Modeling, Dynamics and Control of Continuous Fluidized Bed Layering Granulation Processes

Dissertation

zur Erlangung des akademischen Grades

Doktoringenieur

(Dr.-Ing.)

von Dipl.-Ing. Christoph Neugebauer

geboren am 28. Mai 1986

genehmigt durch

die Fakultät Elektrotechnik und Informationstechnik

der Otto-von-Guericke-Universität Magdeburg.

Gutachter: Prof. Dr.-Ing. Achim Kienle

Prof. Dr.-Ing. Andreas Bück

Prof. Dr.-Ing. Stefan Palis

Promotionskolloquium am 05.06.2020

Foreword

"Nothing in life is to be feared, it is only to be understood."

Prof. Marie Skłodowska Curie

A big Thank You to all who have supported me on this journey.

Kurzzusammenfassung

Die Wirbelschichtsprühgranulation - im Englischen benannt als *Fluidized Bed Layering Granulation* (FBLG) - ist eine bedeutende Klasse partikelbildener Prozesse mit vielfältigen Anwendungen in der modernen Verfahrenstechnik. Ziel des Verfahrens ist das Überführen eines flüssigen Ausgangsstoffes in ein haltbareres und leichter zu handhabendes Granulat. Zu diesem Zweck wird eine Schüttung von Feststoffpartikeln mittels eines erhitzten Gases fluidisiert während der flüssige Rohstoff, zum Beispiel eine Suspension oder Lösung, auf das Partikelbett gesprüht wird. Während der flüssige Anteil des eingedüsten Materials verdunstet, verfestigt sich der feste Bestandteil an der Oberfläche der Partikel. Dies führt zu einem Wachstum der Partikel.

Industriell werden Granulationsprozesse oftmals eingesetzt, um maßgeschneiderte Partikel mit einem hohen Produktdurchsatz herzustellen. Dies kann unter anderem durch einen kontinuierlichen Anlagenbetrieb erreicht werden. Die entsprechende Konfiguration ist durch den permanenten Abzug von Produktpartikeln aus dem Prozess gekennzeichnet. In der Folge müssen neue Partikel durch externe oder interne Keimbildungsprozesse bereitgestellt werden. Auch wenn diese Betriebsweise viele Vorteile bietet, zum Beispiel eine Reduktion der Vor- und Nachbereitung, ist ein stabiler Betrieb der kontinuierlichen FBLG nicht trivial. Aus praktischen Erfahrungen ist bekannt, dass der Prozess zu instabilem Verhalten in der Form selbsterhaltender Schwingungen neigt. Da die Oszillationen zu Variationen der Produkteigenschaften, Schwankungen der Massenströme und, im schlimmsten Fall, zu einem Zusammenbruch des Prozesses führen können, sind sie höchst unerwünscht.

Der erste Schwerpunkt dieser Dissertation ist die Untersuchung der Prozessstabilität kontinuierlicher FBLG Prozesse mittels dynamischer Simulationen sowie numerischer Stabilitätsanalysen. Die dafür benötigten Modellgleichungen werden durch *Population Balance Modeling* bestimmt. Da sich die einzelnen Partikel in ihren Eigenschaften, wie zum Beispiel der Größe, unterscheiden, wird der Zustand der gesamten Partikelpopulation durch Anzahldichteverteilungen beschrieben. Die entsprechende Entwicklung der Population über die Zeit wird durch partielle Differenzialgleichungen, den sogenannten *Population Balance Equations*, beschrieben. Die entwickelten *Population Balance Models* (PBM) sind in der Lage, vorherige experimentelle Ergebnisse qualitativ zu reproduzieren: Während ein Satz von Betriebsparametern einen stabilen Betrieb der kontinuierlichen FBLG vorhersagt - gekennzeichnet durch eine konstante Bettmasse und ein stationäres Profil der Partikelgrößenverteilung über die Prozesszeit - prognostiziert ein zweiter Parametersatz das Auftreten selbsterhaltender Schwingungen. Ein erklärtes Ziel dieser Arbeit ist es, die quantitative Beschreibung des dynamischen Verhaltens der untersuchten FBLG Prozesse zu

verbessern. Dazu werden zusätzliche Effekte, unter anderem das Ausbilden einer aktiven Sprühzone und einer inaktiven Trocknungszone innerhalb der Prozesskammer, berücksichtigt, während die Modellgleichungen andere Teilprozesse, wie zum Beispiel das Mahlen der Partikel, verfeinert werden.

Ein weiterer Schwerpunkt dieser Arbeit ist der Betrieb einer kontinuierlich betriebenen FBLG im Pilotmaßstab in einem stabilen stationären Punkt, dem sogenannten *stable Steady State*. In der untersuchten Konfiguration werden die benötigten Keime durch das Mahlen zu großer Partikel gebildet. Die durchgeführten Experimente bestätigen die Befunde der theoretischen Untersuchungen: Während das feine Mahlen zum Auftreten von Instabilitäten führt, stabilisiert die Grobmahlung den Prozess. Aufgrund der prozess-typischen großen Zeitkonstanten sowie Störeinflüsse ist die FBLG durch ein langes Übergangsverhalten in den stationären Zustand gekennzeichnet. Um die Einschwingzeit zu verkürzen, wurde basierend auf einem angepassten PBM eine Regelstrategie entworfen. Der Einsatz des entwickelten Reglers an der realen Anlage verkürzte das Einschwingen signifikant. So konnte innerhalb kurzer Zeit ein stabiler Betrieb unter stationären Bedingungen erreicht werden.

Um weitere Produkteigenschaften, wie zum Beispiel die Porosität der Partikel, zu berücksichtigen, ist der dritte und letzte Schwerpunkt dieser Arbeit eine Erweiterung des dynamischen Models. Zu diesem Zweck wird das PBM um einen Satz gewöhnlicher Differenzialgleichungen erweitert. Diese repräsentieren die thermischen Bedingungen der FBLG. Entsprechend den Befunden vorheriger experimenteller Studien prädiziert das erweiterte Modell den Einfluss des thermischen Zustands der FBLG auf die Produkteigenschaften, sowie die dynamische Stabilität. Basierend auf dem entwickelten dynamischen Modell werden unterschiedliche Regelstrategien entworfen und durch numerische Simulationen validiert. Es wird gezeigt, dass insbesondere der Einsatz von Mehrgrößenreglern vielversprechend ist, die Produktion maßgeschneiderter Partikel unter stationären Bedingungen zu gewährleisten.

Zusammenfassend zeigt die vorliegende Arbeit, dass *Population Balance Modeling* ein vielseitiges Hilfsmittel im Rahmen kontinuierlich betriebener Wirbelschichtsprühgranulations-Prozesse ist. So können, in Abhängigkeit des Detailgrades, PBM zum Untersuchen des qualitativen oder quantitativen Einflusses unterschiedlichster Betriebsparameter auf die Prozessstabilität und die Produkteigenschaften sowie zum Entwurf und der Validierung modellbasierter Regler verwendet werden.

Abstract

Fluidized bed layering granulation (FBLG) is an essential class of particulate processes widely applied in different fields of modern processing industries. The designated aim of this process is the transfer of a liquid starting material into its more durable and easier to handle granular form. For that purpose, an ensemble of particles is fluidized by a heated gas while the liquid raw material, for instance, a suspension or solution, is sprayed onto the particles. While the liquid fraction of the injected material evaporates, the solid fraction solidifies on the particles' surface, resulting in particle growth.

Many industrial granulation processes aim at the formation of tailor-made particles with high product throughputs. One way to achieve this objective is the continuous operation of FBLG. In this configuration, product particles are permanently withdrawn from the process, while external or internal nucleation processes supply new seed particles. Even though this mode of operation offers many advantages, for example, a reduction of pre- and post processing periods, a stable operation of continuous FBLG is a demanding task. As evidenced by practical observation, the process tends to instabilities in the form of self-sustained oscillations. Since those oscillations may lead to variations of the product properties, fluctuation of the mass flows, and, in the worst case, to a breakdown of the process, they are highly undesired.

The first objective of the present thesis is the investigation of the process stability of continuous FBLG by means of dynamic simulations and numerical stability analyses. The model equations are obtained by population balance modeling: here, a number density distribution characterizes the population of particles which differ in their properties, for instance, in particle size. The corresponding evolution of the population is described by a partial differential equation, the so-called population balance equation. The established population balance models (PBM) are capable of reproducing the experimental results qualitatively: While one set of operating parameters predicts a stable operation of the continuous FBLG - characterized by a constant mass and stationary size distribution of the particle population over process time - a second parameter set forecasts the occurrence of self-sustained oscillations. The aim of this thesis is a more quantitative description of FBLG processes. For this purpose, additional effects, including the separation of the process chamber into an active spraying zone and an inactive drying zone, are taken into account while other sub-processes, for instance, the milling of particles, are refined.

The second objective is the operation of a continuous FBLG under stable steady-state conditions on the pilot-scale. In the studied configuration, the milling of oversized particles

provides the required nuclei. The conducted experiments confirm the theoretical findings: While fine milling leads to an unstable process regime, coarse milling stabilizes the process. Due to large time constants and perturbations, a rather long transition to steady-state characterizes the process. In order to reduce the settling time, a feedback control strategy was designed based on a refined PBM. The application of the controller at the plant decreased the transition time significantly such that an operation under stable conditions was achieved within a short period.

The third and final objective of this thesis is an extension of the PBM to account for further product properties, as, for instance, the particles' porosity. For this purpose, the PBM is extended by a set of ordinary differential equations to consider the thermal conditions in the FBLG. In accordance with previous experimental studies, the derived model predicts the influence of the thermal state of the FBLG on product properties and dynamic stability. Based on the developed dynamic model, different control approaches are designed and validated by numerical simulations. It is shown that in particular the application of multiple input multiple output control strategies is promising to achieve the formation of tailored particles under steady-state conditions.

As a whole, this thesis proves that population balance modeling is a versatile instrument in the context of continuously operated fluidized bed layering granulation. Depending on the level of detail, PBMs can be used for studying the qualitatively or quantitively influence of operating parameters on process stability and product properties as well as for the design and validation of model-based controllers.

Contents

List of Figures

List of Tables

Nomenclature

This thesis covers a variety of topics from different areas of process and control engineering. To ensure a good understanding for engineers of both disciplines, the author retained at the respective standard notations as far as possible. The subsequent section gives an overview of the utilized parameter and time-domain variables. Afterwards, variables of the Laplace-domain are presented. The closing sections introduce utilized subscripts and applied abbreviations.

Parameters & time-domain variables

Symbol	Description	Unit
b	overspray rate	
c_p	specific heat capacity	$\mathrm{J}/_{(\mathrm{kg\ K})}$
d_{32}	Sauter mean diameter of a particle population	mm
e	control error	
h	height	m
k	gain / factor	
m	total mass	kg
$\dot{m}$	mass flow rate	$\mathrm{kg}/_\mathrm{s}$
n	particle size distribution	$1/_\mathrm{mm}$
$\dot{n}$	particle flow rate	$1/_{(\mathrm{mm\ s})}$
q_i	number-based ($i = 0$) and volume based ($i = 3$) *normalized* particle size distribution	$1/_\mathrm{mm}$
p	power of mill	W
t	process time	s
u	velocity of fluidization medium	$\mathrm{m}/_\mathrm{s}$
x	mass fraction	
A	surface or cross section	mm^2
G	particle growth rate	$\mathrm{mm}/_\mathrm{s}$
H	total enthalpy	J
$\dot{H}$	enthalpy flow rate	$\mathrm{J}/_\mathrm{s}$
K	outlet gain / drain gain	
L	characteristic size of a particle	mm

L_i	separation diameter	mm
Q	*cumulative* particle size distribution	
$\dot{Q}$	heat flow	J/s
T	separation function	
V	total volume	mm^3
$\dot{V}$	volume flow rate	mm^3/s
X	moisture content of particles	$g_{p,wet}/kg_{p,dry}$
Y	moisture content of fluidization medium	$g_{f,wet}/kg_{f,dry}$
α	relative size of spraying zone	
α_{fp}	heat mass transfer coefficient	$J/(s\ mm^2\ K)$
β_{fp}	mass transport coefficient	m/s
ϵ	particle or bed porosity	
η	drying potential	
θ	temperature	$^\circ C$
λ	eigenvalue	$1/s$
μ_i	i^{th} moment of size distribution	mm^i
$\dot{\nu}$	normalized drying velocity	
ρ	mass density	kg/m^3
σ	separation sharpness / variance	mm
τ	residence time	s
ψ	drying characteristic	
ω	*relative* velocity	
Δp	pressure drop over the particle bed	mbar
Δh_{evap}	evaporation enthalpy at 0 $^\circ C$	J/kg
Π	operating and simulation parameter set	

Variables in the Laplace-domain

Symbol	Description	Unit
s	Laplace variable	$1/s$
A, B, C, D	matrices of a linear time-invariant (LTI) system	
G	transfer function of an LTI system	
K	transfer function of a feedback controller	
S	sensitivity function	
T	*complementary* sensitivity function	
W	weight functions	
R	reference values in vector notation	
U	inputs of an LTI system in vector notation	
X	states of an LTI system in vector notation	
Y	outputs of aa LTI system in vector notation	

Symbol	Description	
σ	singular values of an LTI system	dB
Δm	multiplicative model error	dB

Subscripts

Symbol	Description
bed	particle bed
break	particle breakage
cone	injection spray-cone
crit	critical moisture content of particles
cs	cut-size
dry	dry fraction of particles or fluidization medium
dust	dust
in	elutriation
enuc	external provided nuclei
eq	moisture content of particles at adsorption equilibrium
evap	evaporation
exp	scenarios: pilot-scale experiments
ext	scenarios: external nucleation
f	fluidization medium
fine	fine fraction of particles
in	inlet
inj	*suspension* injection
int	scenario: internal nucleation
heater	heater of the fluidization medium
K	controller
mill	mill and milling process
nozzle	injection nozzle
nuclei	nuclei / seed particles
out	outlet
over	oversized fraction of particles
p	particle phase
pro	scenario: product properties
product	product fraction of particles
recycle	particle recycle
ref	reference value
s	solid
solvent	liquid solvent
sat	saturation
wet	wet fraction of particles or fluidization medium
Σ	sum / total

Abbreviations

Symbol	Description
CFD-DEM	Computational Fluid Dynamics / Discrete Element Method
FBLG	fluidized bed layering granulation
ODE	ordinary differential equation
MIMO	multiple input multiple output
P	proportional controller
PBM	population balance modeling
PI	proportional integral controller
PSD	particle size distribution
SISO	single input single output

1

Introduction & motivation

Widespread in different fields of modern processing industries, particulate processes are of great relevance [56, 60]. Some of the produced goods are a part of every-day life: sugar, flour, instant coffee & cacao, and washing powder can be found in almost every household; dry powder inhalers increase the quality of life of asthmatic persons significantly. Other particulate products, in turn, are an intermediate product in a complex process chain. For instance, milk powders are essential in food industries, fertilizer granules are commonly used in agriculture and forestry, medical drug tablets consists of granules, and catalyst powders are crucial in chemical industries.

This brief but incomplete overview illustrates the significance of particulate products in many domains as food, pharmaceutical, chemical, and energy industries. The respective particle formulation processes are as diverse as the potential applications. Depending on the raw material, particles can be formulated, inter alia, by spray drying of a liquid, by milling or crushing of a solid or by crystallization processes. A further class of widely applied particle formulation processes is granulation. In general, a granulation process converts fine powders or a liquid, e.g., a solution, suspension, or melt, to granules
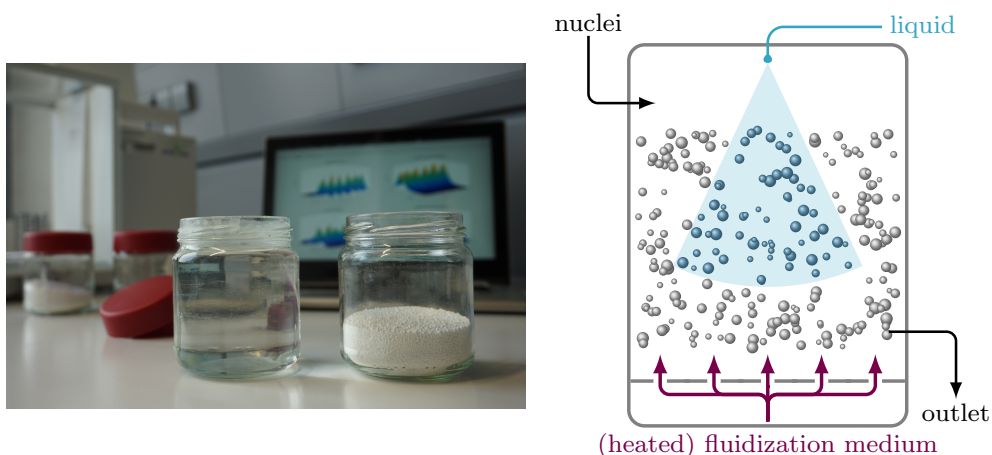
Figure 1.1.: **Left:** 40g of sodium benzoat as 35w% solution and as granules. **Right:** Generalized scheme of fluidized bed layering granulation (FBLG).

process time t
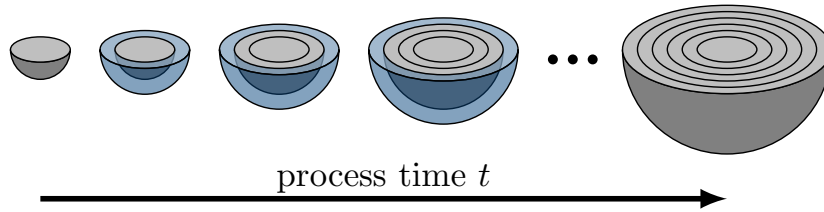
Figure 1.2.: Scheme of layer-wise particle growth: The permanent repetition of wetting and drying within the FBLG results in a layered particle structure.

with predefined properties. Concerning the process and product requirements, different granulation methods are available [56]. For instance,

- tumbling granulation is frequently used to process ores and building materials like cement and dolomite;

- fluidized bed granulation is common to produce fertilizers, inorganic salts, detergents, and pharmaceuticals [7, 65];

- high shear granulation is widely applied in pharmaceutical and detergent industries [90];

- compression agglomeration, e.g., tableting and twin-screw agglomeration, has a manifold of applications in pharmaceutical, food, chemical, and minerals industries [44, 87].

Compared to the starting material, the produced granules offer many benefits. For instance, they might be more durable or are easier to handle.

The focus of the present contribution is on continuous fluidized bed layering granulation (FBLG). Therein, as illustrated in Figure 1.1, a solid-containing liquid, e.g., a solution or suspension, is sprayed onto a bed of particles fluidized by a heated gas. Supported by the heated fluidization medium, the liquid phase of the injection evaporates. Meanwhile, the remaining solid fraction solidifies on the surface, inducing the particles' growth. Resulting from the constant movement of the particles within the granulation chamber, the permanent repetition of wetting and drying leads to a layered particle structure as shown in Figure 1.2 [108].

In comparison with a batch-wise operation, an accurate adjusted continuous FBLG enables a high throughput of product particles with uniform properties. As product particles are withdrawn from the continuous process permanently, nuclei have to be supplied continuously. The required nuclei can be provided as external seed particles or can be gained by internal nucleation processes as thermal overspray [42] or comminuting of oversized particles [19]. However, experimental [93, 94, 95, 97] and theoretical investigations [88, 117] have shown that proper continuous operation of FBLG is not trivial. Depending on the operating parameters, the process settles at a stable steady-state or becomes unstable. Since the unstable process regime, as illustrated in Figure 1.3, is characterized by self-sustained oscillations of the particle size distribution leading
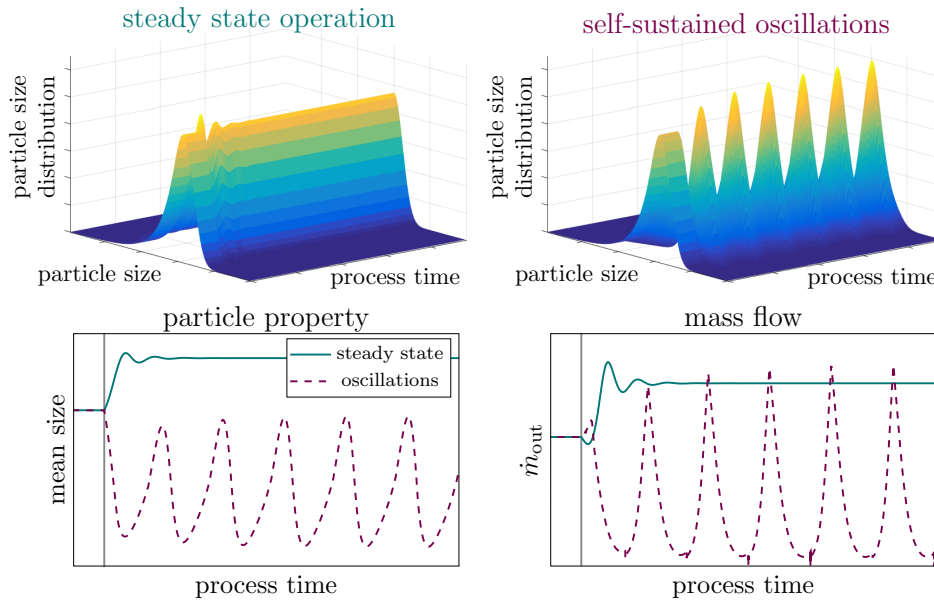
Figure 1.3.: Different forms of the dynamic behavior of continuous layering granulation: While one set of operating parameter leads to the formation of a stable steady-state (**top left**), leading to constant particle properties (**lower left**) and mass flow at the outlet of the granulation chamber over process time (**lower right**), a second parameter set induces the occurrence of self-sustained oscillations (**top right**) resulting in variations of particle properties and mass flows.

to variations of product properties, plant efficiency, and, in the worst case, to a process breakdown, it is highly undesired and has to be avoided.

The key objective of the present thesis is to illustrate how a stable process regime under steady-state conditions can be achieved while product particles with desired properties are formulated. Based on first-principles and experimental observations, dynamic models of FBLG processes are derived. The designed models are a solid base to gain a more in-depth insight into the process. For instance, the influence of the process configuration and selected operating parameters can be investigated by means of dynamic simulations and rigorous system analyses. Besides, the dynamic models can be used for the design and validation of feedback control strategies. Applied at the real plant, the designed controllers are capable of enhancing process performances as well as they guarantee the formation of tailored particles under steady-state conditions. A detailed outline of the thesis is given in the upcoming section.

1.1. Outline

The present thesis consists of six chapters covering different aspects concerning a stable operation of continuous FBLG. Starting with an introduction to the fundamentals of

fluidized bed layering granulation, Chapter 2 presents an overview of experimental and theoretical contributions studying continuous FBLG. Within this chapter, different approaches for modeling the dynamics of FBLG processes are presented. Hereby, the focus is on population balance modeling (PBM). Based on the introduced PBM, the dynamics of continuous FBLG are studied in the subsequent Chapter 3. Thereby, the dynamic model is extended to account for (i) the formation of functional zones and (ii) different process configurations. Based on dynamic simulations and stability analyses, the occurrence of instabilities in continuously operated FBLG is examined.

The following Chapter 4 demonstrates how PBM can be utilized to enhance the performance of pilot-scale plant processes. Based on experimental data, the dynamic model is refined to consider plant characteristics. Model-based controllers are designed and applied to the plant. The derived controllers enhance the process performance significantly. In particular, the transition time to steady-state decreased significantly.

At the beginning of Chapter 5, the dynamic model is extended to account for further key product properties, in particular, the porosity and moisture content of the particles. As those properties depend on the thermal conditions in the FBLG, heat & mass balances are utilized to derive state equations representing temperature and moisture content of particles and fluidization medium. For guaranteeing the formation of particles with desired properties under steady-state conditions, feedback controllers are designed and validated by simulations. The chapter closes with an introduction to multi-stage FBLG.

The final Chapter 6 presents a summary of essential results and provides an outlook on future directions. Main results of this thesis presented in Chapter 3 – 5 have been published in advance. The associated key contributions are presented in chronological order in the following:

- Dreyschultze, C., **Neugebauer, C.**, Palis, S., Bück, A., Tsotsas, E., Heinrich, S., Kienle, A., 2015. *Influence of zone formation on stability of continuous fluidized bed layering granulation with external product classification*, Particuology, 1 – 7.

- **Neugebauer, C.**, Palis, S., Bück, A., Diez, E., Heinrich, S., Tsotsas, E., Kienle, A., 2016. *Influence of mill characteristics on stability of continuous layering granulation with external product classification*, Computer Aided Chemical Engineering 38, 1275 – 1280.

- Bück, A., **Neugebauer, C.**, Meyer, K., Palis, S., Diez, E., Kienle, A., Heinrich, S., Tsotsas, E., 2016. *Influence of operation parameters on process stability in continuous fluidised bed layering with external product classification*, Powder Technology 300, 37 – 45.

- **Neugebauer, C.**, Palis, S., Bück, A., Tsotsas, E., Heinrich, S., Kienle, A., 2017. *A dynamic two-zone model of continuous fluidized bed layering granulation with internal product classification*, Particuology 31, 8 – 14.

- **Neugebauer, C.**, Bück, A., Palis, S., Mielke, L., Tsotsas, E., Kienle, A., 2018. *Influence of thermal conditions on particle properties in fluidized bed layering*

granulation, Processes 6 (12), 235.

- **Neugebauer, C.**, Diez, E., Bück, A., Palis, S., Heinrich, S., Kienle, A., 2019. *On the dynamics and control of continuous fluidized bed layering granulation with screen-mill-cycle*, Powder Technology 354, 765 – 778.

- **Neugebauer, C.**, Bück, A., Kienle, A., 2020. *Control of particle size and porosity in continuous fluidized bed layering granulation processes with sieve mill cycle*, accepted for publication in Chemical Engineering & Technology.

- **Neugebauer, C.**, Seidel, C., Palis, S., Kienle, A., 2020. *Robust Control of Fluidized Bed Layering Granulation*, submitted for presentation at 21$^{\text{th}}$ IFAC World Congress, Berlin.

A complete list of the scientific contributions of the author is given in the *About the author* section at the very end of this thesis.

2

Fluidized bed layering granulation

As motivated in the introducing Chapter 1, the key objective of this thesis is a proper operation of fluidized bed layering granulation under stable steady-state conditions. To enhance the reader's understanding, the FBLG is introduced in two steps: First, fluidized bed processes are introduced; secondly, the different granulation mechanisms are presented. In the subsequent section, an overview of different process configurations and a survey of previous experimental work is given. Followed by a section dedicated to the introduction of the dynamic process models, the closing part of this chapter illustrates how the models can be used to enhance the process understanding and to increase process performance.

2.1. Fluidized bed technologies

The nature of fluidization processes is the conversion of the state of granular materials, e.g., a particle bed, from a static solid-like to a dynamic fluid-like. For that purpose, a fluidization medium is blown upwards through a distribution plate into the process chamber. Compared to the non-fluidized state, the particle mixing and the heat & mass transfer between the solid phase and the surrounding fluid are enhanced in the fluidized state.

The fluidization behavior of the particle bed depends on the velocity of the fluidization medium: effective fluidization requires exceeding the minimum fluidization velocity of the particles, an exceedance of the elutriation velocity results in the blow out the particle bed. Then again, the particles' properties influence the fluidization. As identified by Geldart [38], the (apparent) mass density and the size of the fluidized particles determine the fluidization behavior. Referring to Figure 2.1, Geldart divided the fluidization behavior into four groups:

- The fluidization of **Group A** particles is characterized by a significant expansion of the particle bed. For high fluidization velocities, the undesired formation of hard to control gas bubbles occurs.
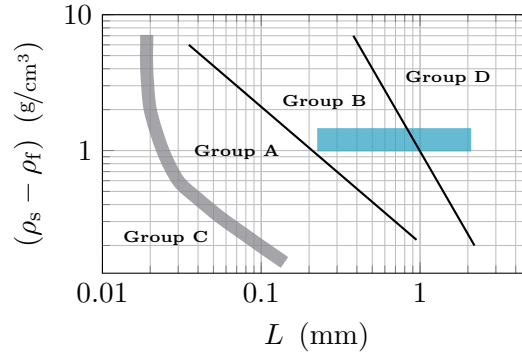
Figure 2.1.: Classification of the fluidization behavior of particles in accordance with Geldart [38]. The domain highlighted in blue relates to the experiments presented in Chapter 4.

- In contrast, a relevant expansion of the particle bed is not observed while fluidizing **Group B** particles. Depending on the fluidization velocity, bubbling occurs.

- Particles of **Group C** are very cohesive and are, therefore, hard to fluidize.

- Due to their large size or high mass density, **Group D** particles are hard to fluidize. Instead of a more-or-less compact particle bed, as observed by fluidization of Group A – C particles, spouting of particles occurs.

In the experiments presented in this thesis, sodium benzoate particles were fluidized with heated air. The related mass densities are given by $\rho_s \approx 1440.0$ kg/m³ and $\rho_f \approx 1.0$ kg/m³, respective. Depending on the actual particle size and porosity, the fluidization behavior corresponds to Group B or Group D. In the contribution [38], the influence of the shape of the fluidized particles was not in the scope of the investigation. However, as shown by Volmari et al. [115], the shape of Group D particles influences their fluidization behavior as well.

The first successful industrial applications of fluidized bed technologies were made in the years 1922 and 1942 in the framework of coal gasification [119] and catalytic cracking of mineral oils [122]. In the 1950s, Dale E. Wurster invented the Wurster Coater [121], which was, at least to the author's knowledge, the first fluidized bed granulation process. In the last decades, the idea of fluidized bed granulation has been pushed forward: new concepts and further areas of applications were developed. The common underlying fundamentals of various granulation processes are introduced in the subsequent section.

2.2. Granulation mechanisms

As in all other classes of granulation processes, different granulation mechanisms co-occur in fluidized bed granulation. In principle, they divide into particle growth, particle breakage & attrition, and nucleation mechanisms. This section briefly introduces the
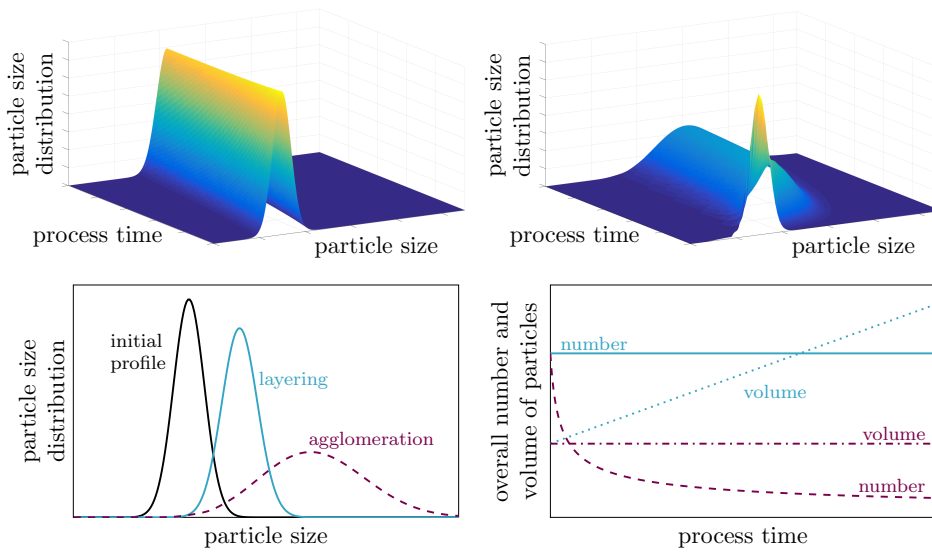
Figure 2.2.: Schematic representation of batch-wise layering granulation (**top left**) and agglomeration (**top right**): While pure layering leads to a narrow particle size distribution, pure agglomeration results in a significant widening of the size distribution (**bottom left**). Thereby, layering granulation is characterized by a constant number of particles and an increase of the overall particle volume over process time, whereas the particle number decreases, but overall particle volume stays constant during agglomeration (**bottom right**).

different categories.

Particle growth   As a key objective of granulation processes is the size enlargement of a particle population, the growth mechanisms are of particular importance. In principle, two different mechanisms are present:

(i) Continuous deposition of mass on the particles' surface, e.g., by injecting a liquid or supplying a powder, leading to differential growth of the particles, is denoted as **layering granulation** [56]. A special case of the layering granulation are coating processes. Here, a layer consisting of different material is applied to encapsulate the particles' core [46].

(ii) The coalescence of particles characterizes the **agglomeration**. Here, two are more particles get into contact and are linked by inter-particle bonding mechanisms, as, for instance, the formation of solid bridges [92, 106]. Thereby, the volume of the resultant particle is the sum of the former individual particles. Hence, discrete particle growth is the characteristic of agglomeration processes [56].

Figure 2.2 presents the growth characteristics corresponding to batch-wise layering and agglomeration. Pure layering granulation leads to slow and compact growth of the particle population. On the contrary, agglomeration results in fast growth but also
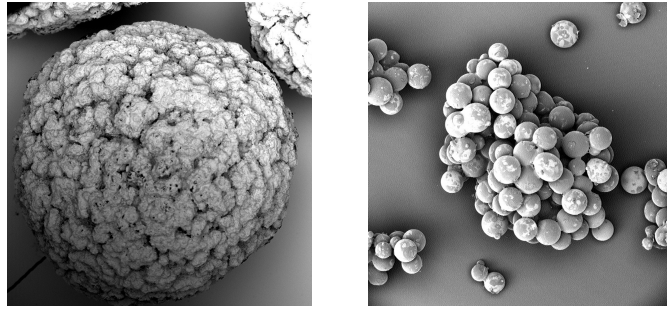
Figure 2.3.: Comparison of particles formulated by fluidized bed layering granulation (**right**) and fluidized bed agglomeration (**left**). The scanning electron microscope images of the particles were originally presented by Hoffmann [48] and Strenzke et al. [106].

in a significant widening of the size distribution. Thereby, the number of particles is constant over process time in the layering process, while agglomeration conserves the overall volume of the particle population. The comparison of the formed particles in Figure 2.3 shows that layering granulation formulates spherical and dense granules while agglomerated particles are non-spherical and more porous. The presented scanning electron microscope images of the particles originate from the contributions of Hoffmann [48] and Strenzke et al. [106].

Particle breakage & attrition   The size reduction of particles within the granulation is caused by particle-particle or particle-device interaction. If particles collide with high impacts, **breakage** might occur. Thereby, dense particles break into fragments while agglomerated particles split into smaller clusters. Otherwise, **attrition**, viz. the abrasion of material from the particles' surface due to contacts at low velocities, leads to the formation of dust.

Nucleation   This class comprises mechanisms resulting in the formation of seed particles within the granulation itself. For instance, an ensemble of dust particles can be rearranged to a larger seed particle by **primary agglomeration**. A second nucleation process is **thermal overspray**. Here, the liquid phase of an injected droplet evaporates before it gets into contact with a particle. The remaining solid serves as a new nuclei.

In general, all the phenomena presented are competing within a granulation process. However, as shown by Ennis et al. [31], a suitable choice of the operating conditions suppresses undesired mechanisms in practice. This insight allows putting the focus on fluidized bed layering granulation while neglecting further granulation mechanisms in the remaining of this thesis.

2.3. Experimental studies concerning continuous FBLG

Besides the already presented granulation mechanisms, a manifold of different sub-processes occurs simultaneously in fluidized bed granulation. To name just a few: particles are fluidized, a liquid can be injected, drying takes place, and particles are transported into, inside, and out of the granulation chamber. In consequence, there is a variety of experimental studies and publications investigating single sub-processes or the overall granulation process. This section provides a brief overview of experimental works concerning FBLG published in recent years. A more detailed presentation of selected key contributions follows in the subsequent chapters.

Starting with the injection of the liquid: Utilizing a two-fluid nozzle, Schulz [96] showed that the size of the spray-cone and the size distribution of injected droplets depend on the configuration of the injection medium and the injection nozzle, e.g., mass concentration and injection pressure. Due to the formation of the spray-cone, the process chamber divides into an active spraying zone and an inactive drying zone. While in the first zone particles' surface is sprinkled with the injected liquid, drying and solidification take place in the second. As shown by Smith & Nienow [101] and Turchiuli et al. [110], a large temperature gradient indicates the transition of the functional zones. Thereby, the configuration of the nozzle influences the formation of functional zones directly.

However, not all of the injected droplets get in contact with a particle. Instead, the liquid phase of some droplets might evaporate before. The remaining solid - denoted as thermal overspray - can be blown out of the granulation chamber or provides new seed particles. As shown by Grünewald et al. [42], this complex process depends on the state of the particle bed and fluidization medium. Droplets that do reach particles settle on their surface. The emerging evaporation was investigated by Sondej et al. [102, 104] by studying the drying process of a sessile droplet of sodium benzoate on the microscopic scale. Besides material properties [32], the initial concentration of the droplet and the drying conditions influences the evaporation. In particular, it was shown that the temperature, moisture content, and mass flow of the fluid determine the drying velocity and, even more important, the structure of the remaining deposit.

On the macroscopic scale, Rieck et al. [91] confirmed these findings by means of a series of lab-scale experiments. In the corresponding batch experiments, the influence of the injection rate and fluid temperature on the shell porosity, i.e., the porosity of the formed layer, was investigated. To compare different operating conditions and predict the shell porosity, Rieck et al. introduced the drying potential. The drying potential, basically defined as the ratio of the actual evaporation rate to the maximum evaporation rate related to the state of the fluidization medium at the inlet, is a measure of the drying efficiency. In this particular case, the drying potential and shell porosity are linearly correlated. The established correlation holds, as shown by Hoffmann et al. [48, 50] and Diez et al. [23], also for continuously operated FBLG processes. Besides, Diez et al. showed that the drying potential determines further key particle properties as surface morphology, solids density, compression strength, and wetting behavior.

However, even if it is well known that continuous FBLGs tends to instabilities in the form of self-sustained oscillations [97], an operation under steady-state conditions - characterized by a constant bed mass and a constant profile of the particle size distribution over process time - was not in the scope of the investigation presented so far. This issue was addressed in a series of experimental studies presented by Schmidt et al. [92, 93, 94, 95]. Depending on the configuration, i.e., internal formation of nuclei by thermal overspray or external formation of nuclei by comminuting oversized particles, the authors studied the influence of the configuration of the particle withdrawal (internal nucleation) and the operating parameters power of the mill (external nucleation), injection rate, temperature of the fluidization medium, and mass flow of the fluidization medium on process dynamics and stability. Thereby, it turned out that a stable steady-state operation is hard to achieve. However, a thorough theoretical analysis was lacking.

So far, the presented contributions focused on single-stage FBLG. By introducing weirs, the process chamber can be divided into different stages. This subdivision allows combining different process steps, e.g., spraying, drying, and cooling, in a single unit and minimizes thus the complexity of utilized equipment. In this configuration, the particle transport from stage to stage is of particular interest. On different scales, the transport behavior of the particles was studied by determining the residence time distribution of particles in the granulation device by using tracer particles (Bachmann et al. [3, 4], Pietsch et al. [86]), by utilizing particle tracking velocimetry (Meier et al. [62]), and by the tracking of particles based on RFID methods (Vollmari & Kruggel-Emden [116]).

Besides experiments, theoretical analyses and simulation studies based on mathematical process models are promising tools to better the understanding of FBLG processes. Depending on the focus of the investigation, different types of dynamic models are available. An overview of selected modeling approaches is presented in the following section.

2.4. Mathematical modelling of FBLG

Depending on the focus of the investigation, the FBLG process can be modeled on different abstractions levels. On the microscopic scale, the dynamics of individual particles are modeled. Here, for instance, interactions of the particle with the fluid, the plant equipment, or other particles are considered. The next coarser abstraction level is the mesoscale. Here, particles are categorized in classes according to their characteristics. It is assumed that particles of a class share the same properties and dynamics. On the macroscopic scale, the coarsest approximation level, the focus is on the integral behavior of the entire particle population. In consequence, selected characteristic values represent the state of the particle bed.

In the literature, different modeling approaches are available on each scale. In this contribution, the microscopic scale is represented by the Computational Fluid Dynamics / Discrete Element Method, the mesoscopic scale by population balance modeling, and

CFD-DEM

population balance modelling
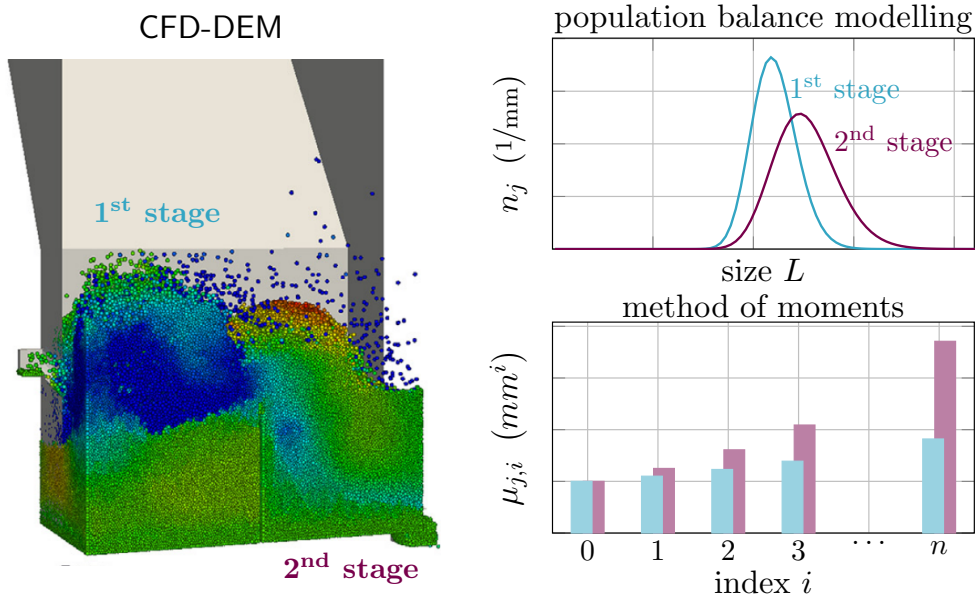
method of moments

Figure 2.4.: Modeling approaches to investigate a two-stage FBLG on different scales: On the microscopic scale, CFD-DEM can be utilized, on the mesoscopic scale PBM, and on the macroscopic the method of moments approach. The illustration corresponding to the CFD-DEM method originates from Diez et al. [22].

the macroscopic scale by the method of moments. Figure 2.4 illustrates the different abstraction levels for a two-stage FBLG.

2.4.1. CFD-DEM methods

The application of Computational Fluid Dynamics / Discrete Element Method models (CFD-DEM) is promising to study the FBLG on the microscopic scale. Based on the concept originally presented by Tsuji et al. [109], CFD-DEM methods determine the dynamics of multiphase systems. By utilizing Newton's laws of motion, the movement of the solid phase (*the particles*) and the motion of the fluid phase (*the fluidization medium*) are coupled. Thereby, CFD-DEM simulations provide an insight into the process that is usually not feasible by other means. For instance, they are capable to examine the influence of different process configurations on the particle wetting [37], zone-formation [8], and particle collision patterns [36]. In recent work, Diez et al. [22] applied CFD-DEM to study the particle-transport inside a multi-stage FBLG for different weir configurations.

However, even if CFD-DEM is a powerful tool for improving process understanding, there is still the drawback of high computing times. Although computer technology and applied algorithms improved significantly in the last decades, the simulation of large-scale systems results quickly in very high computing times up to several days or weeks depending on the utilized hardware.

2.4.2. Population balance modeling

The framework of population balance modeling (PBM) was introduced by Hulburt & Katz [52] and Randolph [89] in the 1960s. It bases on the assumption that an individual (*a single particle*) of a population (*the particle bed*) is characterized by its properties ξ. The properties divide into internal ξ_{int} and external coordinates ξ_{ext}. While internal coordinates define a feature of the individual itself, e.g., size L or volume V, the external coordinates correlate to its location within the operating space as, for instance, the spatial position. The entirety of the population at time t is described by the number density function $n\,(t, \xi_{\text{int}}, \xi_{\text{ext}})$.

Within the scope of fluidized bed layering granulation, the following simplifications are common: (i) assuming a population of spherical particles, the internal coordinate size L - to be precise: the diameter - describes the particles; (ii) the ideal mixing of the particle bed due to the fluidization allows to neglect the external coordinates ξ_{ext}. Hence, $n\,(t, L)$, denoted as particle size distribution throughout this thesis, describes the state of the particle population. A brief introduction to particle size distributions and the accordingly determination in practice is presented in Appendix A.

The temporal evolution of the particle population corresponds to the partial differential equation

$$\frac{\partial n\,(t, L)}{\partial t} = -\frac{\partial\,(Gn)}{\partial L} + B - D \tag{2.1}$$

presented by Hounslow et al. [51]. Here, $\partial(Gn)/\partial L$ represents the progressive particle growth, B the particle birth rate, and D the particle death rate. This equation was refined by Heinrich et al. [47] to account for continuous FBLG. In essential, the one-dimensional PBM is given by

$$\frac{\partial n\,(t, L)}{\partial t} = -G\frac{\partial n}{\partial L} + \dot{n}_{\text{in}} - \dot{n}_{\text{out}} + \dot{n}_{\text{nuclei}} \ . \tag{2.2}$$

where $G\partial n/\partial L$ denotes the layering growth, $\dot{n}_{\text{in}}$ the external particle feed, $\dot{n}_{\text{out}}$ the particle withdrawal, and $\dot{n}_{\text{nuclei}}$ the formation of nuclei within the granulation chamber.

Several authors adopted the presented model equation to consider different effects. For instance, Hampel et al. [45] extended the dynamic model to account for zone-formation while the authors Drechsler et al. [28] and Dosta et al. [25] considered the thermal state of the FBLG by extending the PBM by a set of ordinary differential equations. Furthermore, as presented by Meyer et al. [61], a model extension allows studying the dynamics of multi-stage FBLG. However, if more than one internal coordinate characterize the considered particle population, a multi-dimensional PBM is required to investigate the process dynamics as, for instance, presented by Frank et al. [35] for non-spherical particles.

The partial differential equation (2.2) is the basis of the investigations presented throughout this thesis. Depending on the process configuration and objective of investigation, this equation is refined. In general, the derived equation systems are nonlinear such that

an analytical solution is only feasible in special cases. Hence, numerical methods are required to investigate the process dynamics. For the numerical solution of the defined problems, a method of lines approach was applied. The partial differential equation was discretized utilizing a Finite Volume Method. In specific, a first-order upwind method with 160 (Chapter 3 and Chapter 4) or 200 (Chapter 5) equidistant grid-points was used [55]. The resultant high-dimensional systems of ordinary differential equations (ODEs) were numerically solved using built-in MATLAB (The MathWorks, Natick, USA) functions, e.g., `ode15s` for dynamic simulations.

Compared to the CFD-DEM approach presented in the previous section, the computing effort decreased significantly. In most cases, the PBM was solved within minutes.

2.4.3. Method of moments

A procedure to study the process dynamics of FBLG on the macroscopic-scale is the method of moments. Here, a population is not described by the properties of the single individuals, e.g., the number density distribution n, but by integral quantities of the distribution, so called moments, defined as

$$\mu_i\left(t\right) = \int_0^\infty L^i n\left(t, L\right) \mathrm{d}L \ .$$

(2.3)

Combination with the complex PBM (2.2) yields a low-dimensional system of ODEs representing the *moment* dynamics of the population. Depending on the structure of the involved sub-processes, closure problems may arise which can be resolved with approximate moment algorithms [57].

The moments are closely related to important integral quantities of the particle population, e.g., average or overall particle surface and volume. In comparison to the full PBM less computational effort is required for a numerical solution. On the contrary, the unique back transformation of a set of moments to a full distribution $n\left(t, L\right)$ demands an infinite number of given moments in general. Thus, a reliable statement about the state of the individuals is not always possible.

As the focus of this thesis is on process dynamics of FBLG, the population balance modeling approach is a reasonable compromise between computing effort and process abstraction. The closing section of this chapter presents selected contributions that show how PBM can be used to increase the performance of the process or to enhance the process understanding.

2.5. Applications of PBM

Within the framework of continuous FBLG, many theoretical investigations are based on population balance modeling. First of all, Heinrich et al. [47] derived a PBM for studying the dynamic behavior of continuously operated FBLG processes, neglecting

the formation of functional zones. By means of simulations, the authors showed that, depending on the configuration of the mill, self-sustained oscillations of the particles size distribution and related mass flows might occur for FBLG processes characterized by the formation of nuclei by comminuting oversized particles. Based on the derived PBM, Radichkov et al. [88] elaborated the qualitative influence of additional parameters on the process stability by applying a numerical bifurcation analysis. The authors Vreman et al. [117] extended the PBM presented in [47] to account for continuous FBLG where thermal overspray within the process chamber supplies seed particles. Based on the extended dynamic model, the impact of selected operating parameters on the process stability was investigated. In the summary of the results, the stability analyses [88, 117] revealed the dependency of dynamic stability on the operating parameters: While one parameter set guarantees an operation under steady-state conditions, a second parameter set induces instabilities.

Furthermore, PBM is a suitable tool to gain an enhanced online insight into a process: Combined with state estimation methods, as shown by Bück et al. [17], PBM can be used to restore the size distribution of the particle bed based on a single measurement. A different approach was presented by Palis & Kienle [82]. By estimating the parameters of a predefined PBM, sub-processes can be specified based on plant measurements. Based on experiments on the pilot-scale, the method was recently successfully applied for the identification of the particle milling of oversized particles by Otto et al. [72].

The application of feedback control strategies is promising to enhance dynamic stability and process performance. Thereby, PBM can be utilized for the controller design and validation. For instance, Palis & Kienle [79] showed that a linear PI-controller is capable of stabilizing continuous FBLG processes in the neighborhood of some given reference point. The controller robustness can be increased by H_∞ loop shaping as presented by Palis & Kienle [79, 80]. Further suitable approaches for improving process stability and dynamics are adaptive control strategies [74, 77], model predictive control [14, 16], and non-linear control strategies such as discrepancy based control [76, 78]. However, even if the related closed-loop simulation results are promising, experimental validation is still missing.

To investigate the open-loop dynamics and product properties in multi-stage operation, Bertin et al. [6] established a dynamic model consisting of mass balances, energy balances, and momentum balances as well as a PBM. Based on the introduced dynamic model, Bertin et al. [5] predicted the particle size distribution of the product at steady-state with respect to the operating parameters. For an effective control of multi-stage FBLG, population balance modeling may form the basis for the design of multiple input multiple output strategies as shown by Cotabarren et al. [20] and Palis et al. [83].

3 Process dynamics of continuous FBLG with formation of functional zones

In the following chapter, the influence of selected operating parameter on the dynamic stability of continuous fluidized bed layering granulation is studied. The focus is on the impact of the formation of functional zones on the dynamics. The first part of this chapter motivates the division of the process chamber into a spraying and drying zone. Based on the introduced population balance model, two different process configurations are studied: In the first, nuclei are generated within the granulation chamber by thermal overspray while the formation of seed particles by milling oversized particles characterizes the second. The chapter is based on the author's contributions [15, 29, 70].
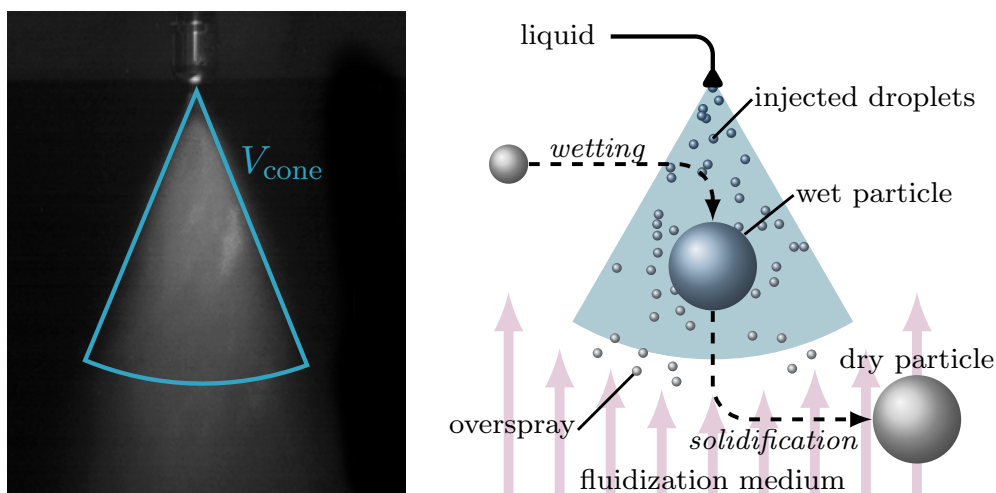
Figure 3.1.: **Left:** Spraying pattern of the injection of sodium benzoate recorded with a high-speed camera. The plain picture was originally presented in [96]. **Right:** Scheme of the particle flow in FBLG with respect to the formation of spraying and drying zone.
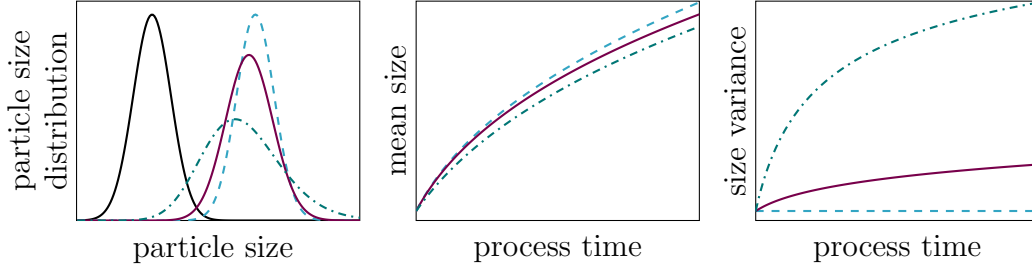
Figure 3.2.: Particle size distribution (**left**), mean size of particle (**center**), and variance of particle size distribution (**right**) for batch-wise FBLG without zone formation (- - -), moderate (——), and pronounced zone formation (-·-·).

3.1. Formation of functional zones in FBLG

While injecting a liquid into the granulation chamber with a two-fluid nozzle, a spray cone of volume V_{cone} is formed. As illustrated in Figure 3.1, only particles inside this cone, denoted as spraying zone, are sprinkled with the liquid. The remaining particles are located in the drying zone. Here, the evaporation of the liquid fraction of the injection takes place while the solid fraction solidifies on the surface inducing the growth of the particles. The boundary between the two functional zones, as shown by Smith & Nienow [101] and Turchiuli et al. [110], is characterized by a large temperature gradient. As a consequence of the zone formation, the bed divides into particles of the spraying zone $n_1(t, L)$ and drying zone $n_2(t, L)$. As presented in Figure 3.2, the formation of functional zones induces a widening of the particle size distribution in batch-wise FBLG over process time (Hoffmann et al. [49], Sherony [99]).

Assuming a homogeneous spatial spreading of particles in the granulation chamber, the relative size of the spraying zone $V_{\text{cone}}/V_{\text{cone}}+V_{\text{drying}}$ and the relative volume of particles within V_1/V_1+V_2 share the same value α. Since the volume of a population of spherical particles is determined by $V_i(t) = (\pi\mu_3(n_i))/6$ with $\mu_j(n_i) = \int_0^\infty L^j n_i(t, L)\, \mathrm{d}L$ the condition

$$\alpha = \mu_3(n_1)/\mu_3(n_1+n_2) \tag{3.1}$$

holds. Meanwhile, the fluidization leads to the exchange of particles between the spraying and drying zone addressed by the particle flow rates

$$\dot{n}_{12}(t, L) = n_1/\tau_1 \quad \text{and} \quad \dot{n}_{21}(t, L) = n_2/\tau_2 . \tag{3.2}$$

The formation of functional zones is described by the relative size of the spraying zone α as well as the mean residence times of particles in the spraying zone τ_1 and the drying zone τ_2. These parameters depend on the configuration of the FBLG. In general, a large α and rapid particle exchange, represented by small residence times τ_1 and τ_2, characterizes a weak zone formation. Vise versa, the pronounced zone formation is characterized by a small α and large values of τ_1 and τ_2. Besides the volume-based definition of the zone formation, different definitions of α have been provided. For instance, Sherony [99] and Wnukowski & Setterwall [120] defined α as the relative

number of particles in the spraying zone. However, as the volume-based definition is related to the apparatus design, it is used throughout this contribution.

Following Maronga & Wnukowski [58], the population balance model (2.2) has to be extended to account for zone formation such that

$$\frac{\partial n_1\left(t, L\right)}{\partial t} = -G\frac{\partial n_1}{\partial L} - \dot{n}_{12} + \dot{n}_{21} + \dot{n}_{1,\text{in}} - \dot{n}_{1,\text{out}} + \dot{n}_{1,\text{nuclei}} \tag{3.3}$$

$$\frac{\partial n_2\left(t, L\right)}{\partial t} = \qquad +\dot{n}_{12} - \dot{n}_{21} + \dot{n}_{2,\text{in}} - \dot{n}_{2,\text{out}} + \dot{n}_{2,\text{nuclei}} \,. \tag{3.4}$$

applies. While $G\partial n_1/\partial L$ describes the particle growth due to layering, $\dot{n}_{i,\text{in}}$ and $\dot{n}_{i,\text{out}}$ stand for the particle feed to and particle withdrawal from the corresponding zone i. The remaining terms $\dot{n}_{i,\text{nuclei}}$ account for the formation of nuclei in the spraying and drying zone. The model equations (3.3) and (3.4) have to be refined to study the continuous FBLG with an internal formation of nuclei by thermal overspray or with the formation of seed particles by grinding oversized particles. The model refinement presented in the remaining of this chapter are based on the population balance models given in Vreman et al. [117] and Radichkov et al. [88] where, however, zone formation was not considered.

3.2. FBLG with internal nucleation

A typical process configuration of continuous FBLG with internal nucleation is presented in Figure 3.3. The nozzle, mounted in top-spray configuration at height h_{nozzle}, sprays small droplets of the injection medium onto the particle bed. While the main fraction of the injection $(1 - b)$ wets the particles' surface and induces the layering growth, the remaining overspray fraction b does not get into contact with the particles. Instead, the liquid fraction of the droplets evaporates such that only the solid fraction remains and forms new seed particles - the so-called overspray - serving as nuclei. To withdraw particles from the process, an outlet tube is installed in the lower part of the granulation chamber. Thereby, the minimum size of withdrawn particles can be set by an adjustable counter-current gas flow through the outlet tube denoted as classification air.

The dynamic behavior of the presented process was studied by means of a linear stability analysis by Vreman et al. [117] and Palis & Kienle [80]. In both contributions, zone formation was not addressed. However, the authors showed that a large amount of injected liquid $\dot{V}_{\text{inj}}$ favors the formation of a stable steady-state. On the contrary, self-sustained oscillations of the particle size distribution $n\left(t, L\right)$ and, in consequence, of the bed height h_{bed} arise for low injection rates $\dot{V}_{\text{inj}}$. Furthermore, Vreman et al. [117] indicated that the size of the internally formed nuclei L_{nuclei} and the minimum size of withdrawn particle L_{out} influences the process stability. These theoretical findings were confirmed by the experimental work of Schmidt et al. [92, 93].
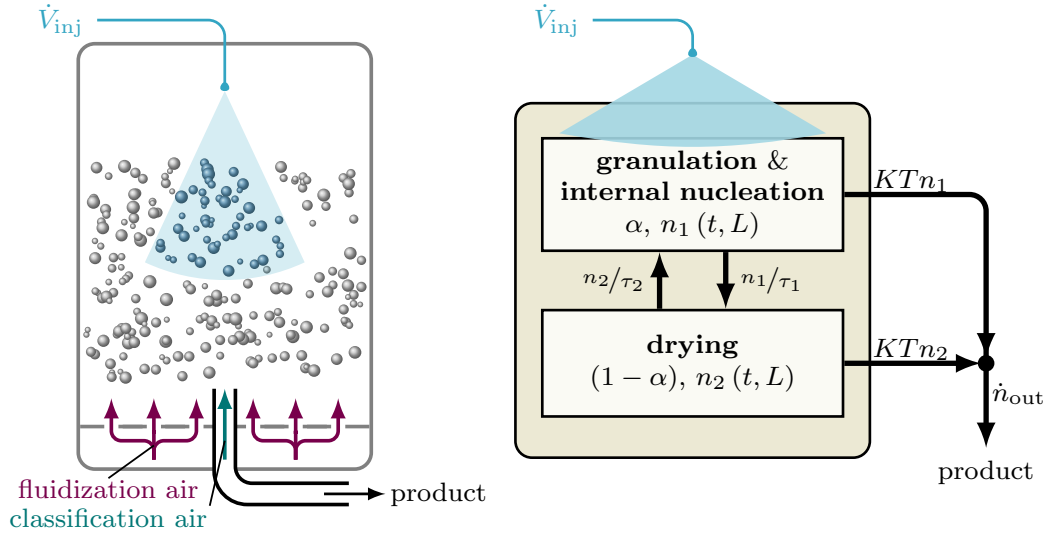
Figure 3.3.: Process scheme (**left**), nomenclature and model structure (**right**) of continuous FBLG with internal nucleation by thermal overspray. In the process scheme, the spraying zone is represented by blue particles while gray particles indicate the drying zone.

3.2.1. Dynamic model

The model structure and nomenclature of the investigated granulation process are presented in Figure 3.3. The fraction $(1-b)$ of the injected liquid $\dot{V}_{\mathrm{inj}}$ covers the surface of particles within the spraying zone $n_1\left(t,L\right)$ and induces the growth. In accordance with Mörl et al. [65] and Vreman et al. [117], the growth rate is determined by

$$G\left(\dot{V}_{\mathrm{inj}}, b, n_1\right) = \frac{2\left(1-b\right)\dot{V}_{\mathrm{inj}}}{\pi\mu_2\left(n_1\right)} \ . \tag{3.5}$$

where the second moment $\mu_2\left(n_1\right) = \int_0^\infty \left(L^2 n_1\left(t,L\right)\right)\mathrm{d}L$ represents the overall surface of the particle bed. The used growth correlation postulates an equal distribution of the injection on the surface of a population of spherical non-porous particles.

The remaining fraction b of $\dot{V}_{\mathrm{inj}}$ is converted to nuclei by thermal overspray. In general, the nucleation process is quite complicated and depends on a variety of operating parameter. For instance, as shown by experiments [42], the states of the particle bed, the fluidization medium, and injection have a significant influence on the nucleation. However, detailed modeling of the overspray process is clearly beyond the scope of this contribution. Instead, as motivated by [117], it is assumed that the overspray fraction b correlates to the height of the particle bed determined by

$$h_{\mathrm{bed}}\left(n_1, n_2\right) = \frac{\pi\int_0^\infty L^3\left(n_1\left(t,L\right) + n_2\left(t,L\right)\right)\mathrm{d}L}{6\left(1-\epsilon_{\mathrm{bed}}\right)A} \ . \tag{3.6}$$

with the cross section of the granulation chamber A and bed porosity ϵ_{bed}. It is assumed that the nucleation rate b attains its minimum value b_∞ if the height of the particle bed

is larger than the nozzle height. If the particle bed is below the nozzle, an increasing distance $(h_{\text{nozzle}} - h_{\text{bed}})$ results in a rise of b. Therefore, the correlation

$$b\left(h_{\text{bed}}\right) = b_{\infty} + \left(1 - b_{\infty}\right) \max\left(0, h_{\text{bed}} - h_{\text{nozzle}}\right) \tag{3.7}$$

is obtained. Assuming a Gaussian size distribution $q_{\text{nuclei}}\left(L\right)$ of the formed seeds, characterized by mean diameter L_{nuclei} and variance σ_{nuclei}, the nucleation is described by

$$\dot{n}_{1,\text{nuclei}} = \frac{6b\dot{V}_{\text{inj}}}{\pi \int_0^{\infty} L^3 q_{\text{nuclei}}\left(L\right) \mathrm{d}L} \quad \text{and} \quad \dot{n}_{2,\text{nuclei}} = 0 \tag{3.8}$$

taking into account that seed formation appears in the spraying zone only.

To describe the particle exchange between the two functional zones, a constant bed porosity ϵ_{bed} and volume of the spraying cone V_{cone} are assumed over process time. These assumptions lead to a constant volume of particles in the spraying zone $V_1\left(n_1\right)$ and - as the overall particle volume $V_1\left(n_1\right) + V_2\left(n_2\right)$ in the granulation chamber is not fixed - to a variable relative size of the spraying zone α. Based on that, the residence time of particles in the spraying zone is determined by balancing the mass flows into and out of the spraying zone. Hence,

$$\frac{1}{\tau_1} = \frac{\dot{V}_{\text{inj}} + V_2/\tau_2 - \pi\mu_3(\dot{n}_{1,\text{out}})/6}{V_1} \tag{3.9}$$

applies. Accordingly, the zone formation is described by the independent parameter V_1, defined by $V_1 = \left(1 - \epsilon_{\text{bed}}\right) V_{\text{cone}}$, and the residence time τ_2. These two parameters depend on the configuration, the geometry, and the operating conditions of the granulation process.

As illustrated in Figure 3.3, product particles are withdrawn from both of the functional zones by the particle outlet. Due to the counter-current air stream through the outlet tube, particles are classified with respect to their size L: While too small particles are blown back into the granulation chamber, particles of sufficient size pass the outlet and are thus removed from the process. The theoretical minimum size of the withdrawn particles, denoted as separation diameter L_{out}, can be determined by balancing drag, induced by classification air, and gravitational forces acting on a particle within the outlet tube. Based on the work of Molerus & Hoffmann [64] the authors Heinrich et al. [47] and Schmidt et al. [93] have shown that L_{out} can be adjusted by manipulating the volume-flow of the classification air stream. To consider non-ideal separation, the Tromp-like separation curve

$$T_{\text{out}}\left(L\right) = \frac{\int_0^L \exp\left((x-L_{\text{out}})/2\sigma_{\text{out}}\right)^2 \mathrm{d}x}{\int_0^{\infty} \exp\left((x-L_{\text{out}})/2\sigma_{\text{out}}\right)^2 \mathrm{d}x} \tag{3.10}$$

with separation sharpness σ_{out} is utilized to describe the classification within the outlet tube (Stieß et al. [105]). Finally,

$$\dot{n}_{1,\text{out}}\left(t, L\right) = K_{\text{out}} T_{\text{out}} n_1 \quad \text{and} \quad \dot{n}_{2,\text{out}}\left(t, L\right) = K_{\text{out}} T_{\text{out}} n_2 \tag{3.11}$$

determine the particle outflows. Here, the gain K_{out} correlates to the probability of an arbitrarily sized particle to enter the outlet tube.

Table 3.1.: Common operating parameters for the FBLG with internal nucleation by thermal overspray and parameter sets $\Pi_{\text{int},i}$ representing different zone formations. Parameter reported in Vreman et al. [117] are indicated by $\star$.

Default operating parameters $\Pi_{\text{int},0}$				Parameter sets for zone formation		
Granulation chamber				**Weak zone formation $\Pi_{\text{int},1}$**		
A	5.00	m^2	$\star$	V_1	2.10	m^3
$\dot{V}_{\text{inj}}$	0.18	dm^3/s		τ_2	10.00	s
h_{nozzle}	440.00	mm	$\star$	**Moderate zone formation $\Pi_{\text{int},2}$**		
ϵ_{bed}	0.50	–	$\star$	V_1	0.25	m^3
Internal nuclei				τ_2	60.00	s
L_{nuclei}	0.30	mm	$\star$	**Pronounced zone formation $\Pi_{\text{int},3}$**		
σ_{nuclei}	0.01	mm		V_1	0.001	m^3
b_∞	0.028	–	$\star$	τ_2	300.00	s
Withdrawal						
L_{out}	0.70	mm	$\star$			
σ_{out}	0.01	mm				
K_{out}	1.92e-4	–	$\star$			
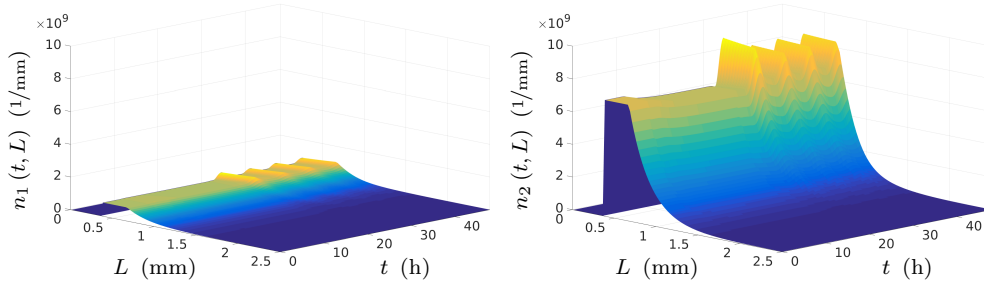
Figure 3.4.: Transient behavior of the particle size distributions $n_1(t,L)$ and $n_2(t,L)$ for continuous FBLG with internal nucleation with parameter set $\Pi_{\text{int},2}$. At $t_1 = 4$ h and $t_2 = 24$ h the injection rate $\dot{V}_{\text{inj}}$ is reduced to 0.17 dm^3/s and to 0.16 dm^3/s, respectively.

3.2.2. Results

In the upcoming section, the influence of key operating parameter on the process dynamics is investigated by means of a simulation study and stability analysis. In accordance with the theoretical finding of Vreman et al. [117] as well as the experimental observations of Schmidt et al. [92, 93], two simulation scenarios are defined: In the first, *Int 1*, the injection rate $\dot{V}_{\text{inj}}$ is varied, in the second, *Int 2*, the separation diameter L_{out} is manipulated. To study the influence of zone formation on the dynamics, the three different operating parameter sets $\Pi_{\text{int},1} - \Pi_{\text{int},3}$ are defined representing a weak, a moderate, and a pronounced zone formation. The parameter sets, together with the operating parameters, and the simulation scenarios are presented in Tables 3.1 and 3.2. The utilized parameter set is based on [117].

Table 3.2.: Simulation scenarios for continuous FBLG with internal nucleation by over-
spray and nucleation by milling of oversized particles.The corresponding
simulation results are presented in the mentioned Figures.

	$t = 0$ h	$t_1 = 4$ h	$t_2 = 24$ h	Figures
Int 1	$\Pi_{\text{int},1}$, $\dot{V}_{\text{inj}} = 0.18$ dm³/s	$\dot{V}_{\text{inj}} = 0.17$ dm³/s	$\dot{V}_{\text{inj}} = 0.16$ dm³/s	3.4 - 3.6, 3.9
Int 2	$\Pi_{\text{int},2}$, $\dot{V}_{\text{inj}} = 0.16$ dm³/s, and $L_{\text{out}} = 0.75$ mm	$L_{\text{out}} = 0.65$ mm	$L_{\text{out}} = 0.55$ mm	3.9
Ext 1	$\Pi_{\text{ext},1}$, $L_{\text{mill}} = 0.85$ mm	$L_{\text{mill}} = 0.775$ mm	$L_{\text{mill}} = 0.70$ mm	3.12 - 3.15

Influence of injection rate $\dot{V}_{\text{inj}}$

As a first step, the dependency of the process dynamics on the injection rate $\dot{V}_{\text{inj}}$ is illustrated by the simulation of scenario *Int 1* for moderate zone formation represented by the parameter set $\Pi_{\text{int},1}$. The initial conditions correspond to the steady-state according to the parameters given in Table 3.1. At $t_1 = 4$ h and $t_2 = 24$ h the injection rate is reduced from 0.18 dm³/s to 0.17 dm³/s and 0.16 dm³/s, respectively.

The process starts, as shown in Figure 3.4, at steady-state indicated by a constant particles size distributions in the spraying zone $n_1(t, L)$ and drying zone $n_2(t, L)$. In consequence, the characteristic variables - here denoted as key process states and presented in Figure 3.5 - are constant as well. The reduction of $\dot{V}_{\text{inj}}$ at t_1 results, according to Equations (3.5) and (3.8), in (i) a reduced growth rate G and (ii) a decrease of the nucleation rate $\dot{n}_{1,\text{nuclei}}$. Due to the reduced amount of formed nuclei, the overall volume of particles within the bed V_Σ and, in consequence, the bed height h_{bed} decrease over process time t. Since the particle volume in the spraying zone V_1 is fixed by the size of the spray cone V_{cone}, only V_2 shirks resulting in an increase of the relative size of the spraying zone α. This can also be observed in the particle size distribution: While $n_1(t, L)$ stays almost constant after the manipulation of $\dot{V}_{\text{inj}}$ at t_1, $n_2(t, L)$ decreases slightly. However, as h_{bed} is still larger than h_{nozzle}, the overspray fraction b remains at its minimum value of b_∞. The constant nucleation favors the formation of a new stable steady-state after a sufficient process time.

In contrast to the first, the second reduction of $\dot{V}_{\text{inj}}$ at $t_2 = 24$ h leads to a significant change in the process dynamics. Instead of settling at new steady-state, self-sustained oscillations of the particle size distributions $n_1(t, L)$ and $n_2(t, L)$ with a period of approximately 7 h arise. Referring to Figures 3.4 and 3.5, these oscillations result directly in oscillating key process states. Based on Figure 3.6, the occurrence of the self-sustained oscillations is clarified by studying the interplay of the nucleation rate b and the bed height h_{bed} introduced by Equation (3.7) within a single oscillation. As an example, the limit-cycle highlighted in Figure 3.6 is studied. The initial-point is the particle size distributions presented in the upper left. Here h_{bed} is at its minimum value. As the particle bed is below the injection nozzle, e.g., $h_{\text{bed}} < h_{\text{nozzle}}$, the overspray fraction b attains the corresponding maximum value.
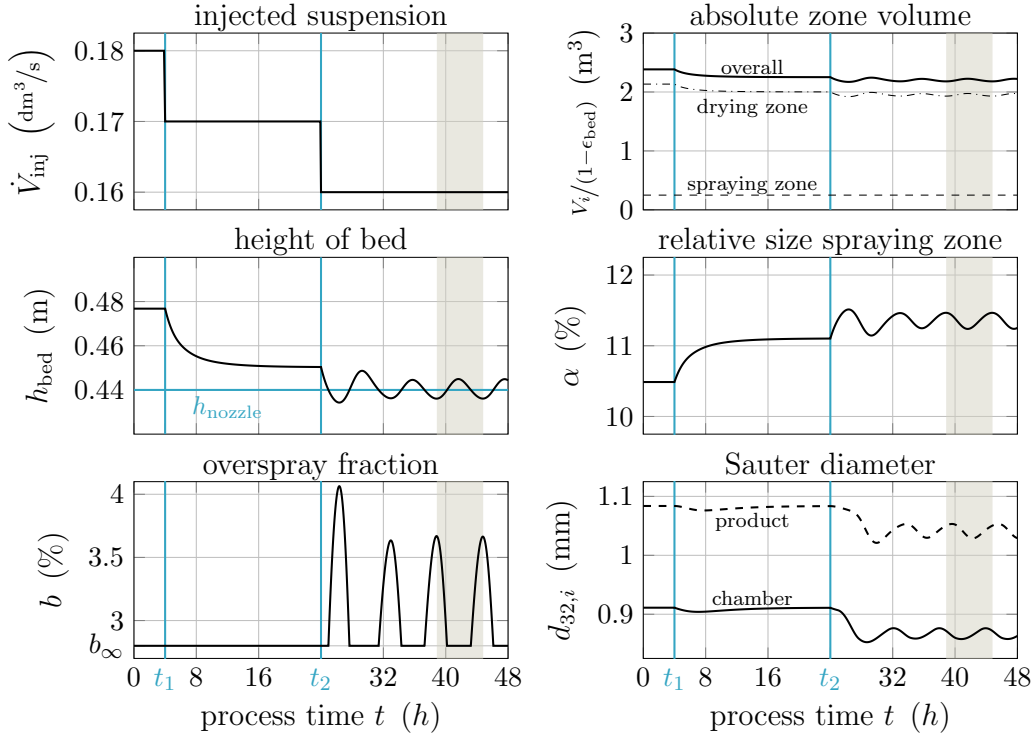
Figure 3.5.: Transient behavior of key process states for continuous FBLG with internal nucleation according to simulation results presented in Figure 3.4. The highlighted domain corresponds to the limit-cycle presented in Figure 3.6.
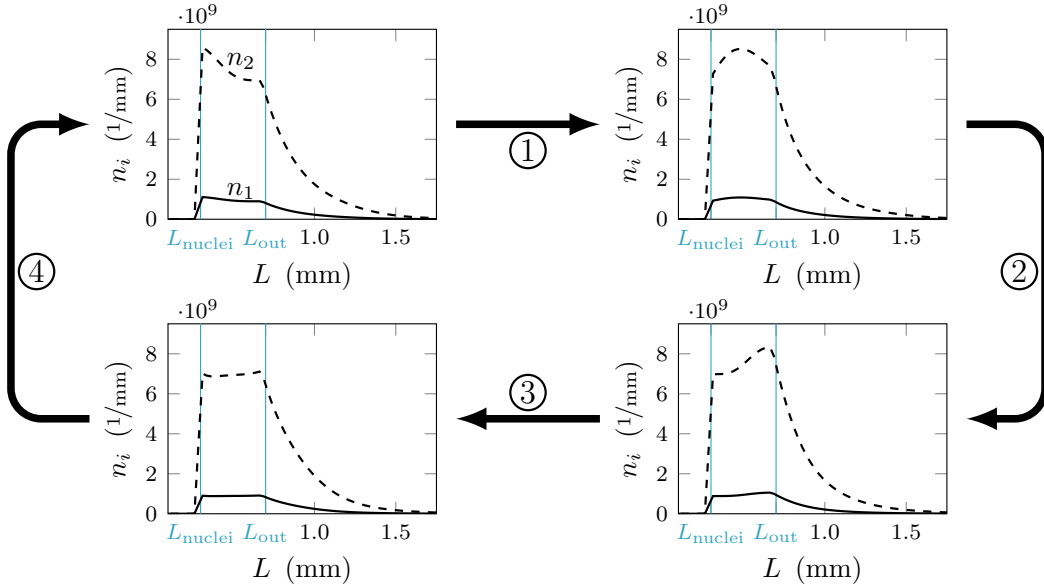
Figure 3.6.: Illustration and motivation of the occurrence of self-sustained oscillations of particle size distributions $n_1(t, L)$ and $n_2(t, L)$ for unstable process regime. The presented limit-cycle corresponds to highlighted domain in Figure 3.5.

① Induced by particle growth, h_{bed} increases leading to a reduced generation of nuclei $\dot{n}_{1,\text{nuclei}}$ as b decreases.

② Particle growth proceeds such that a large particle fraction reaches the separation diameter L_{out}. In the result of the increased overall particle volume V_Σ, h_{bed} passes h_{nozzle} and reaches its maximum value. In consequence of $h_{\text{bed}} > h_{\text{nozzle}}$, b is limited to its minimum b_∞.

③ Since particles larger than L_{out} are withdrawn from the process, h_{bed} decreases. As the bed height drops below the nozzle height, the overspray fraction b increases.

④ If h_{bed} reaches its minimum, b reaches the corresponding maximum value again. In consequence, an increased amount of nuclei $\dot{n}_{1,\text{nuclei}}$ is formed, leading to a peak of the particle distributions $n_1(t, L)$ and $n_2(t, L)$ at the size of the nuclei L_{nuclei}. These peaks initiate the next cycle.

The motivation of the occurrence of self-sustained oscillations is in line with Vreman et al. [117] and Palis & Kienle [80]. In both contributions, the observed instabilities were motivated by the negative feedback between bed height h_{bed} and overspray fraction b.

Influence of zone formation

In the upcoming section, the influence of zone formation on the dynamic stability is explored by means of a one-parameter continuation. As shown in the previous section, the injection rate $\dot{V}_{\text{inj}}$ has a significant influence on process dynamics and was thus selected as a free bifurcation parameter. The results of the parameter continuations corresponding to parameter sets $\Pi_{\text{int},1}$ and $\Pi_{\text{int},3}$ are illustrated in Figure 3.7. Thereby, the two investigated parameter sets represent a weak and a pronounced zone formation.
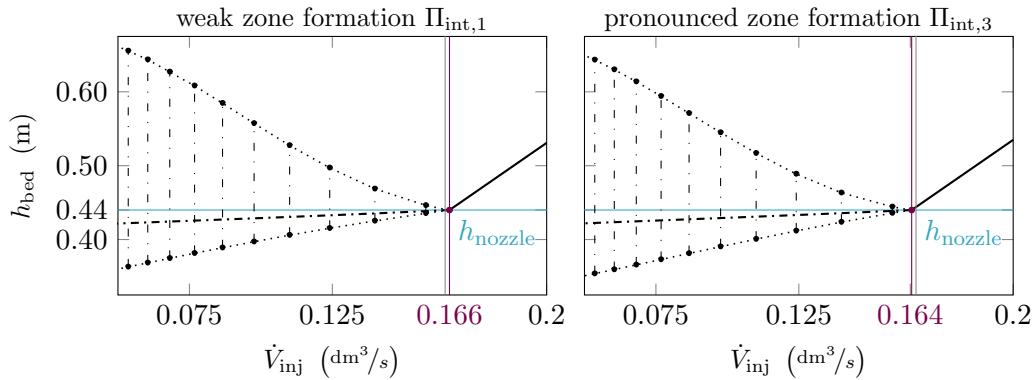
Figure 3.7.: Steady-state and periodic solution branches for the bed height h_{bed} in dependency of the injection rate $\dot{V}_{\text{inj}}$ for weak zone formation (**left**, parameter set $\Pi_{\text{int},1}$) and heavy zone formation (**right**, parameter set $\Pi_{\text{int},3}$). Stable steady-states are indicated by solid lines, unstable steady-states along with amplitudes of corresponding limit-cycles by dash-dotted lines and bullets. The Hopf bifurcation points are indicated by a red line and circle.
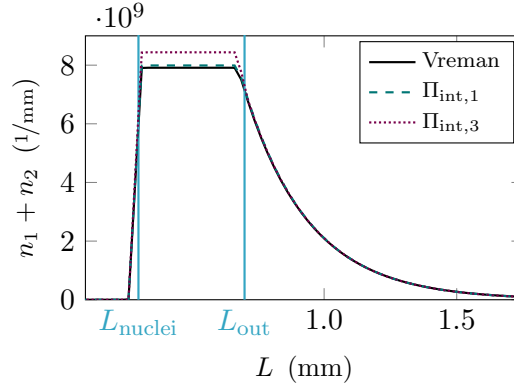
Figure 3.8.: Comparisson of the steady-states of the overall particle size distribution $n(t, L) = n_1(t, L) + n_2(t, L)$ with an injection rate $\dot{V}_{\text{inj}} = 0.18 \text{dm}^3/\text{s}$ for no (Vreman), weak ($\Pi_{\text{int},1}$) and pronounced zone formation ($\Pi_{\text{int},3}$). The steady-state corresponding to FBLG without zone formation complies with Vreman et al. [117].

Figure 3.7 presents the height of the bed h_{bed} at steady state with respect to the injection rate $\dot{V}_{\text{inj}}$. Here, stable steady-states are indicated by solid lines, whereas dashed lines and the associated circles represent unstable steady-states along with the amplitudes of the corresponding self-sustained oscillations. As observed in the simulation of scenario *Int 1*, high injection rates lead to the formation of stable steady-states. Under the investigated conditions, h_{bed} at steady-state is larger than h_{nozzle} such that the nucleation rate b is equal to b_∞. Thus, the nucleation does not depend on the bed height and the negative feedback of b and h_{bed} is not present. The reduction of $\dot{V}_{\text{inj}}$ results in a decrease of h_{bed}. At a specific critical value of $\dot{V}_{\text{inj}}$, the bed height equals the nozzle height. In consequence, the negative feedback of nucleation and bed height is established, resulting in the change of dynamic stability. The resultant instability of the steady-state leads to the occurrence of the self-sustained oscillation. As illustrated in Figure 3.7, the amplitudes of the oscillations increase continuously, starting at zero at the critical point $h_{\text{bed}} = h_{\text{nozzle}}$, with the decrease of the parameter $\dot{V}_{\text{inj}}$.

The observed behavior is a well-known non-linear phenomenon in applied mathematics and engineering science. The switch of the qualitative behavior of a dynamic system with respect to a *bifurcation parameter* at a specific point is known as bifurcation. In the present case, a shift of $\dot{V}_{\text{inj}}$ in the vicinity of the *bifurcation point* induces a smooth onset of a stable limit-cycle emerging from the associated unstable steady-state. This kind of behavior is classified as *supercrtical Hopf bifuraction* [98]. A brief introduction to this phenomena is presented in Appendix B.

Referring to Figure 3.7, the influence of the zone formation on the dynamic stability under the investigated conditions is quite small. Compared to the weak zone formation, the pronounced zone formation shifts the bifurcation point from $\dot{V}_{\text{inj}} = 0.166 \ \text{dm}^3/\text{h}$ to $\dot{V}_{\text{inj}} = 0.164 \ \text{dm}^3/\text{h}$ such that the dynamic stability is slightly improved. This can be explained in the following way: An intensification of the zone formation is char-

acterized by a reduction of the volume of the spray cone V_{cone}. This results in a reduced number and volume of particles within the spraying zone $n_1(t, L)$ leading to faster growth of a smaller number of particles. In consequence, the fraction of particles which can be withdrawn, viz. $L \geq L_{\text{out}}$, shrinks. As the condition $\dot{V}_{\text{inj}} = \dot{V}_{\text{out}}$ with $\dot{V}_{\text{out}} = \pi/6 \int_0^\infty L^3 (\dot{n}_{1,\text{out}} + \dot{n}_{1,\text{out}})\, dL$ has to hold at steady-state, the particle hold-up within drying zone has to increase. This leads, as presented in Figure 3.8, to an increase of the overall particle size distribution $n(t, L) = n_1(t, L) + n_2(t, L)$ and thus to an increased bed height h_{bed}. Hence, an intensification of the zone formation shifts the bifurcation point, characterized by $h_{\text{bed}} = h_{\text{nozzle}}$, to smaller values of $\dot{V}_{\text{inj}}$.

Influence of separation diameter L_{out}

Apart from the injection rate, the dynamic stability of the continuous process depends significantly on the separation diameter L_{out}. To proof the influence of the minimum size of withdrawn particles on the dynamics a two-parameter bifurcation analysis was performed. As parameter set, $\Pi_{\text{int},2}$, representing a moderate zone formation, was chosen. The corresponding result - a stability map - is given in Figure 3.9. Here, the local stability of the steady-state according to the bifurcation parameters $\left(\dot{V}_{\text{inj}}, L_{\text{out}}\right)$ is presented: The non-shaded domains indicate a stable steady-state, whereas the shaded domain represents unstable steady-states inducing the occurrence of self-sustained oscillations. The stability of the steady-states was determined by utilizing the eigenvalues of the Jabobian of the corresponding linearization.

Referring to Figure 3.9, two different boundaries confine the unstable domain:

(i) Upwards, the stability boundary is defined by $h_{\text{bed}} = h_{\text{nozzle}}$. In consequence, stable steady-states are characterized by a bed height above the nozzle height such that b equals b_∞. Thus, the nucleation does not depend on h_{bed}. As shown in the previous section, this is a sufficient condition for dynamic stability.

(ii) Downwards, the unstable domain is limited by a curve of super-critical Hopf bifurcation points. Below this stability boundary, the process is locally stable even though $h_{\text{bed}} < h_{\text{nozzle}}$ holds. To clarify this phenomena simulation scenario *Int 2* was defined. While the injection rate $\dot{V}_{\text{inj}}$ is 0.16 $^{\text{dm}^3}$/s throughout the simulation, the separation diameter L_{out} is decreased from 0.75 mm to 0.65 mm at $t_1 = 4$ h and to 0.55 mm at $t_2 = 24$ h. The key process states h_{bed} and b corresponding to the simulation are presented in Figure 3.9.

The simulation starts at the stable steady-state related to the operating parameter set. After the adjustment of L_{out} at t_1, the process becomes unstable and self-sustained oscillations of the bed height arise. While oscillating, h_{bed} is temporarily above and temporarily below h_{nozzle} resulting in an irregular formation of nuclei as indicated by the temporal course of b. However, the further reduction of L_{out} at t_2 stabilizes the process again. In consequence, the bed height as well as the amplitudes of the associated oscillations decay. As h_{bed} is now permanently below h_{nozzle}, even nucleation is guaranteed such that the process settles at the related steady-state.
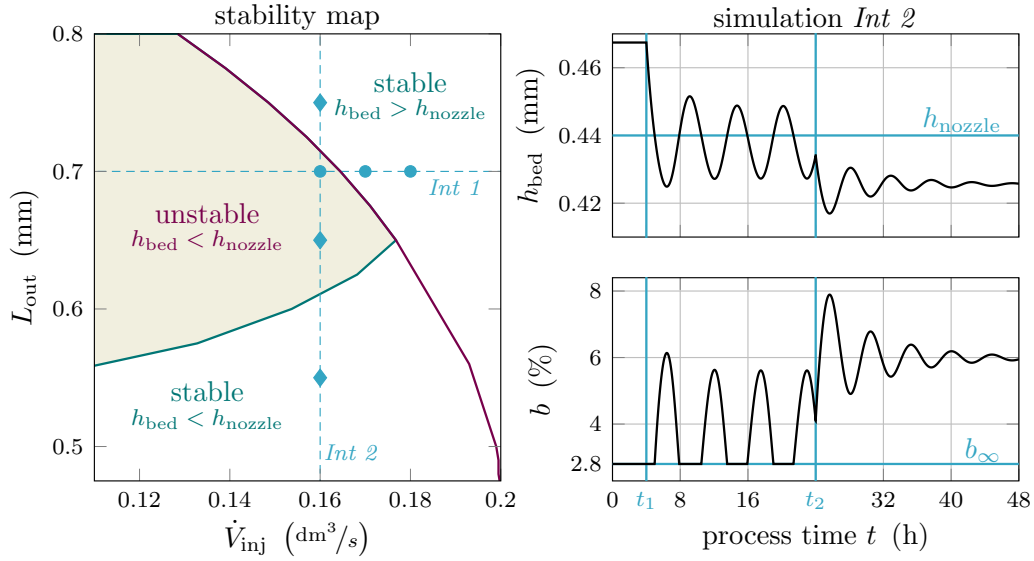
Figure 3.9.: **Left:** Stability domains in the $\left(L_{\text{out}}, \dot{V}_{\text{inj}}\right)$ parameter plane for continuous FBLG with internal nucleation and moderate zone formation represented by parameter set $\Pi_{\text{int},2}$. The shaded region corresponds to unstable steady-states leading to the occurrence of self-sustained oscillations. The markers (—●—) and (—◆—) indicate the operating parameter according to simulation scenarios *Int 1* and *Int 2*, respectively. **Right:** Selected process states of the dynamic simulation corresponding to scenario *Int 2*.

It is worth to mention that the determined stability map is in qualitative agreement with the experimental observations presented in [92, 93]. In a series of three experiments, the authors studied the influence of the classifying particle withdrawal on dynamic stability. Thereby, the separation diameter L_{out} was adjusted by manipulating the velocity of the classification air. In a first experiment, a stable operation was obtained for a small L_{out}. Afterward, the author increased L_{out} such that oscillations of the normalized particle size distribution were observed in a second experiment. In the final experiment, L_{out} was increased once more, leading to stable operation.

Influence of thermal overspray

In the closing section, the influence of the thermal overspray, represented by the minimum overspray fraction b_{∞}, on the process dynamics is investigated. Therefore, stability maps in the $\left(\dot{V}_{\text{inj}}, b_{\infty}\right)$ parameter plane for the three different separation diameters $L_{\text{out}} = \{0.7, 0.65, 0.575\}$ mm are utilized. The remaining parameters comply with $\Pi_{\text{int},2}$. Again, two-parameter continuations were used to determine the stability maps. The corresponding results are presented in Figure 3.10.

Referring to Figure 3.9, (i) the left stability map, $L_{\text{out}} = 0.7$ mm, coincides with the upper stability boundary defined by $h_{\text{bed}} = h_{\text{nozzle}}$, (ii) the central map, $L_{\text{out}} = 0.65$ mm, represents the transition from upper to lower boundary, and (iii) the right
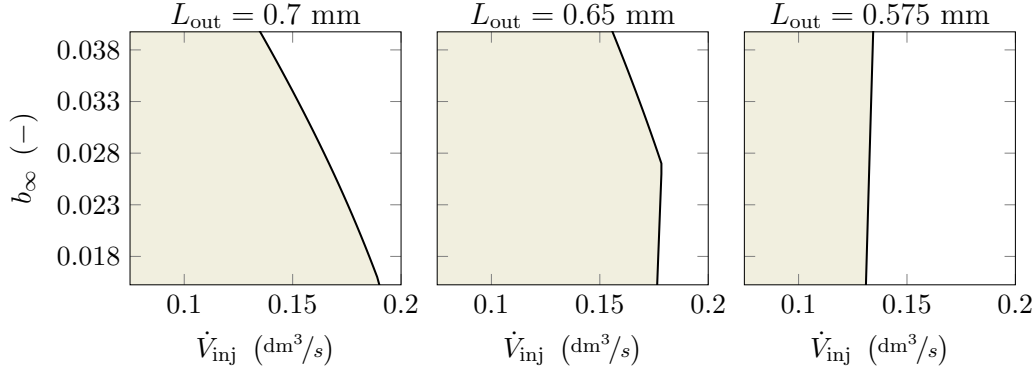
Figure 3.10.: Influence of minimum overspray fraction b_∞ on the dynamic stability in the $\left(\dot{V}_{inj}, b_\infty\right)$ parameter plane for parameter set $\Pi_{int,2}$. The shaded domains represent unstable steady-states.

map, $L_{out} = 0.65$ mm, correlates to the lower stability-boundary where $h_{bed} < h_{nozzle}$ applies.

Due to the positive correlation of the number of formed nuclei and b_∞, defined by (3.7) and (3.8), an increase of b_∞ shifts the critical $\dot{V}_{inj}$ to smaller values along the upper stability boundary. As a consequence, an increase of b_∞ leads to a raised overall particle volume within the bed and, thereby, to a larger bed height. Thus, the boundary $h_{bed} = h_{nozzle}$ is shifted to lower injection rates. On the contrary, the lower stability boundary does not depend significantly on b_∞. This is motivated by $b > b_\infty$ as the condition $h_{bed} < h_{nozzle}$ holds at this boundary.

3.3. FBLG with screen-mill-cycle

Besides internal seed formation, e.g., by thermal overspray, external processes can be used to form nuclei. For instance, the granulation process can be extended by a screen-mill-cycle. As depicted in Figure 3.11, withdrawn particles are classified by screening into the undersized fine, the product, and the oversized coarse fraction. While the product particles are removed from the granulation process, oversized particles are comminuted by milling. Afterward, the milled particles are, together with the fine fraction, recycled to the granulation chamber serving as nuclei. In addition, further external nuclei can be supplied.

Due to the particle recycle, the continuous process tends to instabilities in the form of nonlinear self-sustained oscillations. As reported by Schütte et al. [97], those oscillations lead to variations of the characteristic particle size over process time in practice. To gain a more in-depth insight, the process dynamics were investigated by means of a simulation study by Heinrich et al. [47] and stability analysis by Radichkov et al. [88]. Both contributions proved the significant influence of the milling on the qualitative process behavior: While coarse milling led to the formation of a stable steady-state, fine milling favored self-sustained oscillations. These theoretical results were confirmed by the experiments of Schmidt et al. presented in [92, 95].

Compared to the previous theoretical examinations [47, 88], the influence of zone-formation on process stability is considered and studied in the remainder of this section.
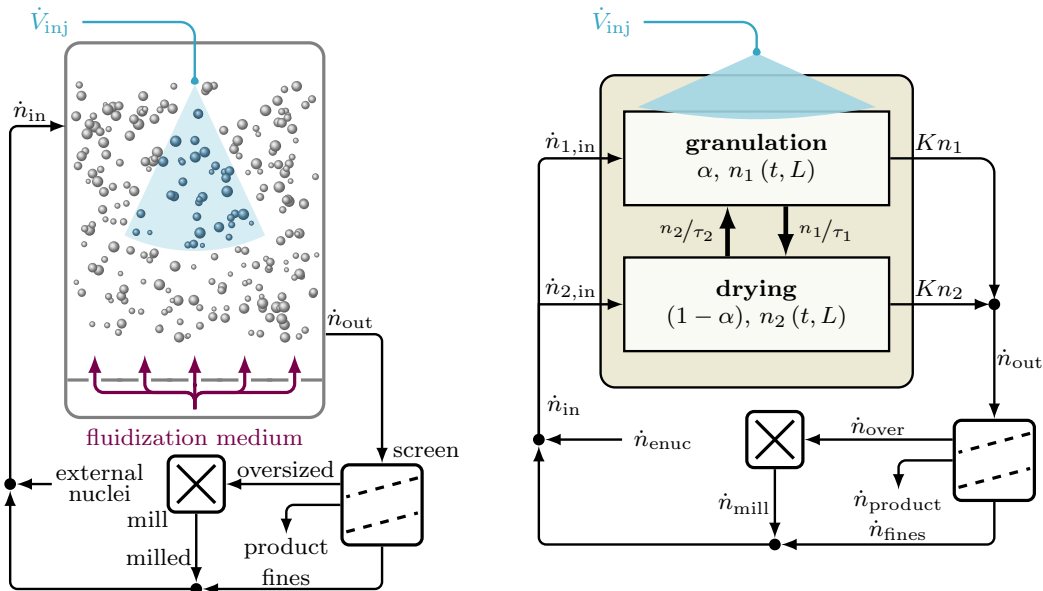
Figure 3.11.: Process scheme (**left**), nomenclature and model structure (**right**) of continuous FBLG with external formation of nuclei by milling of oversized particles. In the process scheme, the spraying zone is represented by blue particles while gray particles indicate the drying zone.

3.3.1. Dynamic model

The flowsheet corresponding to the continuous FBLG with screen-mill-cycle is illustrated in Figure 3.11. The initial point of the modeling is the population balance equations (3.3) and (3.4). In contrast to the previous investigated granulation process, it is assumed that the formation of internal nuclei is suppressed such that $\dot{n}_{1,\mathrm{nuclei}} = \dot{n}_{2,\mathrm{nuclei}} = 0$. In consequence, all droplets of the injected liquid $\dot{V}_{\mathrm{inj}} = x_{\mathrm{inj}}\dot{m}_{\mathrm{inj}}/\rho_{\mathrm{s}}$ are sprinkled on the particles within the spraying zone inducing the layering growth. The terms $\dot{m}_{\mathrm{inj}}$, x_{inj}, and ρ_{s} denote the mass flow of the injected liquid, the corresponding mass fraction of the solid within the liquid, and the associated mass density. Again, an equal distribution of the injection on the particles n_1 is supposed. Thus, assuming non-porous, spherical particles, the growth rate is determined by

$$G\left(\dot{V}_{\mathrm{inj}}, n_1\right) = \frac{2\dot{V}_{\mathrm{inj}}}{\pi\mu_2\left(n_1\right)} \quad \text{with} \quad \mu_i\left(n\right) = \int_0^\infty L^i n\left(t, L\right) \mathrm{d}L \ . \tag{3.12}$$

During the process, particles are representatively withdrawn from both of the functional zones such that

$$\dot{n}_{1,\mathrm{out}}\left(t, L\right) = K_{\mathrm{out}}n_1 \quad \text{and} \quad \dot{n}_{2,\mathrm{out}}\left(t, L\right) = K_{\mathrm{out}}n_2 \tag{3.13}$$

hold. By adjusting the particle outlet via the drain gain K_{out}, the bed mass is kept constant. As a constant bed mass implies a constant third order moment of the particle bed $\mu_3\left(n_1 + n_2\right)$, the condition

$$\frac{\mathrm{d}\mu_3\left(n_1 + n_2\right)}{\mathrm{d}t} = \int_0^\infty L^3\left(\frac{\partial n_1}{\partial t} + \frac{\partial n_2}{\partial t}\right)\mathrm{d}L = 0 \tag{3.14}$$

has to be fulfilled. Based on this condition and the population balance equations (3.3) and (3.4), the bed mass conserving drain is determined by

$$K_{\mathrm{out}} = \frac{\int_0^\infty L^3\left(-G\partial n_1/\partial L + \dot{n}_{1,\mathrm{in}} + \dot{n}_{2,\mathrm{in}}\right)\mathrm{d}L}{\int_0^\infty L^3\left(n_1 + n_2\right)\mathrm{d}L} \tag{3.15}$$

The withdrawn particles $\dot{n}_{\mathrm{out}} = \dot{n}_{1,\mathrm{out}} + \dot{n}_{2,\mathrm{out}}$ are transported to the screen and classified into fines $\dot{n}_{\mathrm{fines}}$, product $\dot{n}_{\mathrm{product}}$ and oversized fraction $\dot{n}_{\mathrm{over}}$. As the dynamics of the process periphery, i.e., screen and mill, are significantly faster than the dynamics of the layering growth, they are neglected. Thus, screening and milling are described by algebraic equations.

The screening of $\dot{n}_{\mathrm{out}}$ is described by the cumulative normal distribution function serving as separation functions T_{I} and T_{II}. Thus, the classification is determined by

$$T_i\left(L, L_i, \sigma_i\right) = \frac{\int_0^L \exp\left(\left(x - L_i\right)/2\sigma_i\right)^2 \mathrm{d}x}{\int_0^\infty \exp\left(\left(x - L_i\right)/2\sigma_i\right)^2 \mathrm{d}x} \quad \text{with} \quad i = \{\mathrm{I}, \mathrm{II}\} \tag{3.16}$$

with the separation diameter L_i and the separation sharpness σ_i. The separation functions T_i represent the probability of a particle of size L to remain on the corresponding

screen i. Consequently, $(1 - T_i)$ is the probability of a particle to pass this screen. As a whole, the screening is described by

$$\dot{n}_{\text{over}} = T_{\text{I}} \, \dot{n}_{\text{out}}, \tag{3.17}$$

$$\dot{n}_{\text{product}} = (1 - T_{\text{I}}) \, T_{\text{II}} \, \dot{n}_{\text{out}}, \quad \text{and} \tag{3.18}$$

$$\dot{n}_{\text{fines}} = (1 - T_{\text{I}}) \, (1 - T_{\text{II}}) \, \dot{n}_{\text{out}}. \tag{3.19}$$

As a next step, oversized particles are milled. In general, milling is a quite complex process depending, for instance, on the type and configuration of the mill as well as the properties of the ground material. However, as the focus of the current section is on the quantitative process behavior, a simple milling model was utilized. Therefore, it is assumed that the mill imprints the Gaussian size distribution

$$q_{\text{mill}} \left(L, L_{\text{mill}}, \sigma_{\text{mill}} \right) = \frac{\exp \left(-(L - L_{\text{mill}})^2 / 2\sigma_{\text{mill}}^2 \right)}{\sigma_{\text{mill}} \sqrt{2\pi}} \tag{3.20}$$

with the mean size of milled particles L_{mill} and the variance σ_{mill} on the oversized particle fraction $\dot{n}_{\text{over}}$. Assuming a mass conserving milling, the particle flow out of the mill is given by

$$\dot{n}_{\text{mill}} = \frac{q_{\text{mill}} \, \mu_3 \left(\dot{n}_{\text{over}} \right)}{\mu_3 \left(q_{\text{mill}} \right)}. \tag{3.21}$$

The milled particles are merged with the fine fraction and, optionally, with the external nuclei such that $\dot{n}_{\text{in}} = \dot{n}_{\text{mill}} + \dot{n}_{\text{fines}} + \dot{n}_{\text{enuc}}$ applies. Therefore, the particle flow rate of the external nuclei is determined by

$$\dot{n}_{\text{enuc}} = \frac{6 q_{\text{enuc}}}{\pi \rho_{\text{s}} \mu_3 \left(q_{\text{enuc}} \right)} \dot{m}_{\text{enuc}} \tag{3.22}$$

depending on the predefined mass flow $\dot{m}_{\text{enuc}}$ and the normalized size distribution q_{enuc}. Here, q_{enuc} is assumed to be normally distributed with mean diameter L_{enuc} and variance σ_{enuc}. While fed to the granulation chamber, the particle flow $\dot{n}_{\text{in}}$ divides, with respect to the relative size of the corresponding functional zone, into

$$\dot{n}_{1,\text{in}} = \alpha \dot{n}_{\text{in}} \quad \text{and} \quad \dot{n}_{2,\text{in}} = (1 - \alpha) \, \dot{n}_{\text{in}}. \tag{3.23}$$

In addition to the already introduced particle flows into and out of the granulation chamber, $\dot{n}_{i,\text{in}}$ and $\dot{n}_{i,\text{out}}$, particles are exchanged between the two functional zones. The particle flow from the spraying to the drying zone

$$\dot{n}_{12} = {n_1}/{\tau_1} \quad \text{and vice versa} \quad \dot{n}_{21} = {n_2}/{\tau_2} \tag{3.24}$$

depend on τ_1 and τ_2. Based on the assumptions of (i) a constant bed volume in accordance with Equation (3.15), (ii) a constant size of the spray cone throughout the process, and (iii) a homogeneous spreading of particles within the granulation chamber, the correlation of the characteristic residence times

$$\frac{1}{\tau_1} = \frac{1}{\tau_2} \frac{1 - \alpha}{\alpha} \tag{3.25}$$

Table 3.4.: Default operating parameter set $\Pi_{\mathrm{ext},1}$ for the FBLG with screen-mill-cycle.

Operating parameter set $\Pi_{\mathrm{ext},1}$ (⋆ *as reported in Radichkov et al. [88]*)							
Granulation chamber				Screens			
m_{bed}	100	kg	⋆	L_{I}	1.00	mm	⋆
$\dot{m}_{\mathrm{inj}}$	100	kg/h	⋆	σ_{I}	0.065	mm	⋆
x_{inj}	1			L_{II}	1.40	mm	⋆
ρ_{s}	1600	kg/m³	⋆	σ_{II}	0.055	mm	⋆
Zone formation				Mill			
α	20.00	%		L_{mill}	0.85	mm	
τ_2	10.00	s		σ_{mill}	0.10	mm	⋆
External nuclei							
L_{enuc}	1.0	mm	⋆				
σ_{enuc}	0.15	mm	⋆				
$\dot{m}_{\mathrm{enuc}}$	0.0	g/s					

is determined. The same correlation was, for instance, used by Hampel et al. [45] for a continuous coating process postulating that the particle exchange between the functional zones does not change the corresponding volumes. In consequence of (3.25), the zone formation is described by the two parameters α and τ_2. As will be shown in the remainder of this section, the two parameters are capable of representing a manifold of configurations and geometries of the granulation chamber.

3.3.2. Results

Based on the introduced dynamic model, the influence of key operating parameter on the dynamics of the continuous FBLG with screen-mill-cycle is investigated in the upcoming section. As a first step, the occurrence of self-sustained oscillations is illustrated and motivated by utilizing a dynamic simulation. In accordance with the contributions [47, 88, 92, 95, 97], L_{mill} was manipulated to observe different forms of qualitative behavior. Afterward, the influence of zone formation on dynamic stability is studied by means of rigorous stability analysis. The impact of the process configuration and further operating parameter on the dynamics is investigated in the closing sections. For all calculations, parameter set $\Pi_{\mathrm{ext},1}$ is used as a base. Deviations are explicitly stated. The default parameter set $\Pi_{\mathrm{ext},1}$, presented in Table 3.4, is based on the contribution of Radichkov et al. [88].

Influence of milling

In this section, the influence of the milling on the qualitative behavior of the FBLG with screen-mill-cycle is studied by means of a simulation. The corresponding results are presented in Figures 3.12 and 3.13. As initial state, the steady-state according to parameter set $\Pi_{\mathrm{ext},1}$ with $L_{\mathrm{mill}} = 0.85$ mm is used. At $t_1 = 4$ h and $t_2 = 24$ h the mean
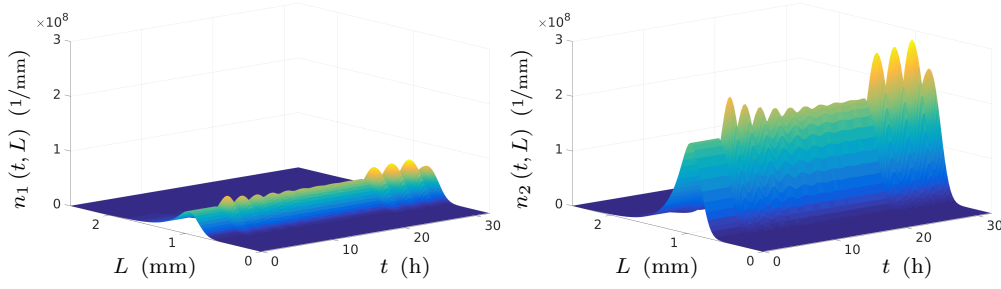
Figure 3.12.: Transient behavior of the particle size distributions $n_1(t, L)$ and $n_2(t, L)$ for continuous FBLG with screen-mill-cycle with parameter set $\Pi_{\text{ext},1}$. At $t_1 = 4$ h and $t_2 = 24$ h the injection rate L_{mill} is reduced to 0.775 mm and to 0.7 mm, respectively.

diameter of milled particles is reduced to 0.775 mm and 0.70 mm. Whereas $L_{\text{mill}} = 0.85$ mm represents coarse milling, fine milling is represented by $L_{\text{mill}} = 0.70$ mm.

Referring to the simulation results, the process starts at a steady-state indicated by a constant profile of the particle size distributions n_1 and n_2. The reduction of L_{mill} at t_1 induces a reduction of the size of nuclei and, thereby, a change of the particle size distributions in the spraying and drying zone. The triggered oscillations of n_1 and n_2 decay over process time such that a new particle size profile is established. As illustrated in Fiugre 3.13, the reduced L_{mill} results in a reduction of the characteristic particle size. Here, the Sauter mean diameter, defined by $d_{32} = {\mu_3(n_1+n_2)}/{\mu_2(n_1+n_2)}$, is used as a representative of the size distribution of the particle population. As the third order moment $\mu_3(n_1 + n_2)$ is constant throughout the simulation, indicated by the constant overall particle volume $V_\Sigma = (\pi/6) \, \mu_3(n_1 + n_2)$, a reduced d_{32} implies an increase of $\mu_2(n_1 + n_2)$. In accordance with Equation (3.12), the growth rate G is inversely proportional to the second-order moment. Thus, the particle growth is slowed down. In addition, the decrease of L_{mill} leads to an increase in the mass fraction of the fines and a decrease of the oversized fraction. In consequence, the throughput of the mill is reduced. In summary, the granulation process is deflected from the initial steady-state due to the set-point switch of L_{mill} from 0.85 mm to 0.775 mm at t_1. However, after a sufficient process time, the continuous FBLG settles at a new steady-state. Therefore, the corresponding steady-state is classified as stable.

The further reduction of L_{mill} to 0.70 mm at t_2 results in a loss of stability. Now, self-sustained oscillations of n_1 and n_2 and, in result, of the key process states arise. Based on Figure 3.14, the formation of self-sustained oscillations is motivated by analyzing the interplay of the overgrowing of particles and the formation of nuclei by milling within an oscillation. The analysis starts with the particle size distribution shown in the upper left. Here, the related Sauter mean diameter d_{32} is at its minimum value:
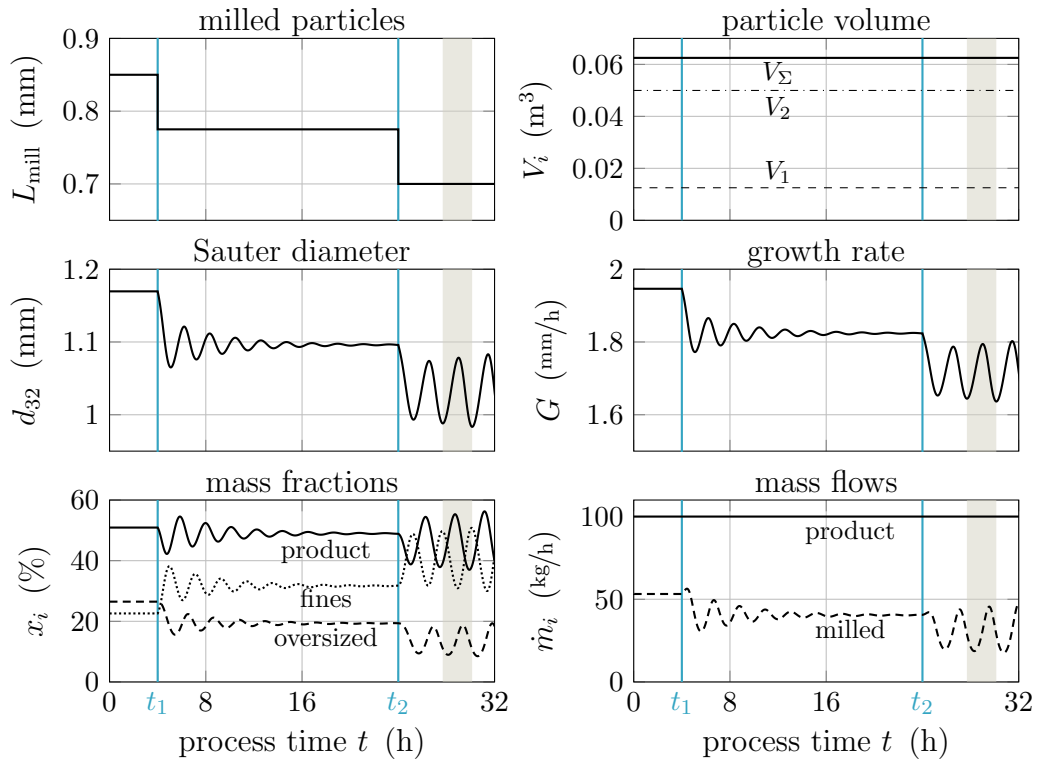
Figure 3.13.: Transient behavior of key process states for continuous FBLG with screen-mill-cycle according to simulation results presented in Figure 3.12. The highlighted domain correlates to the limit-cycle presented in Figure 3.14.
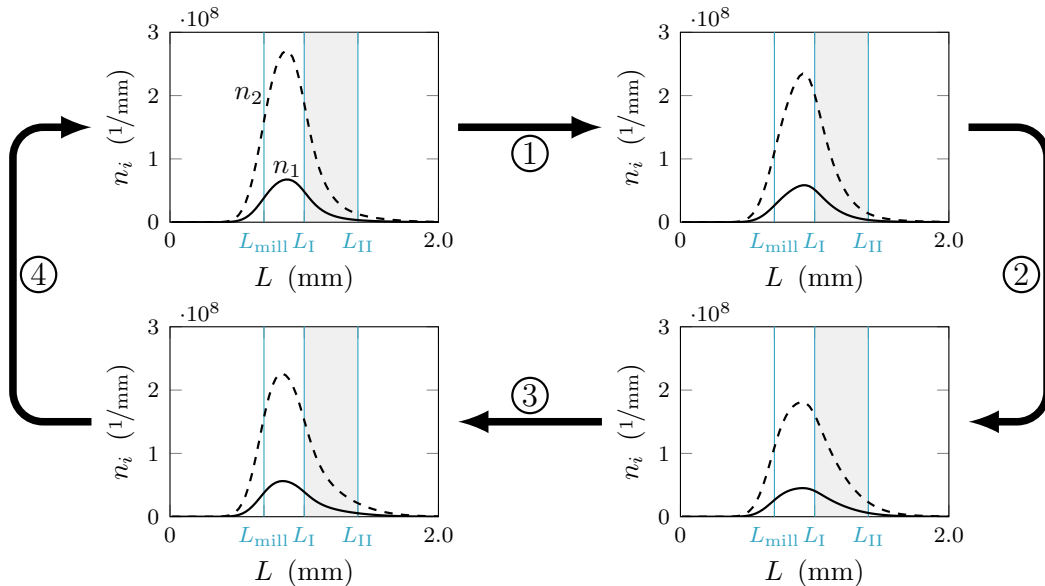
Figure 3.14.: Illustration and motivation of the occurrence of self-sustained oscillations of particle size distributions $n_1(t, L)$ and $n_2(t, L)$ for unstable process regime of FBLG with screen-mill-cycle. The product range is highlighted in gray. The presented limit-cycle correlates to the highlighted domain in Figure 3.13.

①   The small d_{32} is caused by a large mass fraction of the fines. It implies, due to the constant particle volume, a large overall surface of the particles within the bed. In consequence, the growth rate G is quite small, resulting in an uniform particle growth leading to a narrow size distribution. However, as the mass fraction of the oversized particles is at its minimum value, the formation of nuclei is at is minimum as well.

②   In consequence of the particle growth, the peak of the size distributions n_1 and n_2 shifts to larger values. Thus, the Sauter mean diameter d_{32} rises. The growth leads to a decrease in the fine and an increase in the product fraction.

③   As a result of the narrow particle size distribution, a large number of particles enter the product fraction, defined by the separation diameters of the screens L_{I} and L_{II}, simultaneously. As not all product particles can be withdrawn from the process - the condition of a constant bed mass has to be fulfilled - a large number of particles overgrow the upper limit L_{II} and enter the oversize fraction. The illustrated particle size distributions correspond to the maximum value of the Sauter mean diameter in the investigated period.

④   The increased mass fraction of the oversized particles leads to an enhanced generation of nuclei. Thus, the peaks of n_1 and n_2 shifts towards the mean size of milled particles L_{mill} such that d_{32} decreases. As the particle growth proceeds, the particle size distribution reaches the starting profile, again. In consequence, the oscillation starts all over again, resulting in the wave-like movement of n_1 and n_2.

In contrast to the continuous FBLG with internal nucleation, the absolute volumes of spraying and drying zone and, thereby, the relative volume α are constant throughout the simulation due to the bed mass control.

Influence of zone formation

As indicated by the simulation, a small growth rate G induces an uniform particle growth resulting in an unstable process regime. Since the zone formation decreases the particles' surface in the granulation zone, the growth rate G is increased. In addition, the size distributions widen with respect to the zone formation. In consequence, an uneven particle growth appears. All things considered, it is expected that zone formation enhances the process stability. As a reminder, weak zone formation is characterized by the large relative size of the spraying zone α and a small residence time of particles in the drying zone τ_2. In contrast, pronounced zone formation is represented by a small α and a large τ_2.

The influence of zone formation is studied by means of bifurcation analyses. Therefore, parameter continuations are performed. For the required calculation of the corresponding steady-state solutions, the differential total material balance (3.15) is replaced by
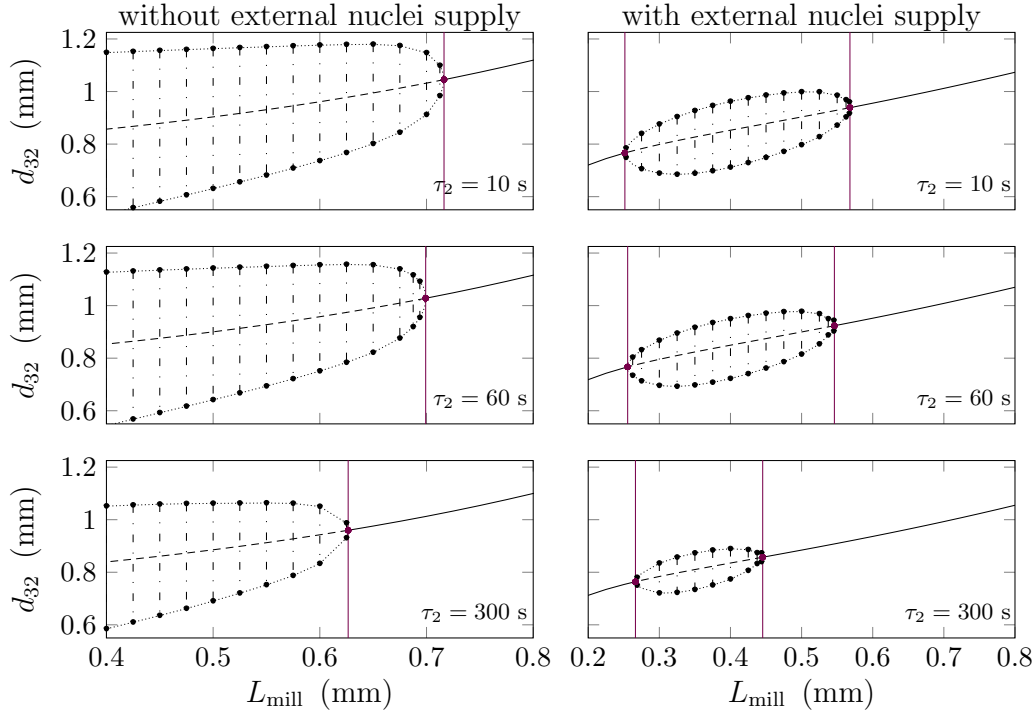
Figure 3.15.: Results of one-parameter bifurcation analyses without (**left column**) and with external nuclei supply (**right column**, $\dot{m}_{\mathrm{enuc}} = 20$ g/s) for different residence times τ_2. From top to bottom τ_2 equals 10 s, 60 s, and 300 s. Stable steady-states are indicated by solid lines, unstable steady-states along with amplitudes of corresponding limit-cycles by dash-dotted lines and black circles. The one-parameter continuation in the upper left corresponds to simulation scenario *Ext 1*. The Hopf bifurcation points are indicated by a red line and circle.

the integral material balance

$$0 = m_{\mathrm{bed}} - \frac{6\rho_{\mathrm{s}}}{\pi} \int_0^\infty L^3 \left(n_1\left(t, L \right) + n_2\left(t, L \right) \right) \mathrm{d}L \ . \tag{3.26}$$

In contrast to Equation (3.15), the introduced integral mass balance does explicitly account for the given reference value of the bed mass. It should be noted that (3.26) can be utilized for the dynamic simulations as well. This is avoided as Equation (3.26), together with (3.3) and (3.4), results in a differential-algebraic equation system with a differential index of 2. In general, this is hard to solve [12].

First, the influence of τ_2 on dynamic stability is studied employing a one-parameter bifurcation analysis. The parameter set corresponds to $\Pi_{\mathrm{ext},1}$ with the three different residence times $\tau_2 = \{10, 60, 300\}$ s. The mean diameter L_{mill} is chosen as the bifurcation parameter since the stability depends significantly on the milling. The corresponding results are presented in the left column of Figure 3.15. Here, the Sauter mean diameter d_{32} at steady-state is shown with respect to τ_2 and L_{mill}. As expected, coarse milling results in the formation of a stable steady-state indicated by the solid lines. With a
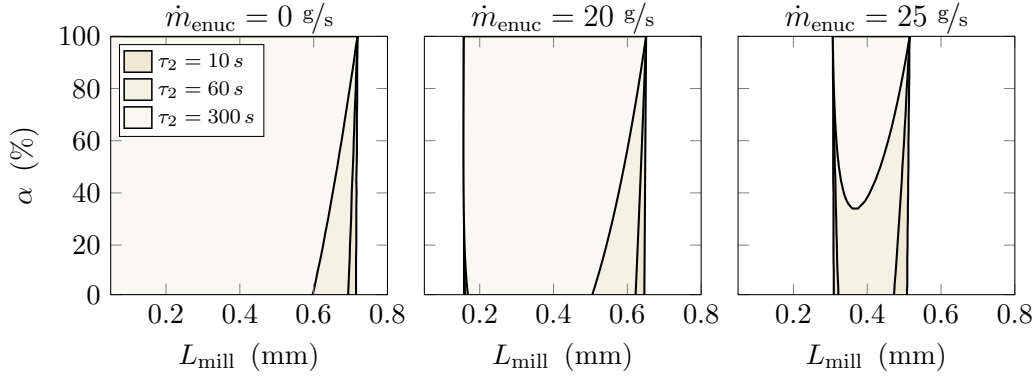
Figure 3.16.: Two-parameter stability maps in the $(L_{\mathrm{mill}}, \alpha)$-domain with respect to different feed-rates of external nuclei and residence times τ_2. From the left to the right $\dot{m}_{\mathrm{enuc}}$ equals 0 g/s, 20 g/s, and 25 g/s. Shaded domains indicate unstable steady-states.

decreasing L_{mill}, the Sauter mean diameter shrinks. In consequence, the overall particle surface is increased whereby the growth rate decreases. Consequently, the reduction of L_{mill} results in a change of the process stability at the bifurcation point: Indicated by the dashed lines, the steady-state becomes unstable and self-sustained oscillations of d_{32} arise. Thereby, the amplitudes of the corresponding limit cycles, marked by circles, increase continuously for small changes of the bifurcation parameter L_{mill}. Hence, a smooth onset of the self-sustained oscillations is observed such that the change of the qualitative process behavior is classified as supercritical Hopf bifurcation. Comparing the results of the bifurcation analysis according to the three different residence times, it becomes evident that an increase of τ_2 shifts the bifurcation point to smaller values of L_{mill}. Hence, an intensification of the zone formation improves the process stability.

This finding is corroborated by the $(L_{\mathrm{mill}}, \alpha)$-parameter domain stability map illustrated in Figure 3.16. Two-parameter bifurcation analyses determined the map for the predefined residence times τ_2. The shaded domains indicate unstable steady-states. Compared to weak zone formation, a pronounced zone formation, i.e., small α and large τ_2, increases the domain where the process is locally stable.

Influence of external nuclei

Referring to the explanation presented at the beginning of this section, the occurrence of self-sustained oscillations is motivated by the particle-recycle. Provoked by the variations of the mass fractions, the formation of nuclei by milling varies over process time inducing the oscillations of the particle size distributions n_1 and n_2. The impact of the particle-recycle can be tempered by providing external nuclei $\dot{n}_{\mathrm{enuc}}$. To demonstrate the stabilizing effect of an external nuclei supply, one-parameter and two-parameter bifurcation analyses were performed with a feed-rate of $\dot{m}_{\mathrm{enuc}} = 20$ g/s. The corresponding results are presented in the right column of Figure 3.15 and the stability map in the center of Figure 3.16. Compared to the previous results, (i) the upper bifurcation point
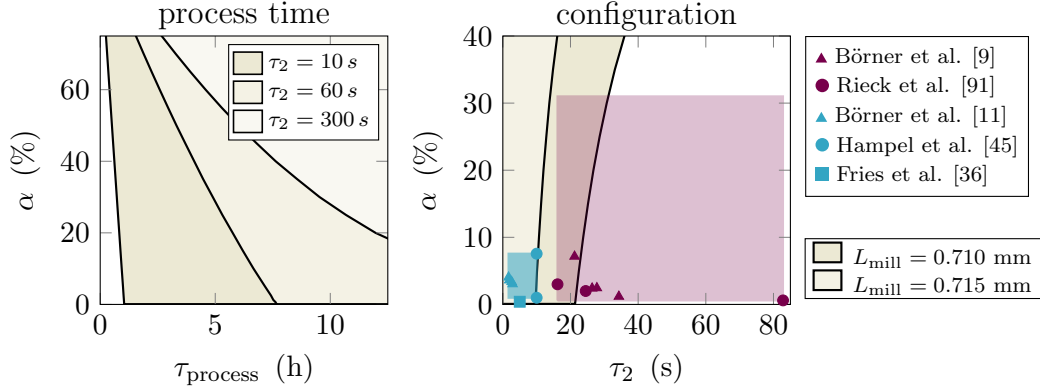
Figure 3.17.: **Left:** Stability map in the $(\tau_{\text{process}}, \alpha)$-domain with respect to different τ_2. Mean diameter of milled particles L_{mill} is set to 0.715 mm. The shaded domains represent an unstable process regime. **Right:** Stability map in the (τ_2, α)-domain with respect to different L_{mill}. Characteristic parameters of the zone formation reported in literature are marked. Explicit values are given in Table 3.6 The parameter range corresponding to top-spray configuration is highlighted in red, the domain highlighted blue represents Wurster configuration.

is shifted to smaller L_{mill}, (ii) the amplitudes of the associated self-sustained oscillations decayed, and (iii) a lower bifurcation point established such that stable steady-states arose for small L_{mill}. In consistence with previous findings of Radichkov et al. [88], the domain of unstable steady-states shrinks such that the process stability is enhanced due to the external nuclei feed. As shown by the right stability map in Figure 3.16, a further raised feed rate, here $\dot{m}_{\text{enuc}}$ is 25 g/s, still improves the dynamic stability. For a pronounce zone formation, the domain of unstable steady-states vanished. In consequence, the dynamic stability of the FBLG does not depend on the milling anymore. However, the stabilizing influence of the zone formation is still evident.

Mean particle residence time

Another adjustable operating parameter is the injection rate. An increase of $\dot{m}_{\text{inj}}$ results in a raised growth rate and, thereby, in faster particle growth. As m_{bed} is fixed to its reference value, the mean residence time, defined by

$$\tau_{\text{process}} = m_{\text{bed}}/\dot{m}_{\text{inj}} \ , \tag{3.27}$$

decreases. The enhanced particle growth leads to a widening of the particle size distribution and, thereby, to improved process stability. This finding is supported by a bifurcation analysis in the $(\tau_{\text{process}}, \alpha)$-domain. The corresponding result is presented in the left stability map of Figure 3.17: Besides a pronounced zone formation, a decreased mean residence time τ_{process} enhanced the process stability.

Table 3.6.: Characteristic parameters of zone formation α and τ_2 reported in the literature. Not reported values are indicated by $-$.

	α (%)	τ_2 (s)		α (%)	τ_2 (s)
Top-spray configuration			Wurster configuration		
Börner et al. [9]	2.40	26.4	Börner et al. [11]	3.38	2.59
	1.18	34.3		4.04	1.70
	2.45	27.8		3.04	2.88
	7.15	21.2		3.61	1.90
Dernedde et al. [21]	$[0.9, 11.9]$	——	Fries et al. [37]	0.40	5.00
Rieck et al. [91]	0.60	82.83	Hampel et al. [45]	7.56	10.0
	2.00	24.50		1.00	10.0
	3.00	16.16			
Turchiuli et al. [110]	$[0.6, 31.0]$	——			

Influence of process configuration

To interpret the stability maps from a practical point of view and to deduce information for a specific continuous granulation process, the parameters α and τ_2 have to be estimated. In general, α characterizes the apparatus design while τ_2 is a measure of the particle mixing. Both parameter depend on a manifold of process parameters. For instance, the apparatus design, the fluidization conditions [8, 9, 37], and the configuration of the nozzle [96, 110] affects α and τ_2. Thus, a precise determination of the parameters is quite challenging and not always feasible. To indicate the dependency of the dynamic stability on the process configuration nevertheless, data from literature have been collected [9, 10, 11, 21, 37, 45, 91, 110]. It should be noted that, beside Hampel et al. [45], all data are based on a batch-wise operation.

Based on simple geometric correlations, the relative size of the spraying zone was estimated for (i) top-spray configuration and (ii) Wurster configuration [121]. The corresponding parameter values are presented in Table 3.6. For details, the reader is referred to Bück et al. [15]. The derived parameter pairs are marked in the (τ_2, α)-domain stability map presented in Figure 3.17. It becomes evident that the parameter ranges of the two configurations are distinct. Compared to the top-spray configuration (highlighted in red), the Wurster configuration (blue domain) is characterized by smaller values of α and τ_2. Referring to the local stability of continuous operated FBLGs with screen-mill-cycle, the Wurster configuration tends more to instabilities than top-spray. This is in line with the concept of the Wurster configuration: As shown by experiments, this configuration guarantees a homogeneous particle growth leading to a narrow size distribution [46]. As already explained, this favors the occurrence of self-sustained oscillations.

3.4. Concluding remarks

In this chapter, the dynamics of continuous operated FBLG for different process con-
figurations were studied utilizing dynamic simulations and bifurcation analyses. Beside
other operation parameters, the impact of the zone formation on the process dynamics
was of particular interest. After a brief introduction on the formation of the spraying
and drying zone, a quite general population balance model, comprising equations (3.3)
and (3.4), was established. Based on [88, 117], the equation system was refined to ac-
count for continuous FBLG with (i) internal nucleation by thermal overspray and (ii)
nucleation by grinding oversized particles. In both cases, the interplay of nucleation and
particle growth triggers the occurrence of self-sustained oscillations. In the first config-
uration, the negative feedback of overspray and bed height reasoned the instabilities.
The loss of stability for the second configuration was motivated by an uneven formation
of nuclei, which results from variations of the oversized mass fraction. Thus, a stable
process regime demands a carefully balanced nucleation process for both configurations.

The presented results are in qualitative agreement with the experimental findings of
Schmidt et al. [92, 93, 95]. As observed in the experiments, Figure 3.9 indicates the
significant influence of the operating parameters $\dot{V}_{\mathrm{inj}}$ and L_{out} on the dynamic stability
of the FBLG with internal nucleation. For low injection rates $\dot{V}_{\mathrm{inj}}$, the continuous process
tends to instabilities. Apart from that, self-sustained oscillations of the particle size
distribution arose for an intermediate-sized separation diameter in the experiments
and the theoretical investigation. In contrast, the process is stable for small and large
valued L_{out}. Referring to Figures 3.15, 3.16, and 3.17, the stability analyses concerning
the FBLG with screen-mill-cycle proved the dependency of the process stability on the
particle milling - represented by L_{mill} - and the injection rate $\dot{V}_{\mathrm{inj}}$. This finding is
supported by the experiments presented in [92, 95].

In addition to the already mentioned experiments, Schmidt et al. [92, 94] studied the
influence of the fluidization conditions in both process configurations. In the correspond-
ing experiments, the mass-flow and temperature represent the state of the fluidization
medium. Since the introduced dynamic systems do not account for the thermal condi-
tions explicitly, a direct comparison of experimental and theoretical results is not feasi-
ble. However, variations of these operating parameters change the process parameters
related to zone formation. For instance, an intensified fluidization affects the particle
transfer between the two functional zones represented by variations of the residence
time τ_2. Hence, within certain limits, the established dynamic models are capable of
accounting for the fluidization conditions. In general, a pronounced zone formation -
i.e. small α and large τ_2 - enhances the process stability. However, as indicated by the
bifurcation analyses, the stabilizing effect of the zone formation is moderate.

The introduced population balance models reproduce the qualitative behavior of contin-
uous FBLGs. Thus, they are a solid base to gain a more in-depth insight into continuous
granulation processes. For studying the dynamics of a specific granulation process quan-
titatively, the dynamic models have to be adapted to account for the characteristics and
operating parameters of the corresponding plant. As an example, the dynamic model

of the continuous FBLG with screen-mill-cycle is refined in the upcoming Chapter 4 to fit the results of pilot-scale plant experiments.

4   Continous FBLG with screen-mill-cycle on the pilot scale

In the previous Chapter 3 population balance models capable of reproducing the different forms of the qualitative behavior of continous operated FBLGs have been developed. The upcoming chapter will show that a suitable parameterized PBM is a solid base to improve the process knowledge and to enhance the process dynamics of a specific plant. Based on experiments on the pilot-scale, the PBM of FBLG with screen-mill-cycle, presented in Section 3.3, is refined taking the plant particularities into account. Building
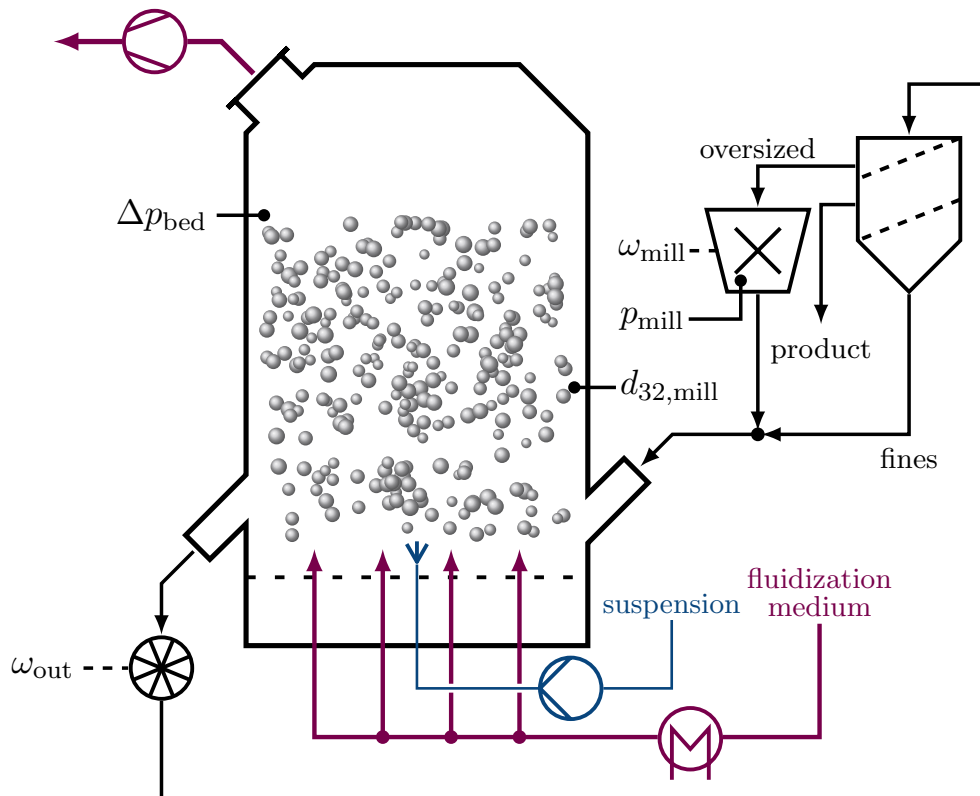
Figure 4.1.: Process scheme of FBLG with screen-mill-cycle according to experimental setup.

Figure 4.2.: Pictures of the utilized experimental equipment; The pilot-scale plant is located at Hamburg University of Technology: **Left:** Granulation chamber Procell 25 of Glatt GmbH. **Center Top:** Granulation chamber equipped with Parsum probe and sampling devise. **Center Bottom:** Impact mill equipped with pin-mill grinding inlet. **Right:** Two-deck-tumbler screen and impact mill.

upon the elaborated dynamic model, a new control concept is derived and validated by experiments. The chapter is based on the authors contribution [68] published in advance.

The remainder of the present chapter is structured as follows: First, a detailed process description is given in Section 4.1. In Section 4.2, the dynamic model of continuous FBLG is refined, considering the characteristics of the utilized plant. The focus is particularly on the milling as the particle comminution has a significant influence on the dynamics. Afterward, Section 4.3 presents the comparison of experimental and simulation results. As the steady-state operation of continuous FBLGs is a prime objective of this thesis, the focus is on (i) a constant bed mass and (ii) on a constant particle size distribution throughout an experiment. Accordingly, the first part of Section 4.3 focuses on bed mass control. In the second part, the introduced dynamic model is used to design a controller capable of dampening the oscillations of the particle size distribution and guaranteeing an operation at steady-state. The closing Section 4.4 summarizes the results and presents a brief outlook on future directions.

4.1. Experimental setup

In cooperation with the Institute of Solids Process Engineering and Particle Technology, Hamburg University of Technology, the dynamics of the continuous FBLG were
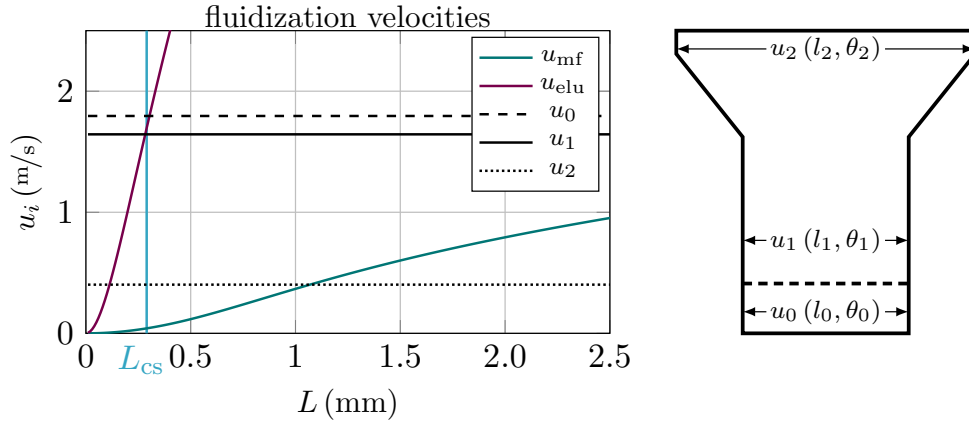
Figure 4.3.: **Left:** Velocity of the fluidization medium within the process chamber, elutriation velocity u_{elu}, and minimum fluidization velocity u_{mf} with respect to particle size L. Particles smaller than than the cut-size L_{cs} are blown out of the granulation chamber. **Right:** Cross-section of the process chamber Procell 25 of Glatt GmbH with corresponding width l_i and temperatures of the fluidization medium θ_i during the experiments: At bottom $l_0 = 0.25$ m and $\theta_0 = 85$ °C, in the process chamber $l_1 = 0.25$ m and $\theta_0 \approx 50$ °C, and at the top $l_2 = 1.0$ m and $\theta_2 \approx 45$ °C.

studied experimentally. The experiments have been carried out in a horizontal fluidized bed plant of the type Procell 25 of Glatt GmbH (Weimar, Germany) equipped with a screen-mill-cycle. Figure 4.1 presents the scheme of the utilized process configuration; Figure 4.2 shows a brief overview of the used equipment. The granulator is 1.0 m long, 0.25 m wide, and 0.25 m deep. In the presented experiments, the process is operated in a single-stage configuration characterized by uniform thermal conditions due to the intensive particle mixing. Experimental conditions for the conducted experiments are: 27.5 kg of sodium benzoate particles were fed to the granulation chamber at the beginning of each experiment. For the fluidization of the particles, ambient air was heated up to 85 °C and blown into the granulation chamber. An accurate choice of the flow rate of the fluidization medium is crucial for proper operation. If it is too low, the lack of fluidization medium induces a too small fluidization velocity u_{fluid} resulting in insufficient particle fluidization. Otherwise, u_{fluid} becomes too high for a too high flow rate leading to the blow out of the particle bed. Based on [65], Figure 4.3 presents an overview of the fluidization conditions. The domain of permissible fluidization velocities is limited by the minimum fluidization velocity u_{mf} and the elutriation velocity u_{elu}. Throughout the experimental examination, the fluidization velocity u_{fluid} was approximately 1.7 m/s.

Particles were withdrawn from the granulation chamber by the rotary valve presented in Figure 4.2. By pneumatic conveyance, the discharged particles were transported to a two-deck tumbler screen. According to the mesh-width, the particles were classified into three fractions while screening: The fine fraction consists of particles smaller than 0.8 mm, the product fraction comprises particles in the range of 0.8 mm to 1.2 mm, and the oversized fraction contains particles larger than 1.2 mm. While the product

fraction was removed from the process, the oversized fraction was milled. For grinding of the oversized particles an impact mill of type *Rekord A* of *Gebr. Jehmlich GmbH, Nossen, Germany* was utilized. As illustrated in Figure 4.2, the mill was equipped with pin-mill grinding elements. After milling, the particles were, together with the fines, re-fed to the granulation chamber.

For online monitoring of the particle sizes, the process chamber was equipped with the inline probe *IPP 70-S (Parsum GmbH, Chemnitz, Germany)*. Based on spatial filter velocimetry [85], the probe determines the chord length distribution of the measured particles. In addition to monitoring, this information can be used for control purposes. In addition, particle samples of the bed and the outlet were taken every 20 minutes. Based on digital imaging processing, the particle size distributions of those samples were determined with a CamSizer XT (Retsch Technology GmbH, Haan, Germany) in the post-processing. A short presentation of the two applied measuring methods is presented in Appendix A.

4.2. Extension of the population balance model

As, besides the dominant layering growth, all granulation mechanisms were suppressed in the experiments, the model presented in Section 3.3 is a solid foundation for modeling the dynamics of the investigated FBLG. While parts of the equation system (3.3), (3.4), and (3.12) – (3.25) can be applied directly, other model parts require refinements. Figure 4.4 presents the corresponding flow sheet and nomenclature. In the scheme, the model parts which are adjusted in the later are highlighted in red. Mainly, the flows $\dot{n}_{\mathrm{in}}$ and $\dot{n}_{\mathrm{out}}$, describing the particle exchange between the granulation chamber and periphery, are revised. Firstly, a brief overview of directly adopted parts is presented;
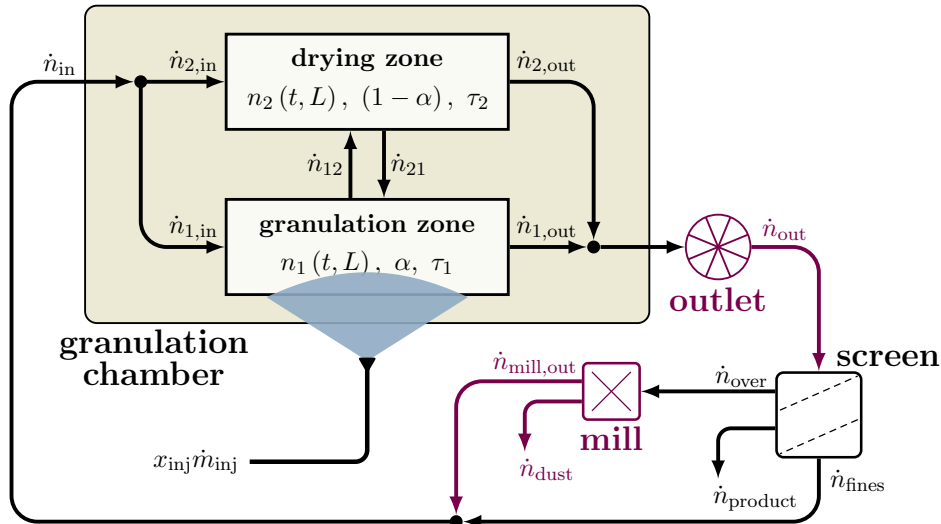
Figure 4.4.: Flow sheet of the FBLG with screen-mill-cycle. Modified model parts are highlighted in red.

secondly, the necessary modifications are motivated and presented step by step.

Due to the carefully tuned operating parameter inter nucleation can be neglected, hence the equations (3.3) and (3.4) with $\dot{n}_{1,\text{nuclei}} = \dot{n}_{2,\text{nuclei}} = 0$ apply. Assuming a population of spherical particles, Equation (3.12) describes the layering based on the assumed equal distribution of the injection on the surface of particles within the granulation zone [65]. The relative size of the granulation zone α is considered as constant over process time. Thus, Equations (3.24) and (3.25) describe the zone formation. Finally, equations (3.16) – (3.19) determine the particle screening.

The particle flow rates $\dot{n}_{\text{in}}$ and $\dot{n}_{\text{out}}$ are mainly related to the bed-mass control, the particle withdrawal, and the milling. To improve the accuracy of the predicted plant dynamics, the concerned sub-models are modified to account for the following:

(i) The ideal mass controller (3.15) is not feasible in plant experiments. Instead, a PI controller was utilized to keep the bed mass at a constant level. In consequence, the bed mass is not fixed anymore and may vary over process time.

(ii) In the conducted experiments, the representative particle removal (3.13) was not observed. Instead, larger particles were preferably withdrawn from the process chamber.

(iii) The coarse approximation of the particle milling (3.21) is not suitable to cover the actual particle comminution. In consequence, a more detailed model of the milling process was identified based on stand-alone milling experiments.

Details of the realized modifications are given in the subsequent sections.

4.2.1. Bed mass control and particle withdrawal

Particles are withdrawn from the process chamber by a rotary valve. It is assumed that the rotary speed of the valve $\omega_{\text{out}}(t)$ determines the mass flow of the discharged particles by

$$\dot{m}_{\text{out}}(t) = k_{\text{out}} \cdot \omega_{\text{out}} \qquad 0 \leq \dot{m}_{\text{out}} \leq \dot{m}_{\text{out,max}} . \tag{4.1}$$

Thus, in a first step, ω_{out} is used as manipulated variable to control the bed mass m_{bed}. As the bed mass can not be measured inline, the pressure drop across the bed Δp_{bed} is utilized as a representative. Following Litster & Ennis [56], m_{bed} and Δp_{bed} are linear correlated. Thus, the correlation

$$\Delta p_{\text{bed}} = k_{\Delta p_{\text{bed}}} m_{\text{bed}} \tag{4.2}$$

with $m_{\text{bed}} = (\pi \rho_{\text{s}}/6) \ \mu_3 (n_1(t, L) + n_2(t, L))$ is used as a first approximation. Vollmari et al. [115] showed that the shape of the particles and fluidization conditions have a significant influence on Δp_{bed} as well. Since both are assumed to be constant throughout the experiments, these effects do not need to be addressed explicitly. Based on the

pressure drop, the bed mass controlled by a PI controller according to

$$\omega_{\text{out}}\left(t\right) = k_{\text{p,out}}\left(e_{\Delta p_{\text{bed}}} + {}^{1}/{\tau_{\text{i,out}}}\int_{0}^{t}e_{\Delta p_{\text{bed}}}\mathrm{d}t\right) \tag{4.3}$$

with $0 \leq \omega_{\text{out}} \leq \omega_{\text{out,max}}$ and $e_{\Delta p_{\text{bed}}}\left(t\right) = \left(\Delta p_{\text{bed,ref}} - \Delta p_{\text{bed}}\right)$ where $\Delta p_{\text{bed,ref}}$ denotes the reference value of the pressure drop.

The flow rates of the withdrawn particles

$$\dot{n}_{\text{out}}\left(t,L\right) = \dot{n}_{1,\text{out}} + \dot{n}_{2,\text{out}} \tag{4.4}$$

$$= K_{\text{out}}T_{\text{out}}\left(n_1 + n_2\right) \tag{4.5}$$

depend on $\dot{m}_{\text{out}}$. Hence, the drain gain K_{out} follows

$$K_{\text{out}} = \frac{\left({}^{6}/{\pi\rho_{\text{s}}}\right)\dot{m}_{\text{out}}}{\mu_3\left(T_{\text{out}}\left(n_1 + n_2\right)\right)} \ . \tag{4.6}$$

The term $T_{\text{out}}\left(L_{\text{out}},\sigma_{\text{out}}\right)$ accounts for the classifying particle removal observed in the experiments. The classification is modeled by the separation function (3.10) and depends on the corresponding separation diameter L_{out} and separation sharpness σ_{out}. In deviation to the previous definition, L_{out} is not a free operating parameter. Instead, as will be shown in the upcoming Section 4.3, the separation diameter depends on the actual size distribution of the particle bed. In particular, it is assumed that L_{out} equals the characteristic value $x_{3,60}$, i.e., the size where the cumulative volume-based particle size distribution $Q_3\left(n_1 + n_2\right)$ equals 0.6:

$$Q_3\left(L = x_{3,60}\right) = \int_{0}^{x_{3,60}}\left(q_{3,1}\left(t,L\right) + q_{3,2}\left(t,L\right)\right)\mathrm{d}L = 0.6 \ . \tag{4.7}$$

The terms $q_{3,i}\left(t,L\right)$ denote the normalized volume-based particle size distribution in the corresponding zone. By screening, the withdrawn particles are classified into the fines, the product, and the oversized fraction. In the next section, the detailed model of the subsequent milling of oversized particles is presented.

4.2.2. Particle milling

> *"Milling is one of the oldest technologies developed by early civilizations, yet so little is known on what happens to the particles when they break."*
>
> Professor M. Ghadiri
> University of Leeds, UK

In general, milling of granules is a complex process. For instance, the type and configuration of the mill as well as particle properties, e.g., porosity and size, influence the particle breakage during milling significantly (Antonyuk et al. [1, 2] and Vogel & Peukert [113]). In the framework of population balance modeling, the milling can be addressed by a breakage kernel. Basically, the kernel divides into a material and a machine function [107, 114]. Due to the complex nature of the overall process, a reliable
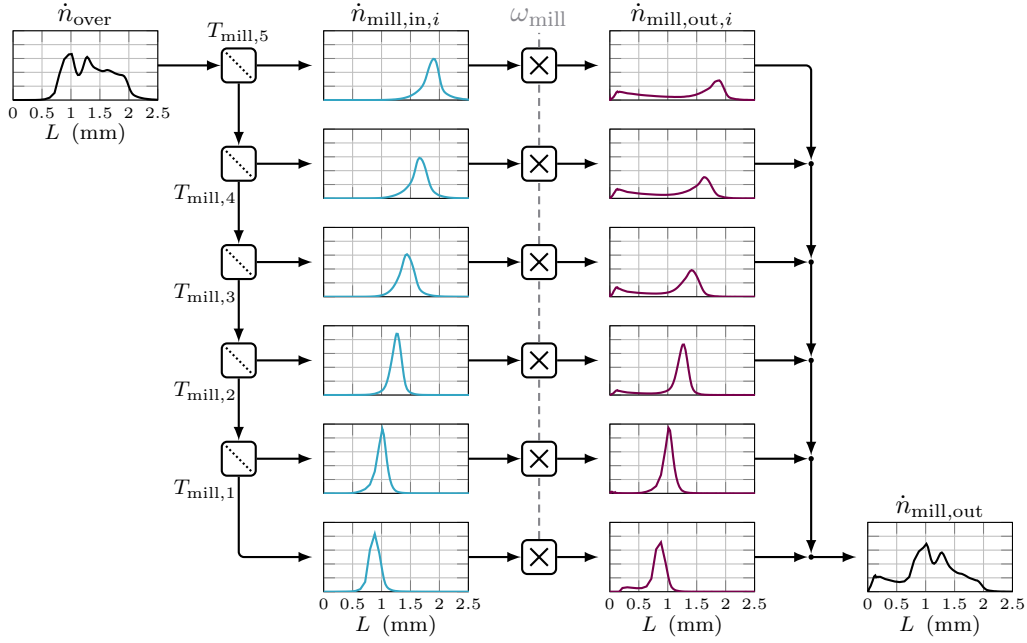
Figure 4.5.: Scheme of the size-depended particle milling: Oversized particles $\dot{n}_{\mathrm{over}}$ are classified into six fractions $\dot{n}_{\mathrm{mill,in},i}$ by separation functions $T_{\mathrm{mill},i}$. Each fraction i is milled with ω_{mill} to the corresponding $\dot{n}_{\mathrm{mill,out},i}$. Finally, the milled fractions are merged to $\dot{n}_{\mathrm{mill,out}}$.

modeling of the two functions is time and labor-intensive. Instead, an empirical milling model was established based on Neugebauer et al. [69]. In contrast to [69], the developed model accounts for the influence of the particle size distribution of the feed to the mill $\dot{n}_{\mathrm{over}}$ on the breakage. As the size distribution of milled particles cannot be measured inline, the following preliminary experimental study was performed: Particles of different sizes were classified into six fractions by screening. Afterwards, samples of 0.5 kg were milled with the relative rotational velocities $\omega_{\mathrm{mill}} = \{10, 15, 20, 25\}\,\%$, i.e., 24 experiments were performed in total. The particle size distributions of the samples were determined before and after grinding with the CamSizer XT. Based on the measurements, the separation functions of the five screens

$$T_{\mathrm{mill},i}\left(L_{\mathrm{mill},i}, \sigma_{\mathrm{mill},i}\right) = \left(1 + \left(L_{\mathrm{mill},i}/L\right)^2\right) \exp\left(\frac{\sigma_{\mathrm{mill},i}}{1 - \left(L/L_{\mathrm{mill},i}\right)^2}\right) \tag{4.8}$$

with $i \in \{1, 2, 3, 4, 5\}$ were parameterized. By measuring the corresponding samples, the normalized number-based size distributions of the milled particle fractions $q_{0,\mathrm{mill,out},i}$ were determined for the different values of ω_{mill}.

As illustrated in Figure 4.5, these quantities are the base of the detailed modeling of the milling. First, $\dot{n}_{\mathrm{over}}$ is split-up into six fractions with respect to the separation functions

$T_{\mathrm{mill},i}$. Hence, the classification of the oversized particles follows

$$\dot{n}_{\mathrm{mill,in},i}\left(t,L\right) = T_{\mathrm{mill},i-1}\prod_{j=i}^{5}\left(1-T_{\mathrm{mill},j}\right)\dot{n}_{\mathrm{over}}\ ,\quad i\in\{6,5,\ldots,2\} \qquad (4.9)$$

$$\text{and}\quad \dot{n}_{\mathrm{mill,in},1}\left(t,L\right) = \prod_{j=1}^{5}\left(1-T_{\mathrm{mill},j}\right)\dot{n}_{\mathrm{over}}\ . \qquad (4.10)$$

During the milling process, the relative mass of each fraction $k_{\mathrm{mill},i}=\mu_3\big(\dot{n}_{\mathrm{mill,in},i}\big)/\mu_3(\dot{n}_{\mathrm{over}})$ is conserved. Based on $k_{\mathrm{mill},i}$,

$$\dot{n}_{\mathrm{mill,out},i}\left(t,L\right) = \frac{k_{\mathrm{mill},i}\ q_{0,\mathrm{mill,out},i}\left(\omega_{\mathrm{mill}},L\right)}{\mu_3\left(q_{0,\mathrm{mill,out},i}\left(\omega_{\mathrm{mill}},L\right)\right)}\ . \qquad (4.11)$$

determines the flow rate of the milled particles corresponding to fraction i. With respect to ω_{mill}, the particle size distribution $q_{0,\mathrm{mill,out},i}$ are obtained by linear interpolation between available measurements. Afterward, the flows of the milled particles are merged.

Compared to the preliminary identification experiments, the continuous FBLG is characterized by a significantly increased mill throughput leading to a decrease of the milling efficiency. For that purpose, a particle bypass is introduced. The corresponding gain k_{bypass}, assumed as constant over process time, represents the fraction of uncomminuted particles of $\dot{n}_{\mathrm{over}}$ while milling. Overall, the particle flow out of the mill is given by

$$\dot{n}_{\mathrm{mill,out}}\left(t,L\right) = k_{\mathrm{bypass}}\dot{n}_{\mathrm{over}} + \left(1-k_{\mathrm{bypass}}\right)\sum_{i=1}^{6}\dot{n}_{\mathrm{mill,out},i}\ . \qquad (4.12)$$

Finally, it is assumed that too small particles - denoted as dust - are blown out of the granulation chamber. This is motivated by the fluidization conditions presented in Figure 4.3: For small particles, u_{elu} is below u_{fluid} such that the fluidization medium elutriates the corresponding particles. This phenomenon is addressed by

$$\dot{n}_{\mathrm{dust}}\left(t,L\right) = \left(1-T\left(L_{\mathrm{cs}},\sigma_{\mathrm{cs}}\right)\right)\ \dot{n}_{\mathrm{mill,out}}\ . \qquad (4.13)$$

Again, the separation function T is given by equation (3.16) with the corresponding cut-size L_{cs} and separation sharpness σ_{cs}. The remaining particles are, together with the fines, re-fed to the granulation chamber:

$$\dot{n}_{\mathrm{in}}\left(t,L\right) = \dot{n}_{\mathrm{fines}} + T\left(L_{\mathrm{cs}},\sigma_{\mathrm{cs}}\right)\ \dot{n}_{\mathrm{mill,out}}\ . \qquad (4.14)$$

With respect to the corresponding relative sizes, the recycled particles are distributed to the spraying and drying zone.

The required system parameters have been fitted to the conducted plant experiments. Table 4.1 presents the respective values.

Table 4.1.: Default operating parameter set $\Pi_{\mathrm{exp},0}$ according to the simulation study.

Parameter set $\Pi_{\mathrm{exp},0}$					
Granulation chamber			**Particle milling**		
m_{bed}	27.5	kg	k_{bypass}	0.75	
$k_{\Delta p_{\mathrm{mill}}}$	0.22	mbar/kg	L_{cs}	0.375	mm
$\dot{m}_{\mathrm{inj}}$	40.0	kg/h	σ_{cs}	0.105	mm
x_{inj}	0.35		$L_{\mathrm{mill},i}$	$[1.01, 1.14, 1.37, 1.58, 1.80]$	mm
ρ_{s}	1440	kg/m³	$\sigma_{\mathrm{mill},i}$	$[4.05, 13.44, 8.64, 8.58, 9.41]$	mm
Zone formation			**Power of mill**		
α	5.0	%		$[149.0, -3.09, -286.04, \ldots$	
τ_2	100.0	s	$\Pi_{\mathrm{mill},i}$	$\ldots\, 25.85, 0.04, -0.0008]$	
			τ_{mill}	0.10	1/s
Particle withdrawal			**Parameter of controllers**		
$k_{\mathrm{p,out}}$	-60.0	%/mm	$k_{\mathrm{p},p_{\mathrm{mill}}}$	0.005	%/W
k_{out}	2.0	kg/%·h	$\tau_{\mathrm{i},p_{\mathrm{mill}}}$	12.0	s
σ_{out}	0.75	mm	$k_{\mathrm{p},d_{32,\mathrm{bed}}}$	250.00	W/mm
$\tau_{\mathrm{i,out}}$	120.0	s	$p_{\mathrm{mill},0}$	120.00	W
$\omega_{\mathrm{out,max}}$	40.0	%	$d_{32,\mathrm{ref}}$	0.90	mm
Particle screening					
L_{I}	1.2	mm			
σ_{I}	0.125	mm			
L_{II}	0.8	mm			
σ_{II}	0.05	mm			

4.3. Experiments & simulation study

Throughout the experimental investigation, different control schemes were developed and tested. Along with Table 4.2, Figure 4.6 presents an overview of the configurations employed. In the initial experiment 1, the standard configuration of the investigated FBLG, represented by the grey box in Figure 4.6, was applied. The pin mill was operated with a constant relative rotational speed ω_{mill}. This configuration is common and was, for instance, also used by Schmidt et al. [92, 94, 95]. In the subsequent experiments 2
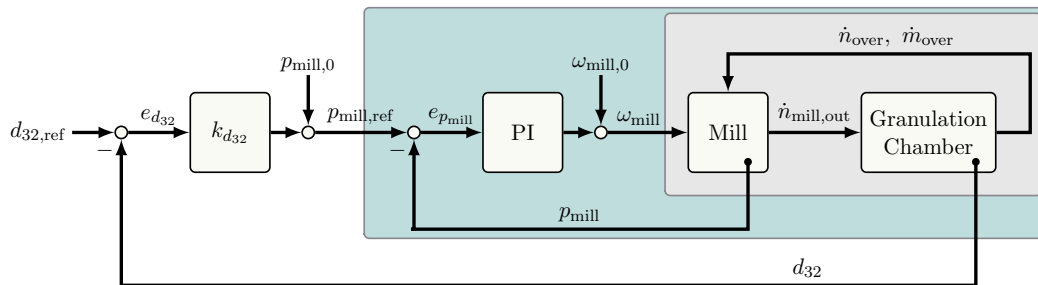
Figure 4.6.: Control schemes of the experiments: grey configuration was used in experiment 1, green configuration in experiments 2 – 4, and overall configuration in experiment 5.

Table 4.2.: Key operating parameters of the pilot-scale experiments $1 - 5$.

ID	x_{inj}	$\dot{m}_{\mathrm{inj}}$	$\theta_{\mathrm{f,in}}$	product	ω_{mill}	$p_{\mathrm{mill,ref}}$	$d_{32,\mathrm{ref}}$	Figures
1	0.35	40 $^{\mathrm{kg}}/\mathrm{h}$	85 °C	$0.8 - 1.2$ mm	17 %	—	—	$4.7 - 4.9$
2	0.35	40 $^{\mathrm{kg}}/\mathrm{h}$	85 °C	$0.8 - 1.2$ mm	—	170 W	—	4.12 & 4.13
3	0.35	40 $^{\mathrm{kg}}/\mathrm{h}$	85 °C	$0.8 - 1.2$ mm	—	140 W	—	$4.14 - 4.16$
4	0.35	40 $^{\mathrm{kg}}/\mathrm{h}$	85 °C	$0.8 - 1.2$ mm	—	120 W	—	4.17 & 4.18
5	0.35	40 $^{\mathrm{kg}}/\mathrm{h}$	85 °C	$0.8 - 1.2$ mm	—	—	1.2 mm	4.21 & 4.22

$- 4$, the mill was operated with a specific constant power p_{mill} over process time. For this purpose, a controller was developed and implemented. In Figure 4.6, the green box represents the related configuration. By varying the reference value $p_{\mathrm{mill,ref}}$, experiments $2 - 4$ illustrated the influence of the milling on the process dynamics. For the final experiment 5, the control concept was extended to the overall structure presented in Figure 4.6.

In addition to experiments $2 - 5$, simulations were carried out as a supplement. The default set of simulation parameters is given in Table 4.1. Based on the first drawn sample of the particle bed of the related experiment, the initial distributions $n_1\,(t = 0, L)$ and $n_2\,(t = 0, L)$ were determined. Therefore, the corresponding samples were measured with the CamSizer XT. The upcoming sections present the experimental data along with the simulation results in great detail.

4.3.1. Operation with constant rotational mill velocity

In the first experiment, the pin mill was operated with a constant relative rotational speed ω_{mill}. The corresponding temporal evolution of the normalized number and volume-based particle size distribution $q_{0,i}\,(t, L)$ and $q_{3,i}\,(t, L)$ of bed and outlet are presented in Figure 4.7. Oscillations with long periods characterize the temporal evolution of the size distributions.

The oscillations are also observed by monitoring the Sauter mean diameters $d_{32,\mathrm{bed}}$ and $d_{32,\mathrm{out}}$ according to the samples drawn from particle bed and outlet. As shown in Figure 4.8, $d_{32,\mathrm{out}}$ was larger than $d_{32,\mathrm{bed}}$ throughout the experiment. This deviation reveals the classifying impact of the particle-withdrawal: primarily, large particles were discharged from the granulation chamber. The classifying influence becomes evident by comparing the particle size distributions of particle bed and outlet. As an example, Figure 4.8 presents the comparison of the samples collected at $t = 12$ h.

In consequence of the oscillations of the particle size distributions, the related mass fractions of the fines x_{fines}, the product x_{product}, and the oversized particles $x_{\mathrm{oversized}}$ varied. As the bed mass m_{bed} is controlled via Δp_{bed} and ω_{out}, referring to equations (4.1) and (4.2), the oscillations of x_{product} led to variations of the mass flow of withdrawn particles $\dot{m}_{\mathrm{out}}$. Since this quantity cannot be measured online, the variations of $\dot{m}_{\mathrm{out}}$ can only be monitored via the rotational speed of the rotary valve at the outlet ω_{out}. As shown in Figure 4.9, ω_{out} varied in the range of $[0, \omega_{\mathrm{out,max}}]$ throughout the experiment.
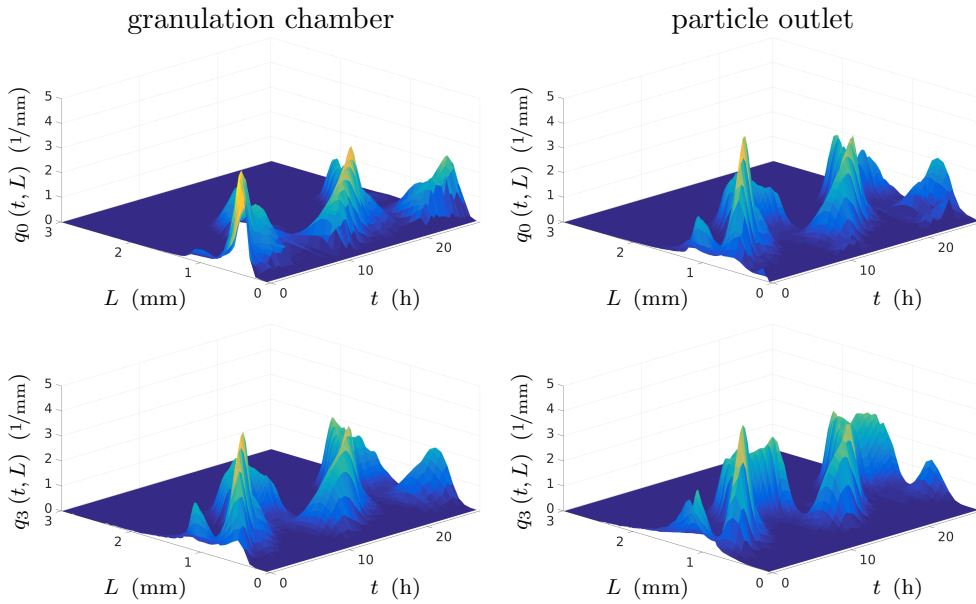
Figure 4.7.: Normalized number and volume based particle size distribution $q_0 (t, L)$ and $q_3 (t, L)$ of particles in granulation chamber and particle outlet according to experiment 1. The size distributions were determined by measuring the taken sample with a CamSizer XT.
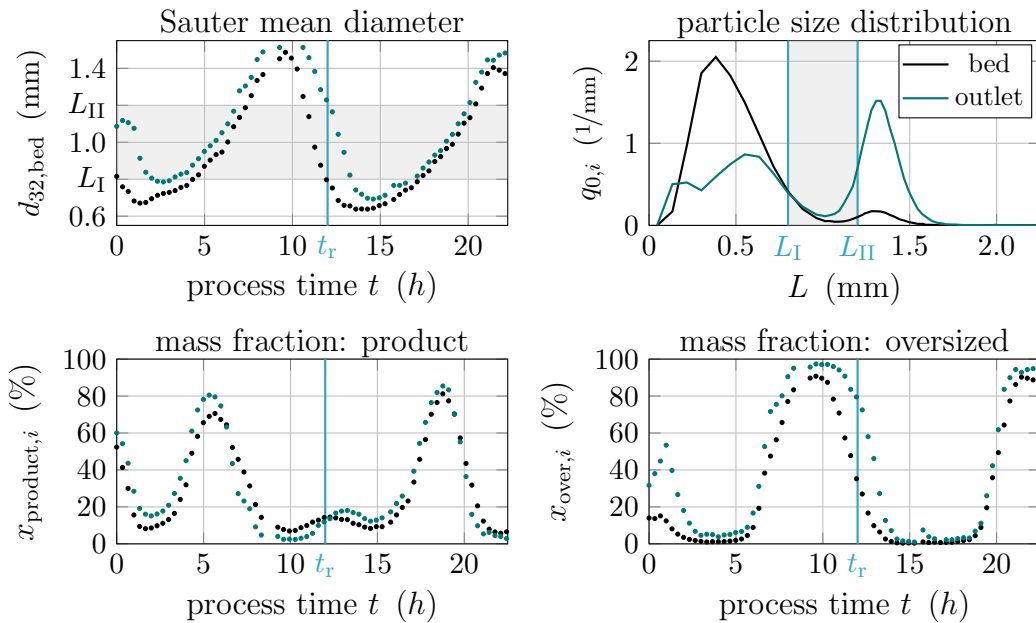
Figure 4.8.: CamSizer XT measurements corresponding to experiments 1: **Upper Left:** Sauter mean diameter of particles in granulation chamber and outlet over process time. Product range is highlighted in gray. **Upper right:** normalized particle size distribution $q_0 (t, L)$ of bed and outlet at $t = 12$ h. Product range is highlighted in gray. **Lower left and right:** mass fraction of product and oversized particles in bed and outlet.
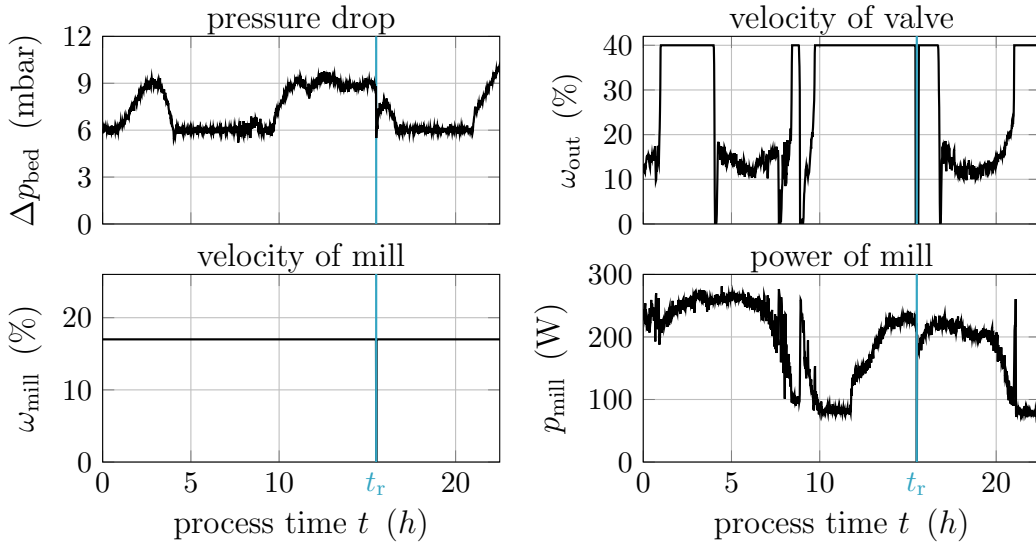
Figure 4.9.: Key data of experiment 1. The mill was operated with a constant relative velocity of $\omega_{\mathrm{mill}} = 17$ %. Alternations of p_{mill} indicate an uneven milling over process time inducing the variations of the bed mass represented by Δp_{bed} (corresponding reference value: $\Delta p_{\mathrm{bed,ref}} = 6$mbar). The experiment was interrupted at $t_{\mathrm{r}} = 15.5$ h.
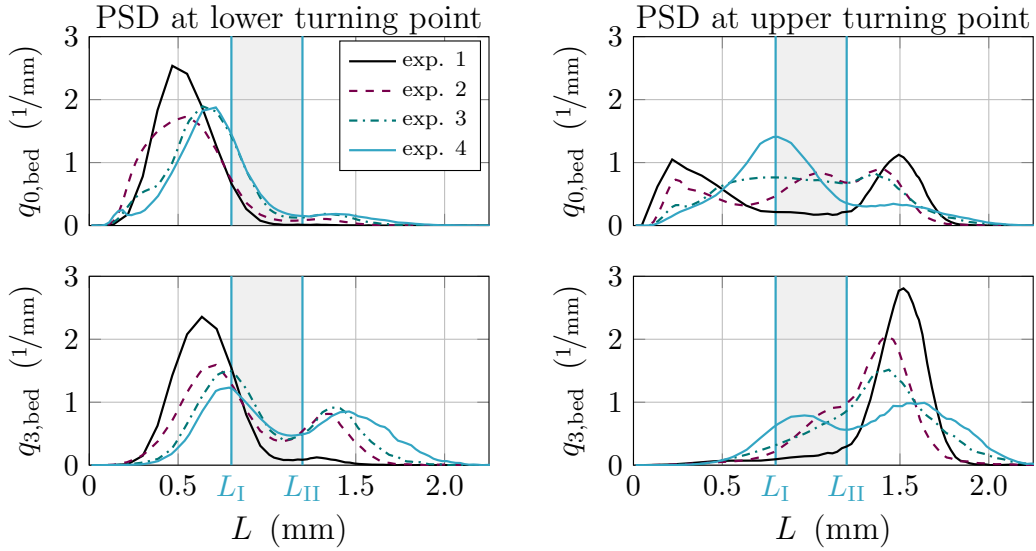
Figure 4.10.: Particle size distributions of samples at lower and upper turning point of $d_{32,\mathrm{bed}}$ for open-loop experiments 1 – 4. Corresponding sampling times: experiment 1 - 13.6 h (lower turning point) and 21.4 h (upper turning point), experiment 2 - 13.0 h and 10.6 h, experiment 3 - 33.4 h and 37.7 h, experiment 4 - 31.3 h and 35.3 h. Product range is highlighted in gray.
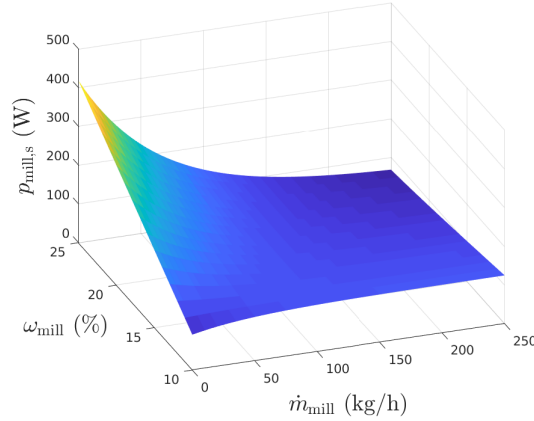
Figure 4.11.: Black box model of the power consumption of the mill: The stationary electrical power $p_{\mathrm{mill,s}}$ correlates to the relative rotational velocity of the mill ω_{mill} and the mill throughput $\dot{m}_{\mathrm{mill}}$.

Based on preliminary experiments, the upper limit $\omega_{\mathrm{out,max}}$ was found to be 40 % as a further increase of ω_{out} did not raise $\dot{m}_{\mathrm{out}}$. It is due to this restriction that not enough product particles were discharged from the FBLG. As illustrated in Figure 4.8, this was exacerbated by the classifying particle withdrawal: in the outlet, product particles were displaced by oversized particles. The insufficient product removal induced a rise of m_{bed} and, as illustrated in Figure 4.9, an increase in the pressure drop Δp_{bed}. Similar patterns of behavior were observed by Schmidt [92]. In the present case, the significantly increasing bed mass finally led to the termination of experiment 1.

Besides an increase of m_{bed}, the classifying outlet induced an overgrowing of particles in the course of the experiment. Particles of product fraction were not withdrawn from the process chamber in a sufficient quantity. In consequence, the growth proceeded such that a large number of particles entered the oversized fraction. For clarification, Figure 4.10 presents $q_{0,\mathrm{bed}}$ and $q_{3,\mathrm{bed}}$ related to local extreme values of $d_{32,\mathrm{bed}}$ - in the following denoted as turning points - for the experiments 1 – 4. Of particular interest are the modes, viz. the peaks, of the particle size distributions. Referring to the data of experiment 1, the modes of $q_{0,\mathrm{bed}}$ and $q_{3,\mathrm{bed}}$ are located in the fines fraction at the lower turning point at $t = 13.6$ h. In the progress of the experiment, the particles have grown. Accordingly, the modes shift to larger particles sizes. At $t = 21.4$ h, the upper turning point of $d_{32,\mathrm{bed}}$, the modes are placed in the oversized fraction. In consequence, the mass portion $x_{\mathrm{oversized}}$ in bed and outlet increased.

The raise of $x_{\mathrm{oversized}}$ in the particle outlet results in a higher mill throughput $\dot{m}_{\mathrm{mill}}$. As illustrated in Figure 4.9, the throughput influences the milling: An increase of $\dot{m}_{\mathrm{mill}}$, characterized by high values of ω_{out} and $x_{\mathrm{oversized}}$, led to a decrease of the electrical power consumption of the mill p_{mill}. In combination with the high maxima of $d_{32,\mathrm{bed}}$ and $d_{32,\mathrm{out}}$, this indicates the insufficient comminution of oversized particles. The uneven milling supported the overgrowing of the particles and, therefore, the occurrence of the observed oscillations.

4.3.2. Operation with constant mill power

To enable an even milling of oversized particles, feedback control was applied: By adjusting the rotational speed ω_{mill}, the mill was operated with constant power p_{mill} at a given reference value $p_{\text{mill,ref}}$. For this purpose, a PI controller was implemented and utilized. In Figure 4.6, the block diagram of the corresponding control structure is highlighted in green.

For the simulation study, the dynamic model was extended accordingly. In particular, it was assumed that a first-order lag element (PT$_1$) describes the dynamic behavior of p_{mill}. Hence,

$$\dot{p}_{\text{mill}}\left(t\right) = \left(p_{\text{mill,s}} - p_{\text{mill}}\right)/\tau_{\text{mill}} \tag{4.15}$$

with the corresponding stationary value of the electrical power $p_{\text{mill,s}}$ and time constant τ_{mill} applies. As indicated by experimental findings, $p_{\text{mill,s}}$ depends on ω_{mill} and the mass throughput $\dot{m}_{\text{mill}}$. Based on previous measurements, the correlation

$$\begin{aligned} p_{\text{mill,s}}\left(\omega_{\text{mill}}, \dot{m}_{\text{mill}}\right) = \Pi_{\text{mill},1} + \Pi_{\text{mill},2}\omega_{\text{mill}} + \dots \\ \left(\Pi_{\text{mill},3} + \Pi_{\text{mill},4}\omega_{\text{mill}}\right)\exp\left(-\left(\Pi_{\text{mill},5} + \Pi_{\text{mill},6}\omega_{\text{mill}}\right)\dot{m}_{\text{mill}}\right) \end{aligned} \tag{4.16}$$

was established by a least-square fit. The functional correlation of $p_{\text{mill,s}}$ and its arguments is presented in Figure 4.5.

As shown in the previous chapter 3.3, the process stability depends significantly on the milling: While coarse milling leads to the formation of a stable steady-state, fine milling favors the occurrence of self-sustained oscillations. By operating the mill at different power levels p_{mill}, the influence of the milling on the process dynamics is illustrated in the experiments 2 – 4. Table 4.2 presents the corresponding set-points of $p_{\text{mill,ref}}$. High values of $p_{\text{mill,ref}}$ represent fine milling; small values account for coarser milling. Throughout the experiments 2 – 4, the classifying effect of the particle withdrawal described in the previous section is observed again.

Figures 4.12 and 4.13 present the results of experiment 2. Here, the mill was operated with $p_{\text{mill,ref}} = 175$ W. Again, $q_{0,\text{bed}}$ and $q_{3,\text{bed}}$ are characterized by oscillations. In contrast to experiment 1, the measured particle size distributions are more compact. As shown in Figure 4.10, the distance between the modes of $q_{0,\text{bed}}$ and $q_{3,\text{bed}}$ at lower ($t = 13.0$ h) and upper turning point of $d_{32,\text{bed}}$ ($t = 10.6$ h) narrowed as well as the amplitudes of the corresponding modes decreased. As depicted in Figure 4.13, this leads to a decrease in the amplitudes of $d_{32,\text{bed}}$. In consequence of the compacter particle size distributions over process time, the mass portion of the product fraction is of sufficient size throughout the experiment. Thus, the adequate product removal from the FBLG is guaranteed such that, as monitored by the pressure drop Δp_{bed}, the bed mass m_{bed} is constant over process time. However, the intensive milling induced the formation of a large number of nuclei. Following the numerical stability analyses presented in Section 3.3, this leads to the formation of self-sustained oscillation of the particle size distribution. Hence, it was not expected that the process settles at steady-state. Its for that reason that the experiment was terminated at $t = 17$ h.

Figure 4.12.: **Left Column:** normalized number and volume based particle size distributions $q_{0,\mathrm{bed}}$ and $q_{3,\mathrm{bed}}$ according to experiment 2. PSDs were determined with CamSizer XT. **Right Column:** PSDs of the corresponding simulation.

Figure 4.13.: Comparison of key data of experiment 2 (black line) and the corresponding simulation results (green line). The mill was operated with a constant power of 175 W by manipulating ω_{mill}. The constant level of the pressure drops Δp_{bed} indicates a constant bed mass m_{bed} throughout the experiment. The Sauter mean diameter bases on the PSDs presented in Figure 4.12. The observed self-sustained oscillations of the PSDs result in nonlinear oscillations of $d_{32,\mathrm{bed}}$.
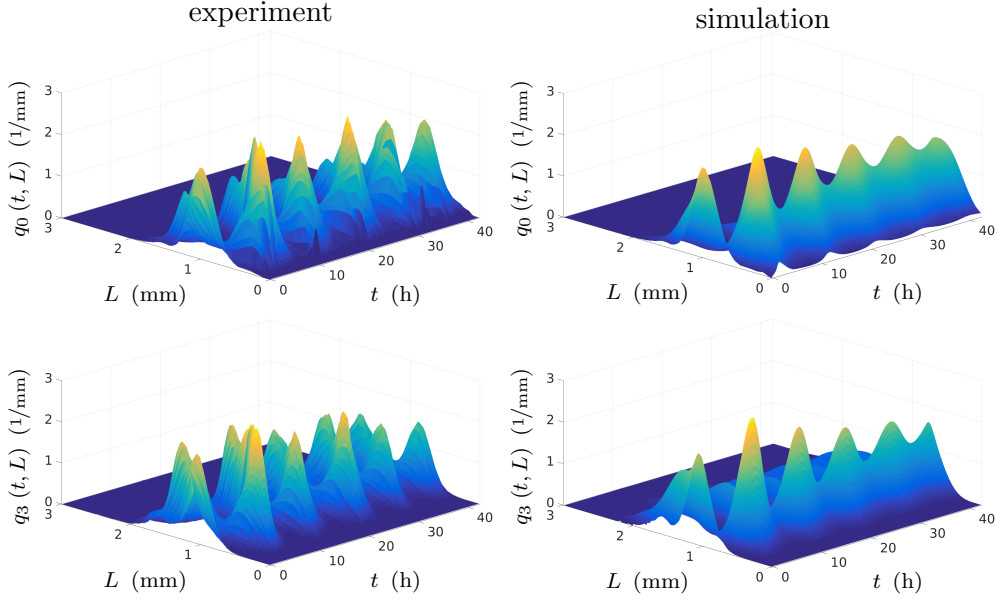
Figure 4.14.: **Left Column:** normalized number and volume based particle size distributions $q_{0,\text{bed}}$ and $q_{3,\text{bed}}$ according to experiment 3. PSDs were determined with CamSizer XT. **Right Column:** PSDs of the corresponding simulation.
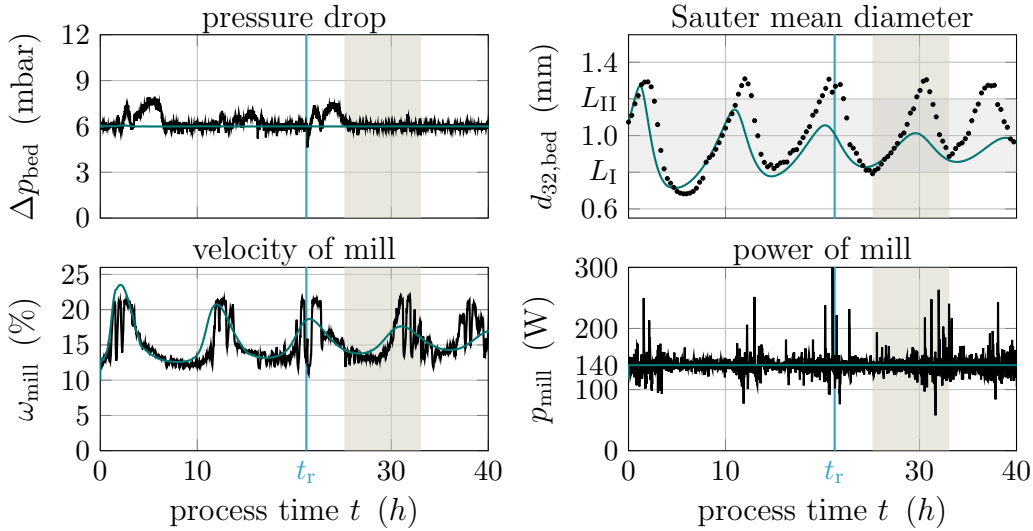
Figure 4.15.: Comparison of key data of experiment 3 (black line) and the corresponding simulation results (green line). The mill was operated with a constant power of 140 W by manipulating ω_{mill}. The constant level of the pressure drops Δp_{bed} indicates a constant bed mass m_{bed} throughout the experiment. The Sauter mean diameter, based on the PSDs presented in Figure 4.14, is characterized by slowly decaying, non-linear oscillations. The highlighted time interval corresponds to the limit-cycle presented in Figure 4.16. At $t_{\text{r}} = 21.25$ h, the experiment was interrupted.
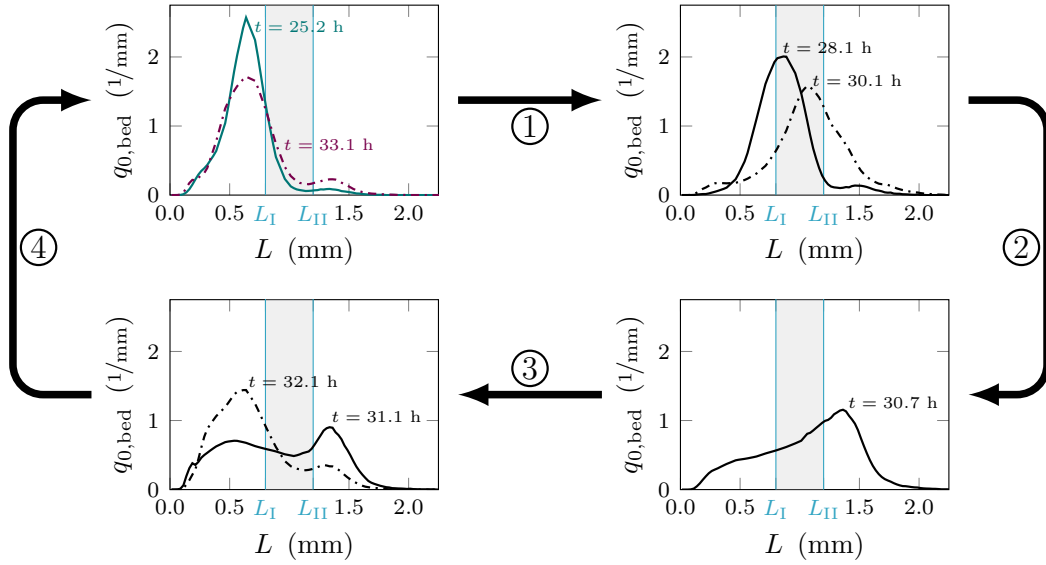
Figure 4.16.: Oscillation of the normalized particle size distribution $q_{0,\text{bed}}$ observed in experiment 3. Correlated to the highlighted time interval in Figure 4.15, the oscillations starts at $t = 25.2\,\text{h}$ and ends at $t = 33.1\,\text{h}$. The highlighted domain represents the product fraction.

In the subsequent experiment 3, the reference value of the mill power $p_{\text{mill,ref}}$ was reduced to 140 W. Due to the runtime of 40 h, the experiment was interrupted and restarted at $t = 21.25\,\text{h}$. The Figures 4.14 and 4.15 present $q_{0,\text{bed}}$, $q_{3,\text{bed}}$, and key process states related to experiment 3. Once again, the process is operated at a constant level of Δp_{bed}.

The reduction of $p_{\text{mill,ref}}$ results in a coarser particle milling. In line with the theoretical predictions, see Section 3.3, the coarser milling enhanced the process stability. Referring to the particle size distributions related to consecutive minima of $d_{32,\text{bed}}$, the oscillations of $q_{0,\text{bed}}$ are slightly dampened. As an example, the upper left plot of Figure 4.16 presents the normalized size distributions of the samples collected at $t = 25.2\,\text{h}$ and $t = 33.4\,\text{h}$. Besides, Figure 4.16 illustrates the corresponding oscillation of $q_{0,\text{bed}}$ in the time interval $[25.2, 33.4]$ h. In contrast to the limit-cycle related to the not refined population balance model, see Figure 3.14, the modes of the particles size distribution passed through the product fraction and entered the oversized fraction. However, the interplay of overgrowing and the formation of nuclei by milling, inducing the occurrence of oscillations, is evident.

Compared to experiment 2, the modes of $q_{0,\text{bed}}$ and $q_{3,\text{bed}}$ shifted to a larger particle size L at the lower turning point of $d_{32,\text{bed}}$ at $t = 33.4\,\text{h}$ as presented in Figure 4.10. The compacter particle size distribution leads to an evener formation of nuclei throughout the experiment resulting in the slow decay of the observed oscillations.

In the next experiment, $p_{\text{mill,ref}}$ was reduced to 120 W. Figures 4.17 and 4.18 present the related particle size distributions and key process states. This time, the experiment
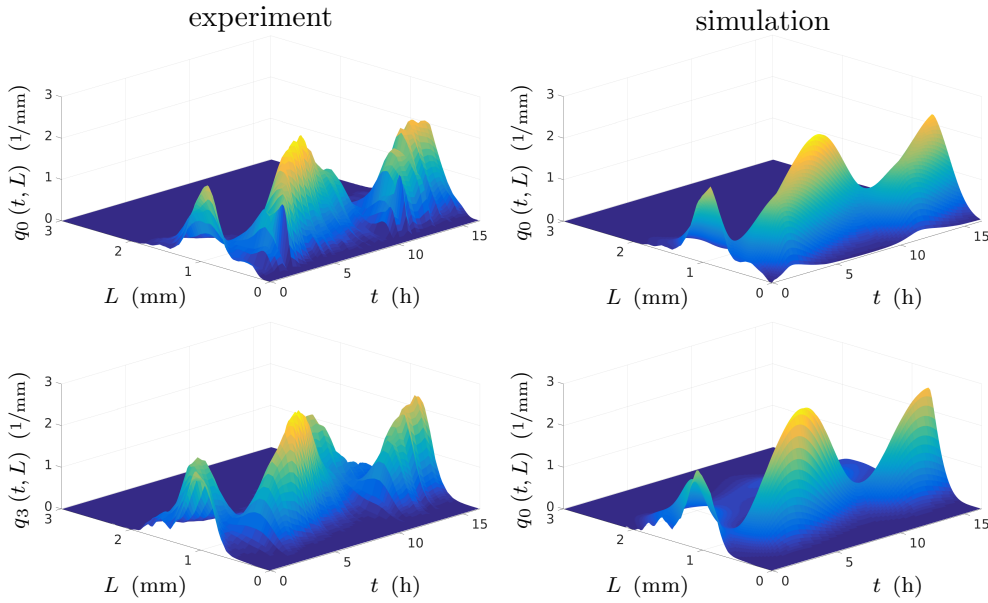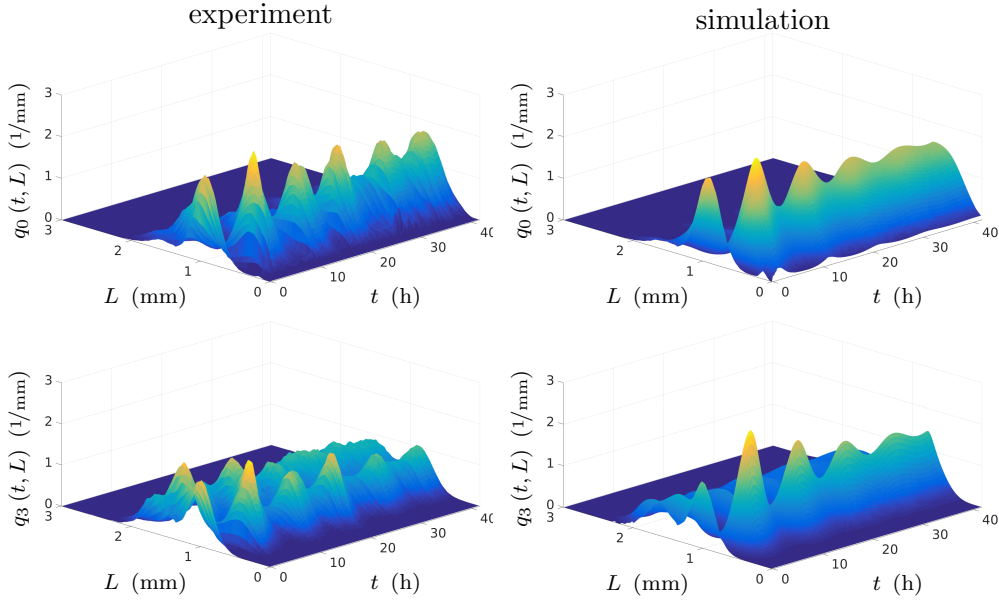
Figure 4.17.: **Left Column:** normalized number and volume based particle size distributions $q_{0,\text{bed}}$ and $q_{3,\text{bed}}$ according to experiment 4. PSDs were determined with CamSizer XT. **Right Column:** PSDs of the corresponding simulation.
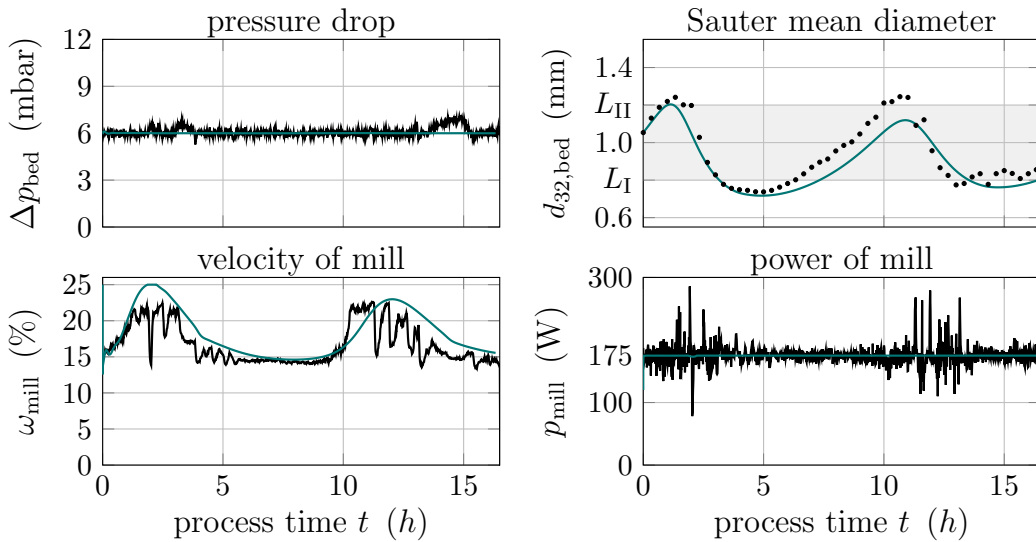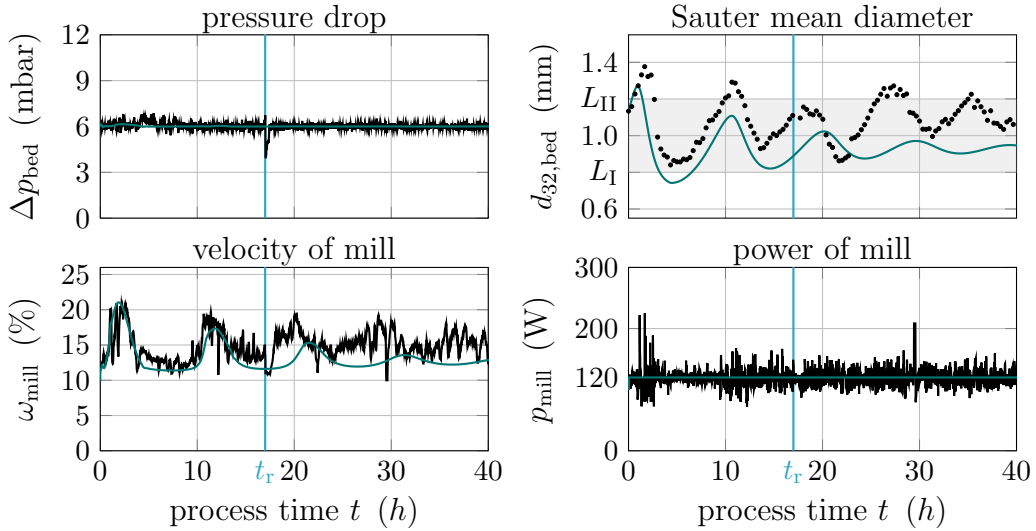

Figure 4.18.: Comparison of key data of experiment 4 (black line) and the corresponding simulation results (green line). The mill was operated with a constant power of 120 W by manipulating ω_{mill}. The constant level of the pressure drops Δp_{bed} indicates a constant bed mass m_{bed} throughout the experiment. The Sauter mean diameter, based on the PSDs presented in Figure 4.17, is characterized by decaying, non-linear oscillations. At $t_{\text{r}} = 17.0$ h, the experiment was interrupted.

was interrupted and restarted at $t = 17$ h. Compared to the previous experiments, the oscillations are more dampened in experiment 4. In consequence, the deviations between the particle size distributions corresponding to the lower and upper turning point of $d_{32,\text{bed}}$, sampling times are $t = 31.3$ h and $t = 35.3$ h, are small. Referring to Figure 4.10, the deviation between the size distributions decreased in comparison to experiments 1 – 3.

For the further course of the experiment, it is expected that these deviations would vanish. In consequence, the process would reach stable steady-state conditions characterized by a constant bed mass m_{bed} and a stationary profile of the normalized particle size distributions. However, even after a long process time, the settling to the steady-state was not achieved due to the oscillatory behavior. Also, process disturbances may aggravate the settling. Hence, the experiment was terminated at $t = 40$ h.

Throughout this section, the experimental data are compared to predictions based on the dynamic model presented in Section 4.2. Except for the respective reference values $p_{\text{mill,ref}}$, the simulations share the default parameter set given in Table 4.1. Overall, experimental findings and simulation results are in reasonable agreement. Referring to Figure 4.12, 4.14, and 4.17, the maximum values of the normalized particle size distributions and the periods of the corresponding oscillations are at the same level. In results, the measured and simulated size distributions $q_{0,\text{bed}}$ and $q_{3,\text{bed}}$ have similar shapes. Furthermore, as presented in Figures 4.13, 4.15, and 4.18, the simulation results of p_{mill} and ω_{mill} are in good agreement with experimental data.

Summarizing the simulation results, the developed dynamic model is capable of reproducing the observed different dynamics with respect to the milling power: While large values of $p_{\text{mill,ref}}$ lead to the formation of oscillations of $q_{0,\text{bed}}$ and $q_{3,\text{bed}}$, characterized by large amplitudes, slowly decaying oscillations are observed for smaller values of $p_{\text{mill,ref}}$.

4.3.3. Cascade control

In the previous experiments, a stable steady-state operation was not achieved. Even if the FBLG was operated at a constant bed mass m_{bed}, (slow decaying) oscillations characterized the particle size distributions. To enhance the process dynamics and establish the steady-state operation, a cascade controller was designed. According to Figure 4.6, the control structure was extended: By manipulating the reference value of the mill power $p_{\text{mill,ref}}$, the introduced outer loop controls the Sauter mean diameter $d_{32,\text{bed}}$. Since the simulations reproduce the experiments with sufficient accuracy, the dynamic model presented in Sections 4.2 and 4.3.2 is a good base for the controller design. First, the dynamic model was numerically linearized at the stationary state related to the parameter set representing experiment 4. In the vicinity of the corresponding steady-state, the resultant linear time-invariant transfer function $G_{\text{nom}}(s)$ - commonly denoted as LTI system - relates the dynamics of the input signal $p_{\text{mill,ref}}$ to the dynamics of output variable $d_{32,\text{bed}}$. The nominal transfer function $G_{\text{nom}}(s)$ is of order 403. By balanced truncation [100], the full-order system was reduced to a system of order 5. Referring

to Figure 4.19, the bode plot of the reduced system $G_{\mathrm{red}}(s)$ is in good agreement with the bode plot of the nominal system $G_{\mathrm{nom}}(s)$.

Based on the transfer function $G_{\mathrm{red}}(s)$, a feedback controller was designed by the root-locus method [24, 33]. In brief, the root-loci represent the poles of the closed-loop LTI system

$$G_{\mathrm{cl}}(s) = {}^{kG_{\mathrm{ol}}(s)}/{}_{1+kG_{\mathrm{ol}}(s)} \tag{4.17}$$

in the complex plane in dependency of the controller gain k. Starting at the pole of the open-loop system $G_{\mathrm{ol}}(s)$, viz. $k = 0$, the poles according to $G_{\mathrm{cl}}(s)$ move along the root-loci towards the zeros of $G_{\mathrm{ol}}(s)$ for an increasing control gain k. For a stable closed-loop system it is mandatory that all poles of $G_{\mathrm{cl}}(s)$ are located in the left half-plane.

Figure 4.20 presents the root-loci corresponding to $G_{\mathrm{red}}(s)$ controlled by a P controller (left) and a PI controller (right). Regarding the stationary accuracy of the steady-state, open-loop systems $G_{\mathrm{ol}}(s)$ with integral actions - for instance, provided by the application of a PI controller - are preferred in general. In this specific case, the application of a PI controller is not suitable. Due to the open-loop pole at the origin, introduced by the integral part of the PI controller, a branch of the root-loci lies entirely in the right half-plane. Hence, a closed-loop pole is located in the right half-plane for arbitrary control gains $k_{d_{32}}$. Thus, a PI controller is not capable of stabilizing the dynamic system $G_{\mathrm{red}}(s)$. In contrast, the root-loci related to the P controlled system predicts a stable closed-loop behavior and dampening for suitable control gains $k_{d_{32}}$. Furthermore, it is expected that the controller is capable of stabilizing the process even if the open-loop dynamics are unstable, e.g., the pair of complex poles close to the imaginary axis shifts from the left to right half-plane. For instance, an increase of $p_{\mathrm{mill,ref}}$ may lead to the described pole shift and, thereby, induce the loss of stability of the open-loop system.

For the validation of the P controller, the corresponding non-linear dynamic model was extended by the controller according to

$$p_{\mathrm{mill,ref}}(t) = k_{d_{32}} e_{d_{32}} + p_{\mathrm{mill},0} \tag{4.18}$$

where the deviation between the reference value and the actual value of the Sauter mean diameter determines the control error $e_{d_{32}} = d_{32,\mathrm{ref}} - d_{32,\mathrm{bed}}$. As simulation results, presented in Appendix C, were promising, the control strategy was tested at the plant in experiment 5. For measuring the required $d_{32,\mathrm{bed}}$, the equipped inline probe Parsum IPP 70-S was used. Along with the simulation results, Figure 4.21 and 4.22 present the experimental data. Again, they are in good agreement. Due to the extended control strategy, oscillations of the particle size distributions and, in consequence, of the Sauter mean diameter $d_{32,\mathrm{bed}}$ are dampened within a short period. In results, as the bed mass m_{bed} is constant as well, a steady-state operation was achieved within approximately 5 hours. Compared to the previous experiment 4 presented in Figure 4.17 and 4.18 - where steady-state conditions were not achieved within the first 40 hours of process time - the process dynamics were significantly enhanced.
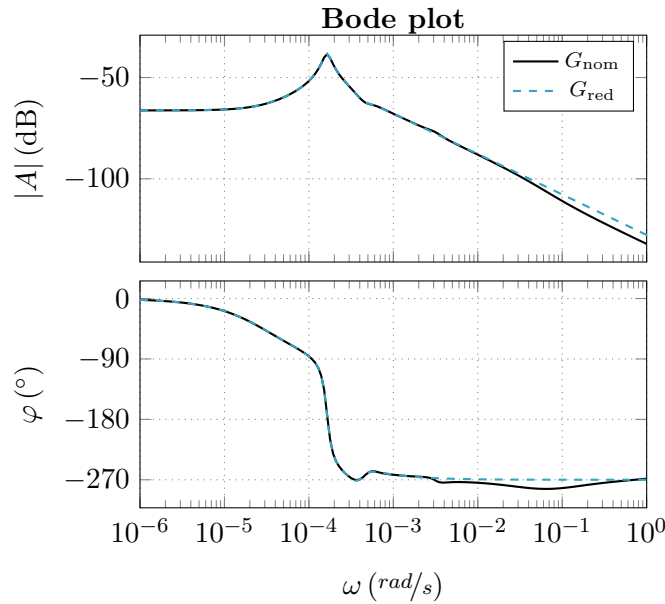
Figure 4.19.: Bode plots of the full order system $G_{\mathrm{nom}}(s)$ and the reduced system $G_{\mathrm{red}}(s)$ of order 5.
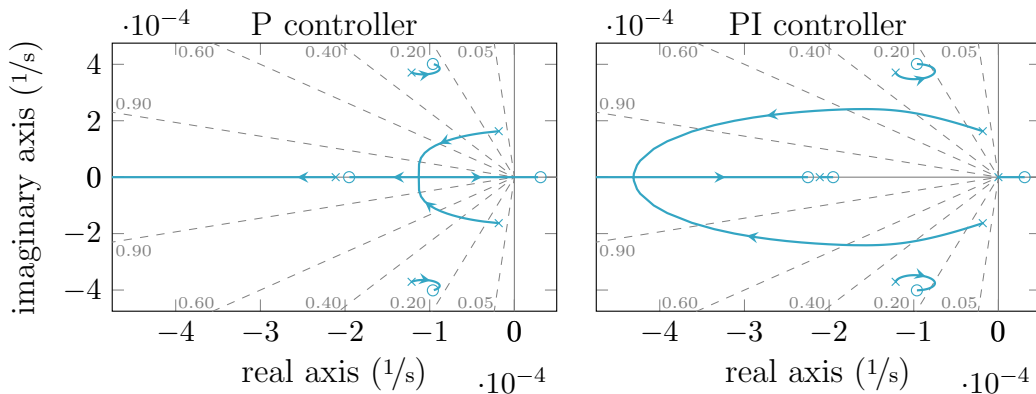
Figure 4.20.: The root-locus of the closed-loop system $G_{\mathrm{cl}}(s)$ with respect to controller gain $k_{d_{32}}$. Poles of $G_{\mathrm{ol}}(s)$ are indicated by x, the according zeros by o. The damping ratios of $G_{\mathrm{cl}}(s)$ are specified in gray. **Left:** A suitable tuned P controller $k_{d_{32}}$ increases the damping ratio of $G_{\mathrm{cl}}(s)$ and guarantees a stable steady-state operation. **Right:** Due to the pole introduced at the origin, one pole of the PI controlled closed-loop system is in the right half-plane. Hence, $G_{\mathrm{cl}}(s)$ is unstable for all $k_{d_{32}}$.
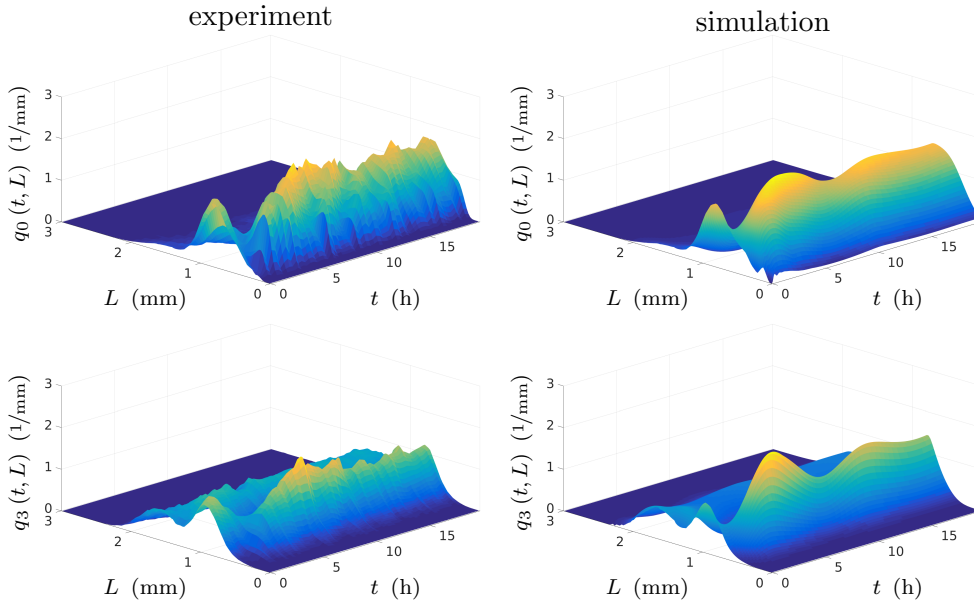
Figure 4.21.: **Left Column:** normalized number and volume based particle size distributions $q_{0,\text{bed}}$ and $q_{3,\text{bed}}$ according to experiment 5. PSDs were determined with CamSizer XT. **Right Column:** PSDs of the corresponding simulation.
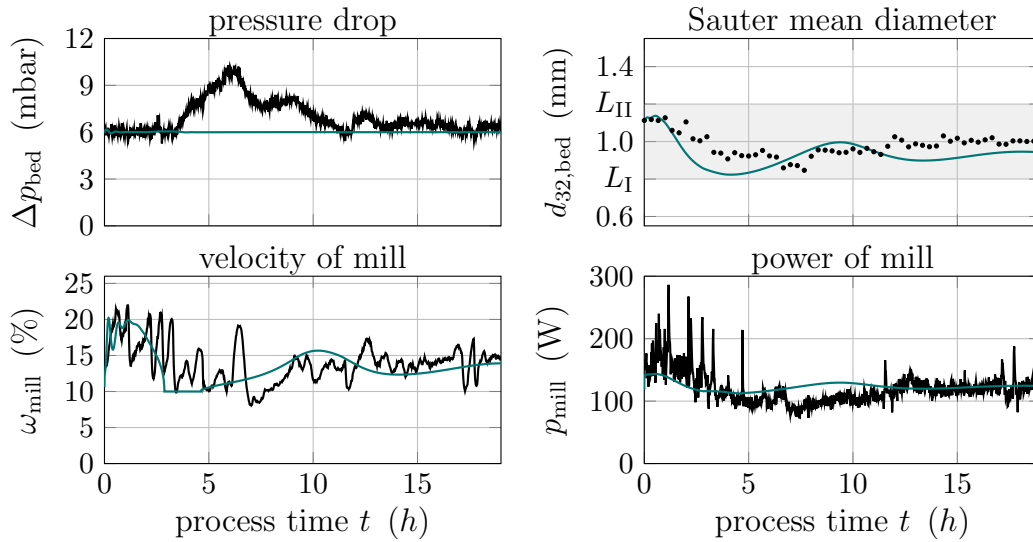
Figure 4.22.: Comparison of key data of experiment 5 (black line) and the corresponding simulation results (green line). As presented in Figure 4.6, the process is controlled based on the inline measured PSD. The process settles, after a sufficient process time t, at steady-state characterized by a constant pressure drop Δp_{bed} and Sauter mean diameter $d_{32,\text{bed}}$.

4.4. Concluding remarks

Based on the theoretical findings presented in Chapter 3, the process dynamics of a specific granulation plant were investigated in quantitatively in the current chapter. For the first time, the dynamics of a continuously operated fluidized bed layering granulation with screen-mill cycle were studied by pilot-scale experiments accompanied by a simulation study based on a population balance model. Firstly, the dynamic model presented in Section 3.3 was extended to account for the plant characteristics. In particular, a detailed model of the milling process was derived. Subsequently, the results of the experimental study were presented. Within the experiments, different approaches to control the milling process were tested. In experiment 1, the mill was operated with a constant rotary velocity ω_{mill}. This default configuration was not capable of operating the process with constant bed mass m_{bed} nor constant particle size distributions. As experiment 1 indicated uneven particle comminution, a controller was designed to enhance the milling: By manipulating ω_{mill}, the mill was operated at constant power p_{mill}. Throughout the related experiments 2 – 4, the bed mass m_{bed}, represented by the pressure drop over the bed Δp_{bed}, was at a constant level. The experiments confirmed the theoretical findings of Section 3.3: Intense milling, viz. high values of p_{mill}, resulted in self-sustained oscillations of the particle size distributions characterized by large amplitudes. In contrast, the observed oscillations were slowly decaying for coarser milling. However, due to the slow process dynamics and process disturbances, steady-state conditions were not achieved in experiments 2 – 4.

The control structure was extended by an outer control loop to accomplish a faster transition to steady-state operation. By utilizing the derived cascade control in experiment 5, it was shown for the first time that feedback control is capable of enhancing the process dynamics of continuous FBLGs. Within a short time, a constant bed mass m_{bed} and stationary profiles of the particle size distributions $q_{0,\text{bed}}$ and $q_{3,\text{bed}}$ throughout process time were achieved. Hence, the process settled at steady-state.

The experimental study showed that - even relatively simple - feedback control strategies are capable of enhancing the process dynamics significantly. By this, they are, among other things, a valuable tool to examine the influence of different process configurations and operating parameters on the process dynamics and product properties through experiments within a short time. In combination with on- and offline estimations [30, 72, 82] and monitoring methods [13, 17, 76] the experiments can be used for refinements of the developed dynamic model and thus to enhance the process understanding. For instance, the influence of thermal conditions and multi-stage operation influences on product properties and process dynamics is of particular interest.

As simulation results are in good agreement with experimental data, the extended population balance models is an ideal basis for the design of advanced control strategies for the presented granulation process. Various simulation studies showed that robust [79, 80] and adaptive control strategies [74, 77], model predictive control [14, 16], nonlinear control approaches [75, 78, 81], and multiple input multiple output controller [20, 83] are promising to improve the performance of FBLG processes further.

5 Influence of thermal conditions and advanced control concepts

Depending on the intended purpose and down-stream processes, different product specifications are required in granulation processes. So far, the presented population balance models were only capable of accounting for a single particle property: the particle size L. However, it is evident that further characteristics are relevant as well. As shown by experimental studies [23, 50, 91], several particle properties, e.g., porosity and moisture, depend significantly on the thermal conditions of the fluidization medium. Hence, the dynamic models have to be extended to consider the influence of the thermal conditions on the product properties.

First, Section 5.1 motivates the model extensions presented in the subsequent Section 5.2. To account for the particle growth and the thermal conditions, the derived model consists of a population balance model and a system of ordinary differential equations. The influence of the thermal conditions on product properties and process dynamics is illustrated by simulations and stability analyses in Section 5.3. It becomes evident that the formation of tailor-made particles under steady-state conditions demands new control concepts. In the following Sections 5.4 and 5.5, different control strategies are designed and tested by means of simulation. Finally, Sections 5.6 introduces the multi-stage configuration that provides, compared to single-stage FBLG, new degrees of freedom to influence process dynamics and product properties. The chapter is based on the contributions Neugebauer et al. [66, 67, 71].

5.1. Motivation

In the majority of cases, granules are an intermediate product in a process chain. Thus, subsequent process steps demand specific particle properties. For example, a minimum strength avoids particle breakage and dust formation during the transport [2]. Otherwise, solubility is a crucial feature if granules are dissolved at a later stage [60]. Following Litster et al. [56], the key properties of a granule are the corresponding size and porosity. The remaining properties depend directly on one or the other.

By means of experiments with sodium benzoate, Rieck et al. [91] and Hoffmann et al.
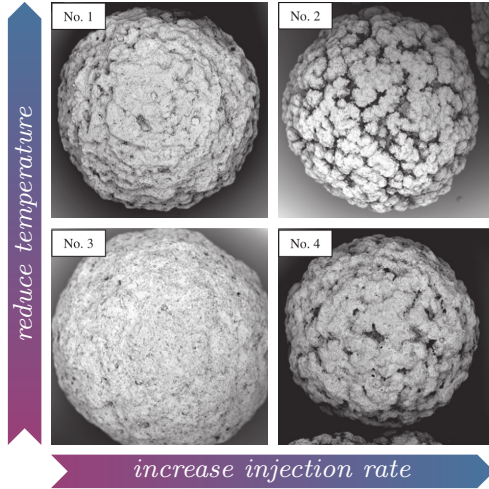
Figure 5.1.: Influence of drying conditions on layer porosity as presented in [91]: glass particles coated with sodium benzoate according to operating parameters presented in Table 5.1.
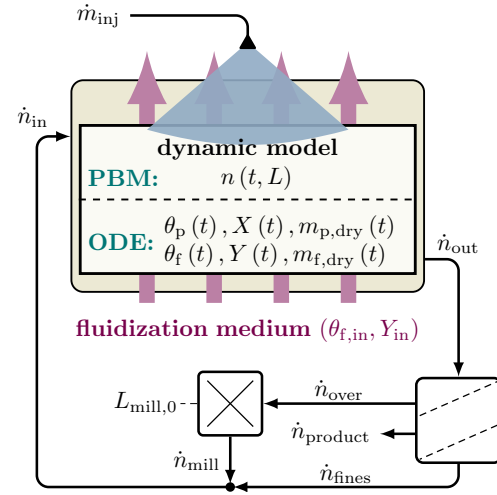
Figure 5.2.: Flow sheet of the investigated FBLG : The dynamic model consists of a PBM and a system of ordinary differential equations.

[50] showed that the operating parameter affects the porosity of the particles' shell ϵ_{shell} and, over process time, the apparent particle porosity ϵ_{p}. As illustrated in Figure 5.1 - the presented pictures of the particles originate from Rieck et al. [91] - intense drying conditions, here represented by a low injection rate $\dot{V}_{\text{inj}}$ and a high temperature of the fluidization medium $\theta_{\text{f,in}}$, leads to compact particles with a smooth surface. On the contrary, moderate drying conditions, viz. high injection rate $\dot{V}_{\text{inj}}$ and small temperature $\theta_{\text{f,in}}$, result in a rough surface. Hence, the porosity ϵ_{shell} is small for intense and high for moderate drying conditions. To clarify this observation, Sondej et al. [104] studied the underlying solidification process, in particular a crystallization, in great detail. By drying a sessile sodium benzoate droplet, the influence of selected operating parameters on the structure of the deposits was investigated. In the conducted experiments it was shown that porosity and the footprint of the remaining salt deposit depend significantly on the initial sodium benzoate concentration of the droplet as well as on the thermal conditions of the surrounding fluidization medium.

To represent the thermal conditions within the FBLG, Rieck et al. [91] introduced the drying potential η. For fluidized bed layering granulation, a linear relation between the drying potential η and the porosity of the particle shell ϵ_{shell} was found experimentally [50, 91]. In the corresponding experiments, a sodium benzoate solution was injected by a nozzle mounted in top spray configuration onto a particle bed. Diez et al. [23] showed that the linear correlation between ϵ_{shell} and η also holds for bottom spray configuration.

As the population balance models presented so far do not consider the thermal condi-

tions of the FBLG, they are not capable of determining the drying potential η. Hence, the dynamic models neither can predict the shell porosities $\epsilon_{\mathrm{shell}}$ nor the apparent particle porosity ϵ_{p}. Furthermore, the models do not account for the impact of the thermal conditions on the dynamics proven by experiments [94]. To overcome these shortcomings, an extended dynamic model of the FBLG is derived in the subsequent section. The derived model is applied to the continuously operated FBLG with screen-mill-cycle.

Table 5.1.: Operating parameters and particles' shell porosity $\epsilon_{\mathrm{shell}}$ of the experiments presented in Rieck et al. [91]. The related particles are presented in Figure 5.1.

no.	$\theta_{\mathrm{f,in}}$	$\dot{m}_{\mathrm{inj}}$	η	$\epsilon_{\mathrm{shell}}$
1	50 °C	0.504 kg/h	0.79	0.50
2	50 °C	0.967 kg/h	0.56	0.64
3	95 °C	0.512 kg/h	0.89	0.46
4	95 °C	1.277 kg/h	0.72	0.50

5.2. Dynamic model

The coupling of particles and the surrounding fluidization medium is characteristic for FBLG. A manifold of states characterizes both particles and fluidization medium. While particles are described by the corresponding individual size, temperature, and moisture content, temperature and moisture content determine the state of the fluidization medium. Further important state variables are the dry hold-up mass of the particle bed and the fluidization medium. In the literature, several models that account for the thermal conditions in FBLG are available [13, 25, 28]. However, even if the models regard the impact of the particulate phase on the thermal states, they do not consider the influence of thermal conditions on the particle properties. Thus, the dynamic models presented so far are not capable of predicting any product property but particle size L.

This open issue is addressed in the remainder of this section. Based on Radichkov et al. [88] and Bück et al. [13], a dynamic model capable of accounting for the bidirectional coupling of the particle phase and fluidization medium is derived. The model consists, as presented in Figure 5.2, of two sub-systems: (i) A population balance model $n(t, L)$ accounting for the particle growth and (ii) a system of ordinary differential equations representing the thermal conditions. For modeling, it is assumed that both, particles and fluidization medium, are ideally mixed such that the formation of functional zones can be neglected. Hence, the temperature of particles $\theta_{\mathrm{p}}(t)$ and fluid $\theta_{\mathrm{f}}(t)$, moisture content of particles $X(t)$ and fluid $Y(t)$, and dry mass of the particle $m_{\mathrm{p,dry}}(t)$ and fluid hold-up $m_{\mathrm{f,dry}}(t)$ can be modeled as lumped states. By correlating the particles' shell porosity $\epsilon_{\mathrm{shell}}$ to the drying potential η [91] and introducing a porosity-dependent breakage of the particles during the milling of the oversized fraction, the thermal conditions and particle properties are linked. The upcoming sections present the modeling in details.

5.2.1. Population balance model

Starting with Equation (2.2), the population balance model is derived. Since the focus is on the process characteristics of continuous fluidized bed layering granulation with screen-mill-cycle, only layering growth, particle withdrawal, particle screening, and particle milling are considered. As pointed out above, this assumption is admissible since a proper choice of operating conditions suppresses further granulation and nucleation mechanisms [31]. Hence, particle breakage and attrition within the granulation chamber as well as thermal overspray can be neglected. Therefore, the PBM is given by

$$\frac{\partial n\left(t,L\right)}{\partial t} = -G\frac{\partial n}{\partial L} + \dot{n}_{\text{in}} - \dot{n}_{\text{out}} \ . \tag{5.1}$$

The particle growth depends on the porosity of the particles' shell ϵ_{shell}. Postulating an equal distribution of the injected suspension on the particle surface, again, a population of spherical particles is assumed,

$$G\left(n,\dot{m}_{\text{inj}},\epsilon_{\text{shell}}\right) = \frac{2x_{\text{inj}}\dot{m}_{\text{inj}}}{\left(1-\epsilon_{\text{shell}}\right)\rho_{\text{s}}A_{\text{bed}}} \tag{5.2}$$

determines the growth rate [65]. The growth rate depends on the injection rate $\dot{m}_{\text{inj}}$, the corresponding mass fraction x_{inj}, mass density of the solid ρ_{s}, and the total surface of the particle bed $A_{\text{bed}}\left(t\right) = \pi\mu_2\left(n\right)$ with $\mu_i\left(n\right) = \int_0^\infty L^i n\left(t,L\right)\mathrm{d}L$. For the layering granulation of sodium benzoate, as shown by experiments [23, 49, 91], the shell porosity ϵ_{shell} correlates linearly to the drying potential η:

$$\epsilon_{\text{shell}} = -\Delta\epsilon_{\text{shell}}\eta + \epsilon_{\text{shell},0} \ . \tag{5.3}$$

The corresponding parameters $\Delta\epsilon_{\text{shell}}$ and $\epsilon_{\text{shell},0}$ are presented in the experimental study of Rieck et al. [91]. Due to variating operating conditions over process time, the overall porosity of a particle may change. To take this into account, the apparent average porosity of the particles, defined by

$$\epsilon_{\text{p}} = 1 - \frac{m_{\text{p,dry}}/\rho_{\text{s}}}{\left(\pi/6\right)\mu_3\left(n\left(t,L\right)\right)} \ , \tag{5.4}$$

is introduced.

The potential η represents the drying of the particles. It is defined as the ratio between the actual drying rate and the maximum drying rate, i.e., under saturated conditions, with respect to the state of the fluidization medium at the inlet. Hence, the drying potential η measures the efficiency of the drying process. It is determined by the moisture content of the fluidization medium at the inlet Y_{in} and at the outlet Y_{out} as well as the saturation moisture Y_{sat}. As it is assumed that the fluidization medium is ideally mixed, the condition $Y_{\text{out}} = Y$ applies. Consequently,

$$\eta = {\left(Y_{\text{sat}}-Y\right)}/{\left(Y_{\text{sat}}-Y_{\text{in}}\right)} \ . \tag{5.5}$$

defines the drying potential.

Throughout process time, particles are removed from the granulation chamber by a non-classifying withdrawal: $\dot{n}_{\text{out}}(t, L) = Kn$. To keep the bed mass constant over time, as a proper continuous operation demands, a PI controller manipulates the drain gain K. Therefore, the deviation of the actual dry bed mass $m_{\text{p,dry}}$ and the related reference values $m_{\text{p,dry,ref}}$ determines the corresponding control error. The withdrawn particles are, in accordance with Equations (3.16) – (3.19), classified into fines $\dot{n}_{\text{fines}}$, product $\dot{n}_{\text{product}}$, and oversized fraction $\dot{n}_{\text{over}}$. While the product fraction is removed from the process, oversized particles are milled. Following Equations (3.20) and (3.21), the mill imprints a Gaussian size distribution - defined by mean diameter L_{mill} and variance σ_{mill}^2 - onto the oversized particles $\dot{n}_{\text{over}}$. Thereby, the corresponding masses are conserved. In contrast to Section 3.3, L_{mill} is not an arbitrary operating parameter. Instead, L_{mill} divides into two terms:

$$L_{\text{mill}} = L_{\text{mill},0} + \Delta L_{\text{mill}} . \tag{5.6}$$

While $L_{\text{mill},0}$ accounts for the operating conditions of the mill, ΔL_{mill} represents the influence of the particle properties on the breakage within the mill. Basically, Equation (5.6) splits the milling process into a material and machine function as proposed by Vogel et al. [114].

As shown in Diez et al. [23], the strength of a particle depends on its apparent porosity ϵ_{p}. To consider the resultant influence of ϵ_{p} on the milling, the linear correlation

$$\Delta L_{\text{mill}}(\epsilon_{\text{p}}) = a_{\text{break}} + b_{\text{break}}\epsilon_{\text{p}} \tag{5.7}$$

is introduced. After milling, the particles $\dot{n}_{\text{mill}}$ are, together with the fines $\dot{n}_{\text{fines}}$, re-fed to the granulation chamber serving as nuclei.

5.2.2. Heat & mass transfer

The dynamics of the thermal conditions within the FBLG are described by six dynamic states: temperature of particles $\theta_{\text{p}}(t)$ and fluid $\theta_{\text{f}}(t)$, moisture content of particles $X(t)$ and fluid $Y(t)$, the mass of the dry hold-up of particles $m_{\text{p,dry}}(t)$ and fluidization medium $m_{\text{f,dry}}(t)$. Based on mass and enthalpy balances, the corresponding state equations are derived assuming an ideally mixed system.

As the solvent is not represented by separate state equations, liquid solvent $m_{\text{p,solvent}}$ and vapor solvent $m_{\text{f,solvent}}$ are considered as a part of the particle and fluid phase, respectively. Based on that assumption, the moisture contents of the particle and fluid phase are defined as the ratios of solvent mass to dry mass. Hence, $X(t) = m_{\text{p,solvent}}/m_{\text{p,dry}}$ and $Y(t) = m_{\text{f,solvent}}/m_{\text{f,dry}}$ hold. The related temporal behaviour is represented by the corresponding time derivatives:

$$\dot{X}(t) = \left(\dot{m}_{\text{p,solvent}} - X\dot{m}_{\text{p,dry}}\right)/m_{\text{p,dry}} \quad \text{and} \quad \dot{Y}(t) = \left(\dot{m}_{\text{f,solvent}} - Y\dot{m}_{\text{f,dry}}\right)/m_{\text{f,dry}} . \tag{5.8}$$

The required time derivatives of the solvent and the dry mass related to particle and
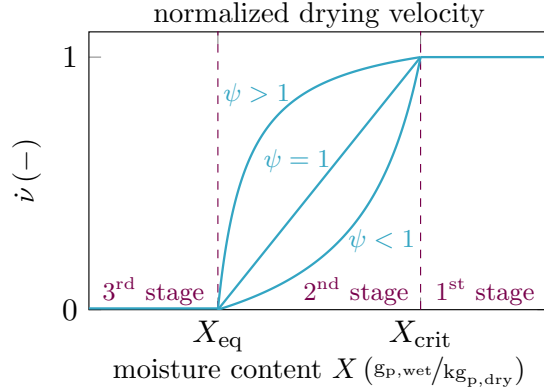
Figure 5.3.: Normalized drying velocity $\dot{\nu}$ over moisture content of the particles X as introduced by van Meel [111] for different drying characteristics represented by ψ.

fluid phase result from balancing the mass flows:

$$\dot{m}_{\mathrm{p,dry}}\left(t\right) = x_{\mathrm{inj}}\dot{m}_{\mathrm{inj}} + \dot{m}_{\mathrm{p,dry,in}} - \dot{m}_{\mathrm{p,dry,out}} \tag{5.9}$$

$$\dot{m}_{\mathrm{p,solvent}}\left(t\right) = \left(1 - x_{\mathrm{inj}}\right)\dot{m}_{\mathrm{inj}} + X_{\mathrm{in}}\dot{m}_{\mathrm{p,dry,in}} - X_{\mathrm{out}}\dot{m}_{\mathrm{p,dry,out}} - \dot{m}_{\mathrm{evap}}, \tag{5.10}$$

$$\dot{m}_{\mathrm{f,dry}}\left(t\right) = \dot{m}_{\mathrm{f,dry,in}} - \dot{m}_{\mathrm{f,dry,out}}\ , \tag{5.11}$$

$$\dot{m}_{\mathrm{f,solvent}}\left(t\right) = Y_{\mathrm{in}}\dot{m}_{\mathrm{f,dry,in}} - Y\dot{m}_{\mathrm{f,dry,out}} + \dot{m}_{\mathrm{evap}}\ . \tag{5.12}$$

While x_{inj}, $\dot{m}_{\mathrm{inj}}$, the mass flows of the fluidization medium at inlet $\dot{m}_{\mathrm{f,dry,in}}$ and the corresponding moisture content Y_{in} as well as mass flows of the fluidization medium at outlet $\dot{m}_{\mathrm{f,dry,out}}$ are operating parameters, the mass flows related to the particle flows of the feed $\dot{m}_{\mathrm{p,dry,in}}$ and the withdrawal $\dot{m}_{\mathrm{p,dry,out}}$ depend on the population balance model presented in the previous Section 5.2.1. They are determined by $\dot{m}_{\mathrm{p,dry},i} = \left(1 - \epsilon_{\mathrm{p},i}\right)\rho_{\mathrm{s}}\left(\pi/6\right)\mu_{3}\left(\dot{n}_{i}\right)$ for $i = \{\mathrm{fines, milled, out}\}$. The remaining mass flow rate $\dot{m}_{\mathrm{evap}}$ represents the drying of the particles. It denotes the mass transfer of the injected solvent from the particle phase to the fluidization medium due to its evaporation.

In brief, the term drying denotes the heat and mass transfer between a solid and a fluid, here particles and fluidization medium, due to the evaporation of a liquid. However, even if the nature of the process is quite intuitive, the drying of porous media, like sodium benzoate particles on the microscopic scale, is one of the most complex problems in the field of process engineering [118]. For instance, the heat and mass transfer - and thereby the evaporation rate $\dot{m}_{\mathrm{evap}}$ - depends not only on the state of the surrounding fluid but also on the particle characteristics as size, moisture, and material properties [18]. On the macroscopic scale, as proposed by van Meel [111] and illustrated in Figure 5.3, the drying process divides into three periods: In the first period, characterized by $X \geq X_{\mathrm{crit}}$, where X_{crit} denotes the critical moisture of the particles, the evaporation rate $\dot{m}_{\mathrm{evap}}$, is limited by the state of the fluidization medium only. This is because mainly moisture located at the particles' surface evaporates in this period. In the second period, $X_{\mathrm{crit}} \leq X \leq X_{\mathrm{eq}}$, mass transfer resistances on the particle-side decrease $\dot{m}_{\mathrm{evap}}$. In the

third drying period, the particle moisture X is, however, below the thermodynamic adsorption equilibrium moisture X_{eq} such that $X < X_{eq}$ holds. In this period, no further drying takes place.

To address the decrease of the evaporation rate $\dot{m}_{evap}$ over the drying periods, van Meel [111] introduced the normalized drying velocity $\dot{\nu} = \dot{m}_{evap}/\dot{m}_{evap,I}$. It is defined as the ratio of the actual evaporation rate $\dot{m}_{evap}$ to the evaporation rate corresponding to the first period $\dot{m}_{evap,I}$. As only the state of the fluid limits the evaporation in the first period, $\dot{m}_{evap,I}$ is the maximal possible value of $\dot{m}_{evap}$. Hence, $\dot{\nu}$ is unity in the first while it becomes zero in the third period. In between, $\dot{\nu}$ depends on the actual particle moisture X and specific material properties. To address the influence of material properties on the drying in the second period, the parameter ψ is introduced. In conclusion, the normalized drying velocity is given by

$$\dot{\nu}\left(\delta\right) = \begin{cases} 1 & X \geq X_{crit} \\ \frac{\psi\delta(X)}{1+(\psi-1)\delta(X)} & X_{crit} > X \geq X_{eq} \\ 0 & X_{eq} > X \end{cases} \tag{5.13}$$

where $\delta\left(X\right) = {(X-X_{eq})}/{(X_{crit}-X_{eq})}$ represents the normalized moisture content. Hence, the drying curve, representing the drying characteristics and presented in Figure 5.3, is determined by the parameters ψ, X_{eq}, and X_{crit}. Based on given experimental data, the drying curve can be fitted.

The driving force of the evaporation is the difference between the saturation moisture Y_{sat} and the moisture content Y_{in} [84]. The saturation moisture Y_{sat} - defined as the maximum amount of vapor a fluid can carry - depends on the state of the fluidization medium at the inlet, in specific on $\theta_{f,in}$ and Y_{in} [13, p. 165]. As a whole, the evaporation rate is given by

$$\dot{m}_{evap} = \dot{\nu}\left(\delta\right)\beta_{fp}A_{bed}\left(Y_{sat}\left(Y_{in},\theta_{f,in}\right) - Y\right)\rho_{f,dry} \tag{5.14}$$

Besides Y, Y_{sat}, and $\dot{\nu}$, the evaporation rate depends on the overall surface of the particles $A_{bed} = \pi\mu_2\left(n\left(t,L\right)\right)$, the mass density of the dry fluid $\rho_{f,dry}$, and the coefficient β_{fp} representing the mass transport between fluid and particles as presented by Gnielinski [41].

Starting with the total enthalpies of particles $H_p = m_{p,dry}\left(c_{p,p} + c_{p,l}X\right)\theta_p$ and fluidization medium $H_f = m_{f,dry}\left(\left(c_{p,f} + c_{p,v}Y\right)\theta_f + Y\Delta h_{evap}\right)$, the state equations of particle and fluid temperature $\theta_p\left(t\right)$ and $\theta_f\left(t\right)$ are derived. The enthalpies depend on the specific heat capacities of the particles $c_{p,p}$, liquid water $c_{p,l}$, water vapor $c_{p,v}$, dry air $c_{p,f}$, and on the specific evaporation enthalpy of water Δh_{evap} at $\theta = 0\ °C$. The material characteristics related to dry air, water vapor, and liquid water are determined by the correlations presented by Glück [40]. In contrast, as the heat capacity of sodium benzoate depends hardly on the temperature under the investigated conditions [53], $c_{p,p}$ is a fixed parameter.

The enthalpies are derived with respect to time and, afterwards, reformulated such that

$$\dot{\theta}_p\left(t\right) = \frac{\dot{H}_p - \left(c_{p,p} + c_{p,l}X\right)\theta_p\dot{m}_{p,dry} - m_{p,dry}c_{p,l}\theta_p\dot{X}}{m_{p,dry}\left(c_{p,p} + c_{p,l}X\right)} \tag{5.15}$$

Table 5.2.: Default simulation parameter set $\Pi_{\text{pro},0}$.

Parameter set $\Pi_{\text{pro},0}$

Particle phase			Particle outlet & screening		
$m_{\text{p,dry}}$	15.0	kg	$k_{\text{p,out}}$	-0.001	$1/s$
$c_{\text{p,p}}$	4200	J/kg·K	$\tau_{\text{i,out}}$	1000	s
Fluidization medium			L_{I}	1.00	mm
$m_{\text{f,dry}}$	1.0	kg	σ_{I}	0.065	mm
$\dot{m}_{\text{f,dry,in}}$	1500.0	kg/h	L_{II}	1.40	mm
Y_{in}	6.0	g$_{\text{f,wet}}$/kg$_{\text{f,dry}}$	σ_{II}	0.055	mm
$\theta_{\text{f,in}}$	80.0	°C	Particle milling		
Heater Dynamics			a_{break}	2.50	mm
τ_{heater}	10.0	s	b_{break}	0.98	mm
Injected suspension			$L_{\text{mill},0}$	0.8	mm
$\dot{m}_{\text{inj}}$	40.0	kg/h	σ_{mill}	0.1	mm
x_{inj}	0.35		PI controllers		
θ_{inj}	20	°C	k_{η}	10.0	°C
Drying characteristics			τ_{η}	100.0	s
ψ	0.1		$k_{d_{32,\text{bed}}}$	0.01	
X_{eq}	5.0	g$_{\text{p,wet}}$/kg$_{\text{p,dry}}$	$\tau_{d_{32,\text{bed}}}$	100.0	s
X_{crit}	50.0	g$_{\text{p,wet}}$/kg$_{\text{p,dry}}$			
$\epsilon_{\text{shell},0}$	0.45				
$\Delta\epsilon_{\text{shell}}$	-0.33				

and

$$\dot{\theta}_{\text{f}}(t) = \frac{\dot{H}_{\text{f}} - \left((c_{\text{p,f}} + c_{\text{p,v}}Y)\theta_{\text{f}} + Y\Delta h_{\text{evap}}\right)\dot{m}_{\text{f,dry}} - m_{\text{f,dry}}\left(c_{\text{p,v}}\theta_{\text{f}} + \Delta h_{\text{evap}}\right)\dot{Y}}{m_{\text{f,dry}}\left(c_{\text{p,f}} + c_{\text{p,v}}Y\right)} \quad (5.16)$$

hold. Strictly speaking, the Equations (5.15) and (5.16) also depend on the temperature derivatives of the specific heat capacities $c_{\text{p},i}$. However, as under the investigated conditions the numerical values of $\partial c_{\text{p},i}/\partial\theta$ are quite small, their influence is neglected in the remainder of this chapter.

By balancing the enthalpy flows, the time derivatives of particle enthalpy $\dot{H}_{\text{p}}$ and fluid enthalpy $\dot{H}_{\text{f}}$ are determined:

$$\dot{H}_{\text{p}}(t) = \dot{H}_{\text{inj}} + \dot{H}_{\text{p,in}} - \dot{H}_{\text{p,out}} + \dot{Q}_{\text{fp}} - \dot{H}_{\text{evap}} , \quad (5.17)$$

$$\dot{H}_{\text{f}}(t) = \dot{H}_{\text{f,in}} - \dot{H}_{\text{f,out}} - \dot{Q}_{\text{fp}} + \dot{H}_{\text{evap}} . \quad (5.18)$$

The particle phase and fluidization medium are coupled via (i) the heat-transfer

$$\dot{Q}_{\text{fp}}(t) = \alpha_{\text{fp}}A_{\text{bed}}\left(\theta_{\text{p}} - \theta_{\text{f}}\right) \quad (5.19)$$

and (ii) the enthalpy transfer caused by the evaporation

$$\dot{H}_{\text{evap}}(t) = \dot{m}_{\text{inj}}\left(c_{\text{p,v}}\theta_{\text{f}} + \Delta h_{\text{evap}}\right) . \quad (5.20)$$

While the first depends on the heat-mass-transfer coefficient α_{fp}, as presented in Gnielinski [41], the second correlates to the evaporation rate $\dot{m}_{\mathrm{evap}}$, defined by Equation (5.14). The remaining enthalpy flows $\dot{H}_i$ result from the mass transfer of the injection

$$\dot{H}_{\mathrm{inj}}\left(t\right) = \dot{m}_{\mathrm{inj}}\left(x_{\mathrm{inj}}c_{\mathrm{p,p}} + \left(1 - x_{\mathrm{inj}}\right)c_{\mathrm{p,l}}\right)\theta_{\mathrm{inj}}\ , \tag{5.21}$$

the enthalpy transfer induced by the fluidization

$$\dot{H}_{\mathrm{f,in}} = \dot{m}_{\mathrm{f,dry,in}}\left(\left(c_{\mathrm{p,f}} + c_{\mathrm{p,v}}Y_{\mathrm{in}}\right)\theta_{\mathrm{f,in}} + Y_{\mathrm{in}}\Delta h_{\mathrm{evap}}\right)\ , \tag{5.22}$$

$$\dot{H}_{\mathrm{f,out}} = \dot{m}_{\mathrm{f,dry,out}}\left(\left(c_{\mathrm{p,f}} + c_{\mathrm{p,v}}Y\right)\theta_{\mathrm{f}} + Y\Delta h_{\mathrm{evap}}\right)\ , \tag{5.23}$$

and the mass flows related to the particles recycle and withdrawal

$$\dot{H}_{\mathrm{p,in}}\left(t\right) = \dot{m}_{\mathrm{p,dry,in}}\left(c_{\mathrm{p,p}} + c_{\mathrm{p,l}}\ X_{\mathrm{in}}\right)\theta_{\mathrm{p,in}}\ ,\ \text{and} \tag{5.24}$$

$$\dot{H}_{\mathrm{p,out}}\left(t\right) = \dot{m}_{\mathrm{p,dry,out}}\left(c_{\mathrm{p,p}} + c_{\mathrm{p,l}}X_{\mathrm{out}}\right)\theta_{\mathrm{p,out}}\ . \tag{5.25}$$

As an ideal mixing of the particle phase in the FBLG is assumed, the conditions $\theta_{\mathrm{p,out}} = \theta_{\mathrm{p}}$ and $X_{\mathrm{out}} = X$ hold. Due to the short residence time of particles in the recycle, further cooling and drying within periphery neglected. Hence, the assumptions $\theta_{\mathrm{p,in}} = \theta_{\mathrm{p,out}}$ and $X_{\mathrm{in}} = X_{\mathrm{out}}$ apply.

For considering the transient behavior of the fluid heater, the temperature $\theta_{\mathrm{f,in}}$, required to determine $\dot{H}_{\mathrm{f,in}}$ with Equation (5.22), is modeled by a first-order lag element with the corresponding time constant τ_{heater}.

The derived dynamic model requires a manifold of system parameters. They can be sub-divided into the following categories:

(1) caloric parameters (e.g., evaporation enthalpy Δh_{evap} or heat capacities $c_{\mathrm{p},i}$),

(2) heat & mass transfer coefficients (α_{fp} and β_{fp}),

(3) parameters related to the drying curve (ψ, X_{eq}, and X_{crit}),

(4) parameters correlating operating parameters to particle properties ($\Delta\epsilon_{\mathrm{shell}}$ and $\epsilon_{\mathrm{shell,0}}$; a_{break} and b_{break}),

(5) and parameters representing the periphery (mill and screen).

The parameters can be taken from property data bases (1), can be approximated by well-established correlations (2), or can be fitted to experimental data (3,4). The periphery (5) is represented by idealized models.

5.3. Open-loop dynamics

The developed dynamic model of the fluidized bed layering granulation consists of two sub-systems: (i) a population balance model considering the particle sizes and (ii) a system of ordinary differential equations representing the thermal conditions. The corresponding system equations were derived in the foregone Sections 5.2.1 and 5.2.2. As presented in Figure 5.4, the two systems are coupled in both directions. For instance, the overall-surface of the particle bed $A_{\mathrm{bed}}\left(n\left(t,L\right)\right)$ influences the heat-transfer $\dot{Q}_{\mathrm{fp}}$ and the evaporation of the solvent $\dot{m}_{\mathrm{evap}}$. As the corresponding state equations depend explicitly or implicitly on $\dot{Q}_{\mathrm{fp}}$ and $\dot{m}_{\mathrm{evap}}$, the particle population $n\left(t,L\right)$ affects the thermal conditions $X\left(t\right)$, $Y\left(t\right)$, $\theta_{\mathrm{p}}\left(t\right)$, and $\theta_{\mathrm{f}}\left(t\right)$. On the contrary, the breakage of the particles correlates via ϵ_{p} and η to the thermal states. Hence, the thermal conditions influence, besides particles properties, the particle size distribution $n\left(t,L\right)$.

In the present section, the influence of the bidirectional coupling on product properties, dynamics, and process stability is illustrated by means of simulations and stability analyses. Inspired by the experimental findings presented in Chapter 4 and the contributions [23, 50, 91, 92, 94], the simulation scenarios *Pro 1 – Pro 4* presented in Table 5.3 are introduced. The initial point of all simulations is a stable steady-state related to the default parameter set given in Table 5.2. The focus of the simulation study is clearly on the process dynamics and particle porosities. However, further product properties, for instance, temperature and moisture content of the particles, depend also on the operating conditions. Besides, stability-maps were determined to illustrate the impact of the selected operating parameters on the local process stability.

***Pro 1* - particle milling** As indicated by theoretical investigations and proven by experiments, see Section 3.3 and Chapter 4, the milling has a significant influence on process stability. Coarse milling favors a steady-state regime, while fine milling results in the occurrence of self-sustained oscillations of the particle size distribution $n\left(t,L\right)$.

Table 5.3.: Overview of the simulation scenarios. Initial state of all simulations is the steady-state corresponding to the default parameter set $\Pi_{\mathrm{pro,0}}$ presented in Table 5.2.

Open-loop simulations

scenario	manipulated parameter		$t = 0$ h	$t_1 = 2$ h	$t_2 = 10$ h	Figures
Pro 1	$L_{\mathrm{mill,0}}$	[mm]	0.80	0.90	0.70	5.5 & 5.6
Pro 2	$\theta_{\mathrm{f,in}}$	[°C]	80.0	90.0	70.0	5.5 & 5.8
Pro 3	$\dot{m}_{\mathrm{inj}}$	[kg/h]	40.0	32.0	48.0	5.5 & 5.9
Pro 4	Y_{in}	[$\mathrm{g_{f,wet}}/\mathrm{kg_{f,dry}}$]	6.0	0.0	15.0	5.5 & 5.10

Closed-loop simulations

scenario	$t_{\mathrm{sp}} = 2$ h	$t_{\mathrm{dist}} = 15$ h	Figures
Pro 5	$\epsilon_{\mathrm{p,ref}} = 0.425$	$Y_{\mathrm{in}} = 15.0\ \mathrm{g_{f,wet}}/\mathrm{kg_{f,dry}}$	5.14, 5.15 & 5.20
Pro 6	$\epsilon_{\mathrm{p,ref}} = 0.370$	$\dot{m}_{\mathrm{inj}} = 32.0\ \mathrm{kg/h}$	5.21
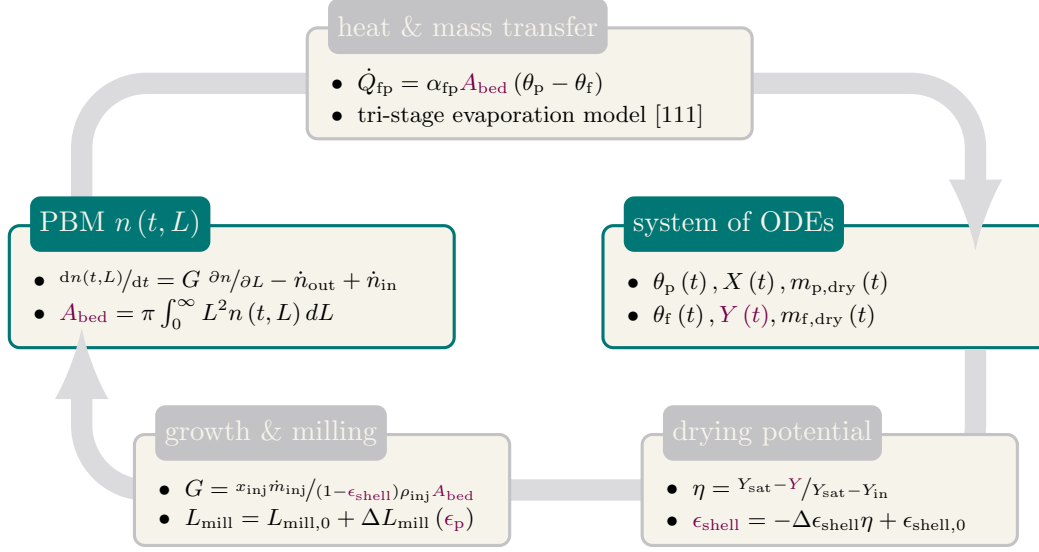
Figure 5.4.: Bidirectional coupling of particulate phase and thermal conditions represented by population balance model (PBM) and a system of ordinary differential equations (ODEs), respectively.

Those oscillations are undesired and have to be avoided as they induce variations of the mass flows $\dot{m}_i(t)$ and may, in the worst case, lead to a process breakdown,

Referring to the corresponding simulation results presented in Figure 5.5 and 5.6, the dynamic model is capable of reproducing the experimental observations qualitatively. While the increase of the nominal mean diameter of milled particles $L_{\mathrm{mill},0}$ from 0.8 mm to 0.9 mm at $t_1 = 2$ h, representing coarse milling, results in the formation of a new stationary profile of the particle size distribution $n(t, L)$, oscillatory behavior characterizes $n(t, L)$ for fine milling, viz. after the reduction of $L_{\mathrm{mill},0}$ to 0.7 mm at $t_2 = 10$ h. The stability maps presented in Figure 5.7 confirm this observation: The process tends to instabilities for small $L_{\mathrm{mill},0}$.

The variations of the particle size distribution lead to a varying Sauter mean diameter $d_{32,\mathrm{bed}} = 6V_{\mathrm{bed}}/A_{\mathrm{bed}} = \mu_3(n)/\mu_2(n)$. As, by adjusting the controlled drain gain K, a constant bed mass $m_{\mathrm{p,dry}}$ is ensured over process time, the overall volume of the particle bed V_{bed}, neglecting the small changes of the apparent particle porosity ϵ_{p}, is considered as constant. In consequence, variations of $d_{32,\mathrm{bed}}$ are motivated by changes in the total bed surface A_{bed}. As the evaporation rate $\dot{m}_{\mathrm{evap}}$ and the heat transfer $\dot{Q}_{\mathrm{fp}}$ depend on the total surface of the particle bed, a shift of A_{bed} leads to a change of the thermal states $X, Y, \theta_{\mathrm{p}}$, and θ_{f}. However, the observed variations of the thermal stated induced by a change of the milling process are quite small. In consequence, the changes in shell porosity $\epsilon_{\mathrm{shell}}$ and apparent particle porosity ϵ_{p} - both correlate via the drying potential η to the moisture content of the fluid Y - are very small as well. Hence, the milling has no significant impact on the particles' structure. This observation is in good agreement with the experimental results of Schmidt [92].
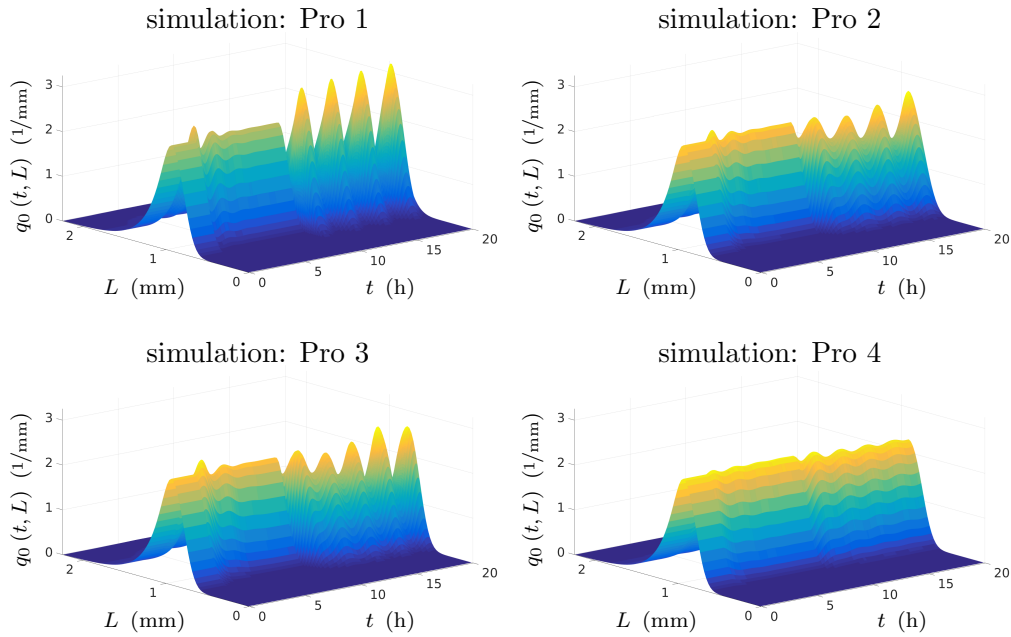
Figure 5.5.: Normalized particle size distributions $q_0\,(t, L)$ related to the simulations of scenarios *Pro 1 – Pro 4*. The corresponding process states are presented in Figures 5.6 and 5.8 – 5.10.
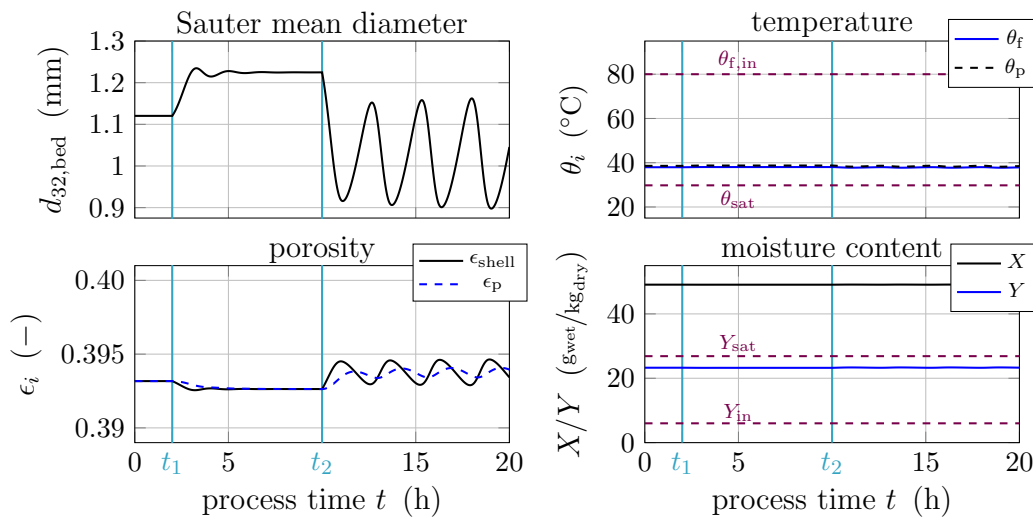
Figure 5.6.: Simulation results according to scenario *Pro 1*: Setpoint switch of mean diameter of milled particles $L_{\mathrm{mill,0}}$ from 0.80 mm to 0.90 mm at $t_1 = 2$ h and to 0.70 mm at $t_2 = 10$ h. The related particle size distribution $n\,(t, L)$ is presented in Figure 5.5.
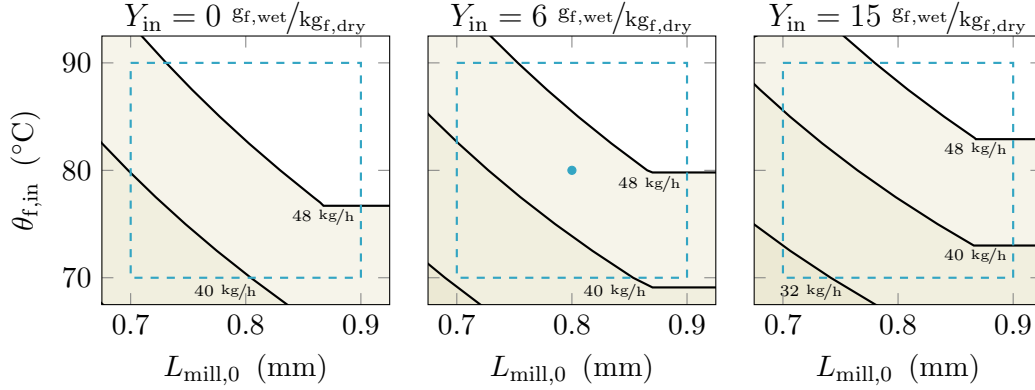
Figure 5.7.: Stability maps in the $(L_{\text{mill},0}, \theta_{\text{f,in}})$-domain with respect to the moisture content of the fluidization medium at inlet (from left to right: $Y_{\text{in}} = [0, 6, 15]$ $\text{g}_{\text{f,wet}}/\text{kg}_{\text{f,dry}}$) and the injection rate. Corresponding to the injection rates $\dot{m}_{\text{inj}} = [32, 40, 48]$ kg/h, shaded domains indicate unstable process regime. The predefined reference point and workspace are indicated by the marker (●) and the dashed line (- - -), respectively.

Pro 2 - **temperature of fluidization medium**   By means of experiments, Schmidt et al. [92, 94] proved the influence of the temperature of the fluidization medium on particle properties and process stability: A lowering of the inlet temperature of the fluidization medium $\theta_{\text{f,in}}$ resulted in an increased particle porosity ϵ_{p} as well as in the occurrence of self-sustained oscillations of the particle size distribution $n(t, L)$. In the respective simulation scenario, the temperature $\theta_{\text{f,in}}$ is increased from 80 °C to 90 °C at $t_1 = 2$ h and, after some settling time, reduced to 70 °C at $t_2 = 10$ h.

As presented in Figure 5.8, the manipulation of the fluid temperature shifts the saturation point. The increase of $\theta_{\text{f,in}}$ at t_1 raised the saturation temperature θ_{sat} and the saturation moisture Y_{sat}. This leads, in accordance with equations (5.3) and (5.5), to an increase of the drying potential η and, in consequence, to a decrease the porosity of the shell ϵ_{shell} and the apparent particle porosity ϵ_{p}. Following equations (5.6) and (5.7), a smaller porosity ϵ_{p} shifts the mean diameter of milled particles L_{mill} to larger values inducing a change of the particle size distribution $n(t, L)$ leading to an increased Sauter mean diameter $d_{32,\text{bed}}$. However, as illustrated in Figures 5.5 and 5.8, the process settles to a new steady-state after a sufficient settling time. On the contrary, self-sustained oscillations arose after the parameter adjustment at t_2. In line with the presented argumentation, the lowering of $\theta_{\text{f,in}}$ to 70 °C decreases L_{mill} such that the process became unstable.

The studied stability boundary can be found in the stability maps presented in Figure 5.7: For sufficient high temperatures, the local process stability depends on $\theta_{\text{f,in}}$ and $L_{\text{mill},0}$. Here, a crossing of the stability boundary results in the occurrence of self-sustained oscillations. For smaller temperatures, a second type of stability boundary, determined by $\theta_{\text{f,in}}$ only, occurs. A crossing of this boundary results in a too-small saturation moisture Y_{sat} such that too little moisture is carried out of the granulation
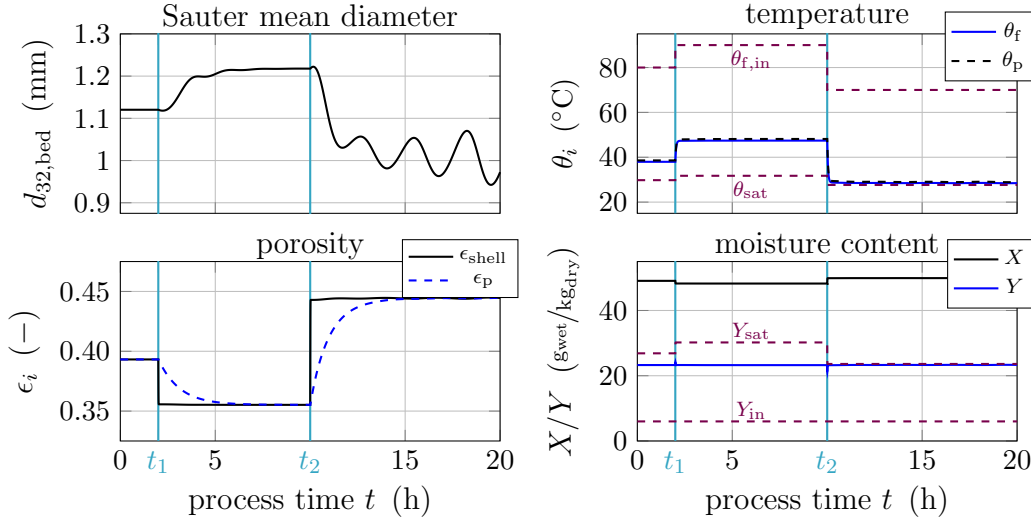
Figure 5.8.: Simulation results according to scenario *Pro 2*: Setpoint switch of the temperature of the fluidization medium at inlet $\theta_{\mathrm{f,in}}$ from 80.0 °C to 90.0 °C at $t_1 = 2$ h and to 70.0 °C at $t_2 = 10$ h. The related particle size distribution $n(t, L)$ is presented in Figure 5.5.
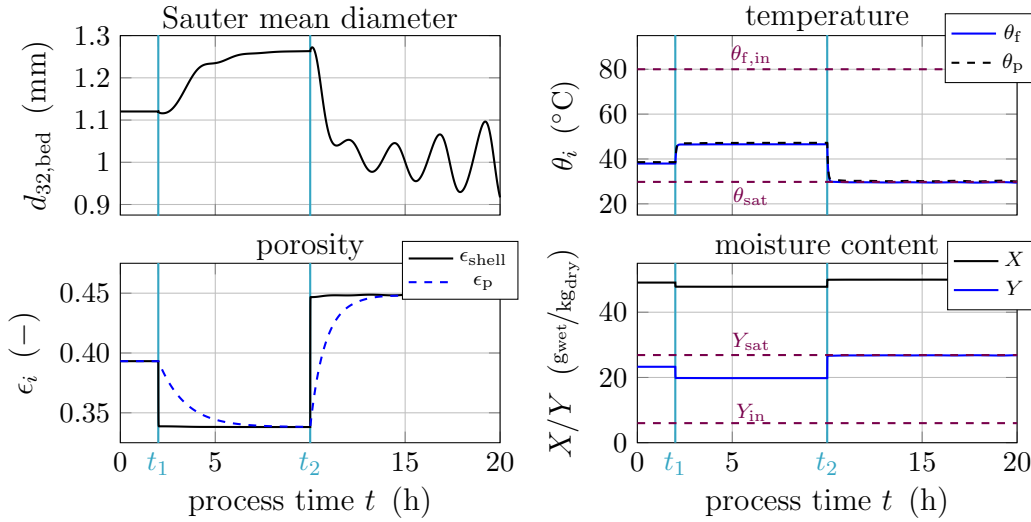

Figure 5.9.: Simulation results according to scenario *Pro 3*: Setpoint switch of injection rate $\dot{m}_{\mathrm{inj}}$ from 40.0 kg/h to 32.0 kg/h at $t_1 = 2$ h and to 48.0 kg/h at $t_2 = 10$ h. The related particle size distribution $n(t, L)$ is presented in Figure 5.5.
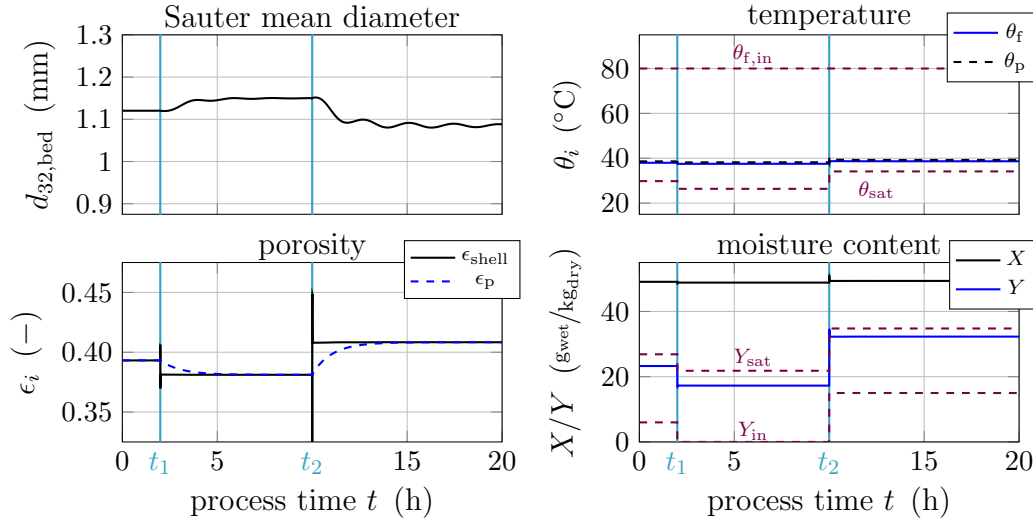
Figure 5.10.: Simulation results according to scenario *Pro 4*: Setpoint switch of the moisture content of the fluidization medium at inlet Y_{in} from 6.0 $g_{f,wet}/kg_{f,dry}$ to 0.0 $g_{f,wet}/kg_{f,dry}$ at $t_1 = 2$ h and to 15.0 $g_{f,wet}/kg_{f,dry}$ at $t_2 = 10$ h. The related particle size distribution $n(t, L)$ is presented in Figure 5.5.

chamber by the fluidization medium. The resultant accumulation and condensation of the solvent within the process leads to the process breakdown.

Pro 3 - injection rate   The injection rate affects product properties and process stability. As shown by experiments [92, 94], high-valued $\dot{m}_{inj}$ lead to a high particle porosity and the occurrence of self-sustained oscillations. These patterns were also observed in the simulation of scenario *Pro 3* as well as in the stability analysis. The corresponding results are presented in Figures 5.5, 5.7, and 5.9.

In the simulation, the decrease of $\dot{m}_{inj}$ from 40 kg/h to 32 kg/h at $t_1 = 2$ h leads to a descent of Y and thus, via the drying potential η, to smaller porosities ϵ_{shell} and ϵ_p. Since a lower apparent particle porosity raises the mean diameter of milled particles L_{mill}, the process stays stable and settles at the corresponding steady-state. Then again, the rise of $\dot{m}_{inj}$ to 48 kg/h at $t_2 = 10$ h increases the particle porosities through the decreased drying potential. Due to the shrinking L_{mill}, the process becomes unstable such that self-sustained oscillations arise.

Pro 4 - moisture content of the fluid   The last open-loop simulation scenario *Pro 4* illustrates the influence of the moisture content of the fluidization medium at inlet Y_{in} on product properties and process stability. The moisture content Y_{in} affects the saturation moisture Y_{sat} and the drying potential η. Summarizing the related simulation results presented in Figures 5.5 and 5.10, larger Y_{in} result in higher porosities ϵ_{shell} and ϵ_p. However, even if a change of stability was not observed in the simulation, process
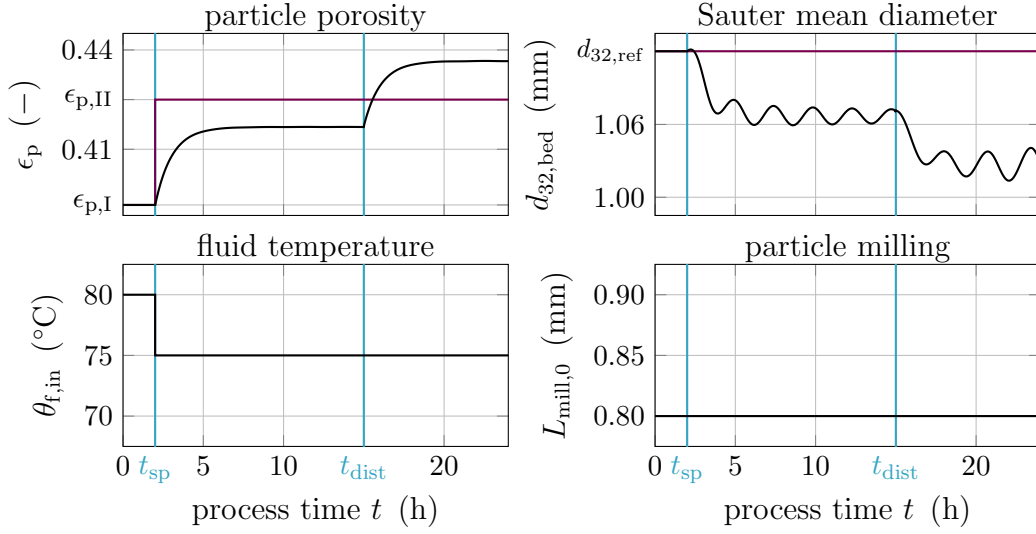
Figure 5.11.: Simulation results of the open loop system according to scenario *Pro 5*: To adjust apparent particle porosity ϵ_p, the temperature $\theta_\mathrm{f,in}$ is reduced from 80.0 °C to 75.0 °C at $t_\mathrm{sp} = 2$ h. At $t_\mathrm{dist} = 15$ h the moisture content Y_in is increased from 6 $\mathrm{g_{f,wet}}/\mathrm{kg_{f,dry}}$ to 15 $\mathrm{g_{f,wet}}/\mathrm{kg_{f,dry}}$.

stability depends on the moisture content of the fluid. Referring to the stability maps given in Figure 5.7, an increase of Y_in shifts the stability boundary to higher values of $\theta_\mathrm{f,in}$ and $L_\mathrm{mill,0}$.

Recapitulating the presented results,

(i) the influence of the particle phase on the fluidization medium is quite weak,

(ii) the impact of the thermal conditions on product properties, in particular on the shell porosity ϵ_shell and apparent particle porosity ϵ_p, is significant,

(iii) and the process stability depends on thermal conditions as well as on the milling parameter $L_\mathrm{mill,0}$.

These outcomes are in qualitative agreement with the experimental findings presented in Chapter 4 and the contributions of Schmidt et al. [92, 94]. Hence, the derived dynamic model is a reliable foundation for further theoretical investigations, e.g., for process and product design, and to design and test new control concepts.

5.4. Conventional process control

Industrial applications demand the formation of particles with tailored properties under steady-state conditions. As process stability and product properties depend both on the operating parameter, see previous Section 5.3, proper operation of the fluidized bed layering granulation is not trivial. For illustration, the simulation scenario *Pro 5* is defined: Starting at the steady-state corresponding to the default parameter set $\Pi_{\mathrm{pro},0}$, presented in Table 5.2, the desired apparent particle porosity $\epsilon_{\mathrm{p,ref}}$ is set from $\epsilon_{\mathrm{p,I}} = 0.39$ to $\epsilon_{\mathrm{p,II}} = 0.425$ at $t_{\mathrm{sp}} = 2$ h. In addition, the moisture content of the fluidization medium at the inlet Y_{in} is shifted from 6 $^{\mathrm{g_{f,wet}}}/_{\mathrm{kg_{f,dry}}}$ to 15 $^{\mathrm{g_{f,wet}}}/_{\mathrm{kg_{f,dry}}}$ at $t_{\mathrm{dist}} = 15$ h. While the first parameter switch represents a change of the required product property, the second represents a process disturbance.

As shown by the open-loop simulation presented in Figure 5.11, the particle porosity depends, inter alia, on the temperature of the fluid. The decrease of the temperature $\theta_{\mathrm{f,in}}$ at t_{sp} leads to an increased particle porosity ϵ_{p} and, due to the change of the particle breakage in accordance with Equation (5.6) and (5.7), to a lowering of the mean diameter of milled particles L_{mill} leading to a change of the particle size distribution $n(t, L)$. As monitored by the Sauter mean diameter $d_{32,\mathrm{bed}}$, the induced oscillations of the particle size are slightly decaying. The occurrence of the process disturbance at t_{dist} causes a further increase of the particle porosity ϵ_{p} and thus a further decrease in the size of the milled particles. On this occasion, self-sustained oscillations of $n(t, L)$ and $d_{32,\mathrm{bed}}$ arise. Hence the process becomes unstable such that the proper operation of the FBLG is not guaranteed anymore.

It is worth to mention that a precise tuning of the product properties requires extensive process knowledge. For instance, the formation of particles with the predefined porosity was not accomplished throughout the simulation. As will be shown in the upcoming sections, feedback control is a suitable tool to achieve both: the formation of particles with tailored properties and a stable steady-state operation.

5.4.1. Single input single output control

The objective of the first control strategy is a defined apparent particle porosity ϵ_{p}. In practice, precise measuring of particle porosity, for instance, based on scanning electron microscopy or micro-computed tomography, is complex and time-consuming [91, 92, 103]. Thus, an inline measuring of ϵ_{p} is hardly feasible. Instead, as ϵ_{p} correlates to η, the drying potential η is utilized as a surrogate. By reformulating Equation (5.3), the desired porosity $\epsilon_{\mathrm{p,ref}}$ determines the related reference value of the drying potential η_{ref}. Even though the drying potential can not be measured inline, it is determined, following Equation (5.5), by measurable thermal conditions. Since η depends on $\theta_{\mathrm{f,in}}$, the temperature of the fluidization medium at the inlet is used as actuating value. In the remainder, the temperature $\theta_{\mathrm{f,in}}$ is limited by the lower and upper constraints of 70 °C and 90 °C, respectively.
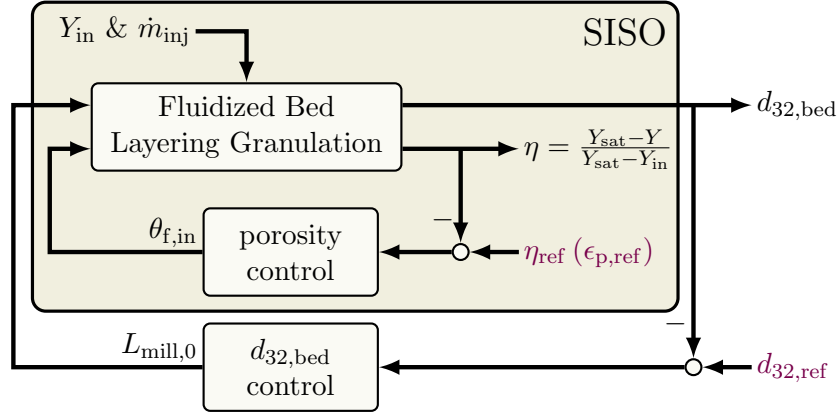
Figure 5.12.: Control structures corresponding to SISO (highlighted) and decentralized MIMO configuration (overall). The granulation process can be disturbed by variations of the moisture content Y_in and the injection rate $\dot{m}_\text{inj}$.

For the design of the single input single output (SISO) controller, the corresponding configuration is presented in Figure 5.12, the non-linear dynamic system was discretized and linearized in the vicinity of the steady-state related to the default parameter set. The resultant linear time-invariant LTI system of order 208 was reduced to the LTI system $G_{\theta_\text{f,in} \to \eta}(s)$ of order 11 by a balanced model truncation [100]. As shown in Figure 5.13, a PI controller $G_{\text{PI},i}(s) = {k_i(1+\tau_{\text{i},i}s)}/{\tau_{\text{i},i}s}$ with $i = \eta$ was parameterized through the root-locus method [33]. Table 5.2 presents the corresponding controller parameter k_η and $\tau_{\text{i},\eta}$. The designed controller was tested at the non-linear dynamic model by simulating scenario *Pro 5*.

Referring to the simulation results given in Figure 5.14, the designed controller is capable of tracking the reference step of the apparent particle porosity $\epsilon_\text{p,ref}$ at t_sp. By readjusting the temperature $\theta_\text{f,in}$, the controller drives the particles' porosity from the initial value $\epsilon_\text{p,I}$ to the new set-point $\epsilon_\text{p,II}$. In addition, the controller suppresses the process disturbances occurrence at t_dist by manipulating $\theta_\text{f,in}$ again. However, due to the change of the particle milling, instabilities arose: the particle size distribution $n(t,L)$, illustrated Figure 5.15, and thereby the Sauter mean diameter $d_\text{32,bed}$ are characterized by self-sustained oscillations. For stabilizing the process, a second control loop is introduced in the next section.

5.4.2. Decentralized multiple input multiple output control

The objective of the decentralized multiple input multiple output controller (MIMO) is a stable steady-state operation along with a defined particle porosity ϵ_p. For that purpose, the established SISO controller is extended by a second control loop. The overall structure is given in Figure 5.12. As shown by the experiments presented in Chapter 4, control of the milling is auspicious to stabilize the Sauter mean diameter and thereby the particle size distribution. Hence, $d_\text{32,bed}$ is used as a control variable, while $L_\text{mill,0}$ is the actuated value. The nominal mean diameter of milled particles $L_\text{mill,0}$
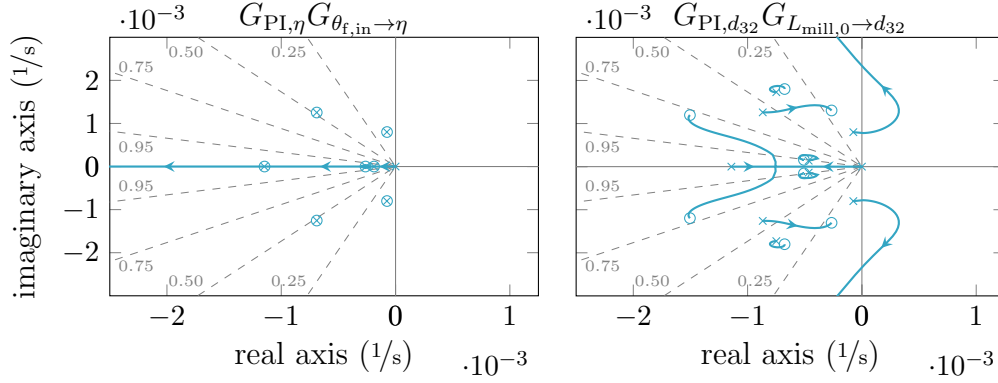
Figure 5.13.: Root-loci of the LTI systems $G_{\theta_{\mathrm{f,in}}\to\eta}(s)$ (**left**) and $G_{L_{\mathrm{mill},0}\to d_{32}}(s)$ (**right**) controlled by PI controller $G_{\mathrm{PI}}(s)$.

is limited by a lower constraint of 0.7 mm and an upper constraint of 0.9 mm.

Following the procedure presented in Section 5.4.1, the second controller is parametrized. Beginning with the linearization of the non-linear model - including the designed SISO controller $G_{\mathrm{PI},\eta}$ - the resultant LTI system of order 209 is reduced to the LTI system $G_{L_{\mathrm{mill},0}\to d_{32}}$ of order 11. Again, root-locus method was applied for the tuning of the controller $G_{\mathrm{PI},d_{32}}$. In the particular case, the root-loci divide into three domains: For small control gains $k_{d_{32}}$, all poles are located in the left half-plane such that the closed-loop process is stable. With an increasing $k_{d_{32}}$, a pair of complex poles moves to the right half-plane so as the controlled FBLG becomes unstable. A further increase of the control gain shifts the dominant pole pair back to the left half-plane leading to a stable process regime. As a small $k_{d_{32}}$ avoids sudden large-amplitude changes of the actuating value, for instance, induced by measuring noise, a control gain relating to the first domain was selected. The corresponding parameters $k_{d_{32}}$ and $\tau_{\mathrm{i},d_{32,\mathrm{bed}}}$ are presented in Table 5.2.

By applying the designed MIMO controller $K_{\mathrm{PI}}(s)=\mathrm{diag}\,(G_{\mathrm{PI},\eta},G_{\mathrm{PI},d_{32}})$, as presented in Figures 5.14 and 5.15, the formation of particles with a predefined porosity under stable steady-state conditions was achieved. However, as will be shown in the upcoming section, the performance and robustness of the MIMO controller can still be improved. For that purpose, centralized higher-order MIMO controllers are derived in the upcoming sections.
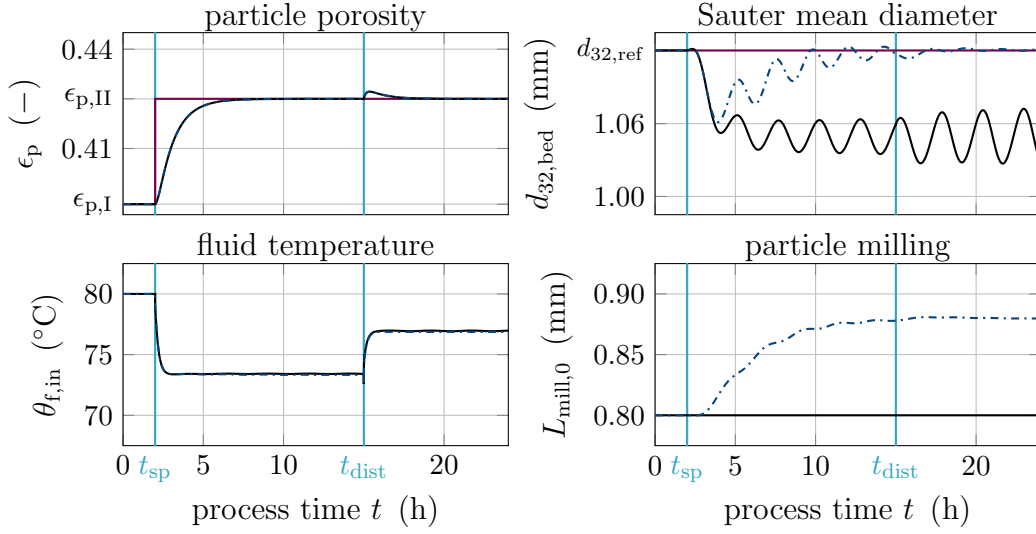
Figure 5.14.: Closed-loop simulations of scenario *Pro 5* according to SISO (—) and MIMO configuration ($-\cdot-$). At $t_{sp} = 2$ h reference value of particle porosity $\epsilon_{p,ref}$ is increased from 0.39 to 0.425; at $t_{dist} = 15$ h the moisture content Y_{in} is set from 6 $g_{f,wet}/kg_{f,dry}$ to 15 $g_{f,wet}/kg_{f,dry}$. The related PSDs are presented in Figure 5.15.
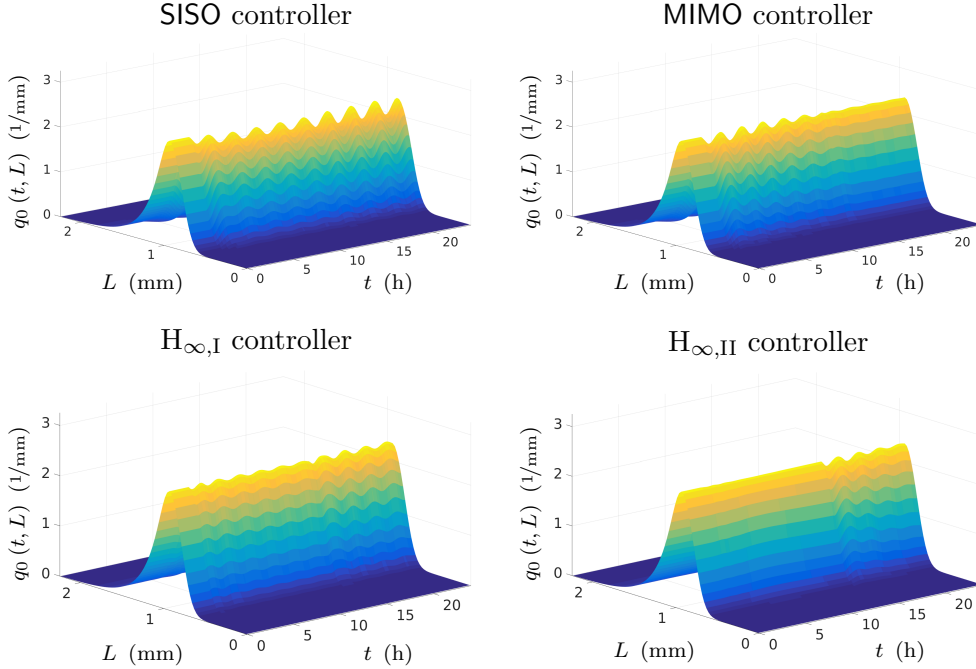
Figure 5.15.: Normalized particle size distributions $q_0(t, L)$ according to the closed-loop simulations. The corresponding process states are presented in Figures 5.14 and 5.20.

5.5. Mixed-sensitivity H$_\infty$ control

In the neighborhood of the nominal steady-state, the simultaneous application of the conventional PI controller $G_{\mathrm{PI},\eta}(s)$ and $G_{\mathrm{PI},d_{32}}(s)$ stabilized the FBLG process. Besides, it guaranteed the formation of particles with predefined apparent porosity ϵ_{p}. However,

(i) as shown by the simulations, the settling of the entire process after a reference step of $\epsilon_{\mathrm{p,ref}}$ is very slow (see Figures 5.14 and 5.15), and

(ii) process uncertainties may, in the worst case, lead to an unstable process regime.

Standard decentralized linear control does not provide a systematic approach for solving these problems. For instance, as illustrated in Figure 5.13, an increase of $k_{d_{32}}$ for increasing the process velocity shifts the dominant pole pair of the closed-loop system to the right half-plane such that the closed-loop system becomes unstable. To improve the process performance and the robustness anyhow, the application of advanced control concepts is promising. For instance, as shown by Palis & Kienle [79, 80], H$_\infty$ loop-shaping is capable of increasing process robustness of continuous FBLG processes. Further auspicious approaches to enhance process stability are adaptive control concepts [74, 77], model predictive control [14, 16], and non-linear control strategies [73, 75, 78, 81]. It is worth to mention that in the listed contributions SISO controllers were designed for controlling particle sizes only. Meanwhile, the thermal conditions of the FBLG were not in the scope of these investigations.

As shown by the simulations presented in Section 5.3, the bidirectional coupling of the particulate phase and the thermal conditions leads to a classical MIMO problem: Both of the actuating values $L_{\mathrm{mill},0}$ and $\theta_{\mathrm{f,in}}$ effect the designated control variables $d_{32,\mathrm{bed}}$ and η. The linearization of the corresponding non-linear system determines the 2×2 transfer function $G(s)$ of order 208. As illustrated in Figure 5.16, $\Delta L_{\mathrm{mill},0}$ actuates $\Delta d_{32,\mathrm{bed}}$ and $\Delta\eta$ via $G_{1,1}(s)$ and $G_{1,2}(s)$, while $\Delta\theta_{\mathrm{f,in}}$ excites the two control variables by $G_{2,1}(s)$ and $G_{2,2}(s)$. By balanced model truncation, the full-order system is reduced to the system $G_{\mathrm{red}}(s)$ of order 8. As shown by the frequency responses, presented in Figure 5.17, the two LTI systems $G(s)$ and $G_{\mathrm{red}}(s)$ are in good agreement. Hence, $G_{\mathrm{red}}(s)$ is a solid base for the controller design presented in the following.

The structure of the closed-loop system studied in the present section is illustrated in Figures 5.16 and 5.18. The possible influence of process disturbances and measurement noise is neglected. The related transfer-functions are given by

$$\mathbf{y}(s) = \underbrace{(I + GK)^{-1}GK}_{T(s)}\mathbf{r} \quad \text{and} \quad \mathbf{u}(s) = \underbrace{(I + GK)^{-1}K}_{S(s)}\mathbf{r} \qquad (5.26)$$

with the associated reference values $\mathbf{r}$, actuating values $\mathbf{u}$, and control values $\mathbf{y}$

$$\mathbf{r}(s) = \begin{bmatrix} \Delta d_{32,\mathrm{ref}} \\ \Delta\eta_{\mathrm{ref}} \end{bmatrix}, \ \mathbf{u}(s) = \begin{bmatrix} \Delta L_{\mathrm{mill},0} \\ \Delta\theta_{\mathrm{f,in}} \end{bmatrix}, \ \text{and} \ \mathbf{y}(s) = \begin{bmatrix} \Delta d_{32,\mathrm{bed}} \\ \Delta\eta \end{bmatrix} \qquad (5.27)$$

where $\Delta x(s)$ denotes the deviation between the nominal and actual value of the corresponding variable $x(s)$. The shapes of the sensitivity $S(s)$, the complementary sensi-
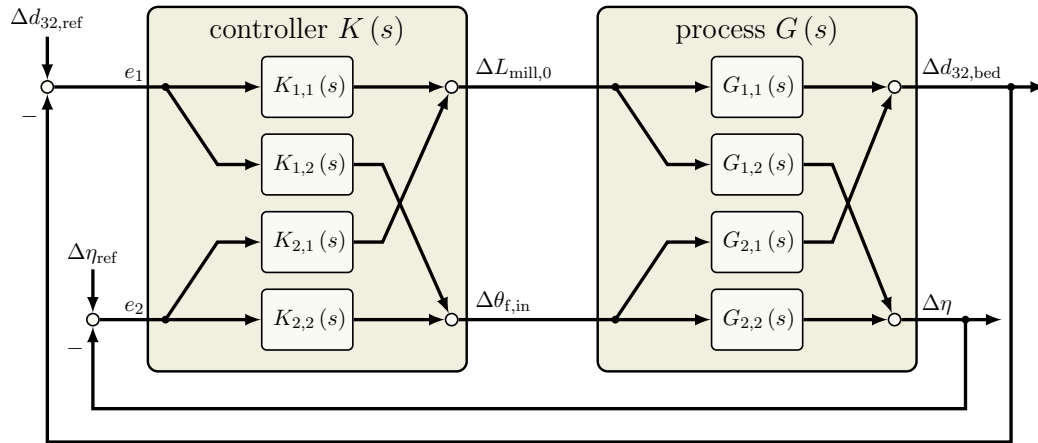
Figure 5.16.: MIMO control scheme: As both control variables $\Delta d_{32,\mathrm{bed}}$ and $\Delta\eta$ depend on the two actuating values, $\Delta L_{\mathrm{mill},0}$ and $\Delta\theta_{\mathrm{f,in}}$ are determined by the control errors $e_1 = (d_{32,\mathrm{ref}} - d_{32,\mathrm{bed}})$ and $e_2 = (\eta_{\mathrm{ref}} - \eta)$ in each case.
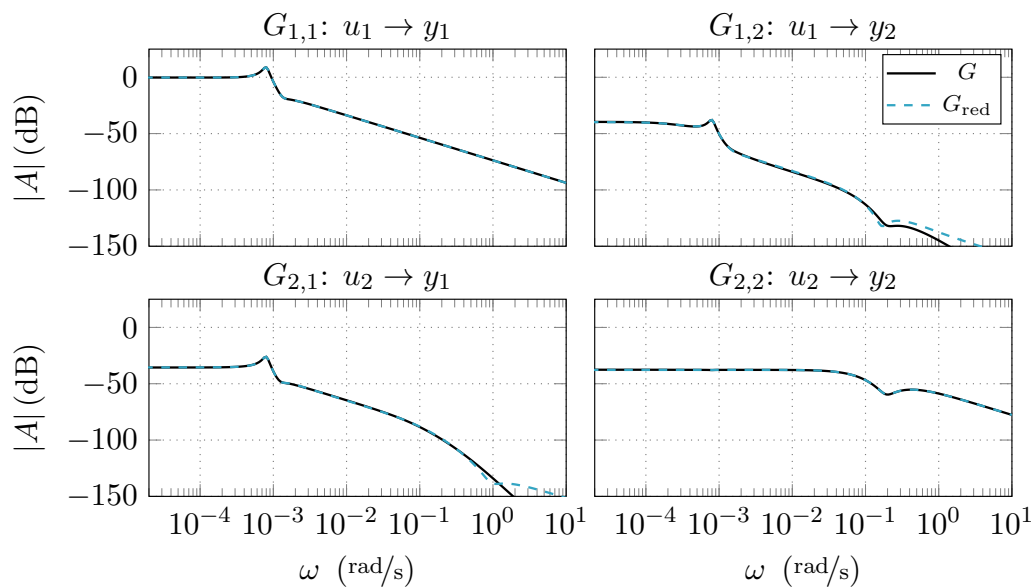
Figure 5.17.: Bode plots of the full-order transfer function $G(s)$ and the reduced system $G_{\mathrm{red}}(s)$.

tivity $T(s)$, and the control effort $K(s)S(s)$ determine several closed-loop objectives. Besides closed-loop stability, the following requirements are of particular interest in the present case [43, 100]:

(i) A good reference tracking demands $\overline{\sigma}(T) \approx \underline{\sigma}(T) \approx 1$.

(ii) For good disturbance attenuation, $\overline{\sigma}(S)$ should be small.

(iii) To limit the control effort, $\overline{\sigma}(KS)$ has to be small.

(iv) Robust stability in the presence of multiplicative output perturbations, details are given in the later, demands a small $\overline{\sigma}(T)$.

The terms $\underline{\sigma}(G)$ and $\overline{\sigma}(G)$ denote the minimum and maximum singular value of the frequency response of a transfer function $G(s)$. Singular values are a powerful tool of linear algebra with numerous applications in engineering science. Regarding control theories, the singular values of $G(s)$ are used as an extension to the Bode magnitudes for MIMO systems. In brief, they are a measure of the different gains of the transfer function $G(s)$ [26, 100].

The predefined closed-loop requirements (i) to (iv) are contradictory and cannot be satisfied simultaneously. During the controller design it is up to the engineer to find a reasonable trade-off between the different demands depending on the specific problem. However, especially in the case of MIMO systems, proper tuning of the feedback controller $K(s)$ is non-trivial. To design controllers that satisfy the requirements nevertheless, various control concepts were derived; for instance, the widely applied H_∞ control theory originating in the work of Zames [124]. In brief, the controller design in the framework of the H_∞ control theory is given as follows: First, the objectives for the controller design are specified. Together with the transfer function $G(s)$ of an open-loop stable dynamic system, an optimization problem is formulated. By minimizing the established problem, the transfer function of the controller $K_\infty(s)$ is determined. Thereby, the derived controller guarantees a robust closed-loop stability for the corresponding system. In general, the calculation of the optimal solution is theoretically and numerically complex. Instead, one restricts to find a sub-optimal solution that satisfies a specific upper constraint γ by an iterative solution of a series of sub-optimal problems [27, 39]. In practice, the performance of the determined sub-optimal controller $K_\infty(s)$ is usually of sufficient quality.

Two important procedures have been established for the controller design in the H_∞ framework [43]: the H_∞ loop-shaping design and the mixed sensitivity design. The first procedure was developed by McFarlane & Dover [59]. Here, the closed-loop objectives are specified in terms of requirements for the open-loop singular values of the compensated system $G_s(s)$. To shape the singular values of $G_s(s) = W_2 G W_1$, the pre- and post-compensator $W_1(s)$ and $W_2(s)$ are introduced. Based on $G_s(s)$, the controller $K_\infty(s)$ is determined.

The second procedure, the mixed sensitivity design, was first presented by Kwakernaak [54] and Verma & Jonckheere [112]. By simultaneous shaping of the frequency
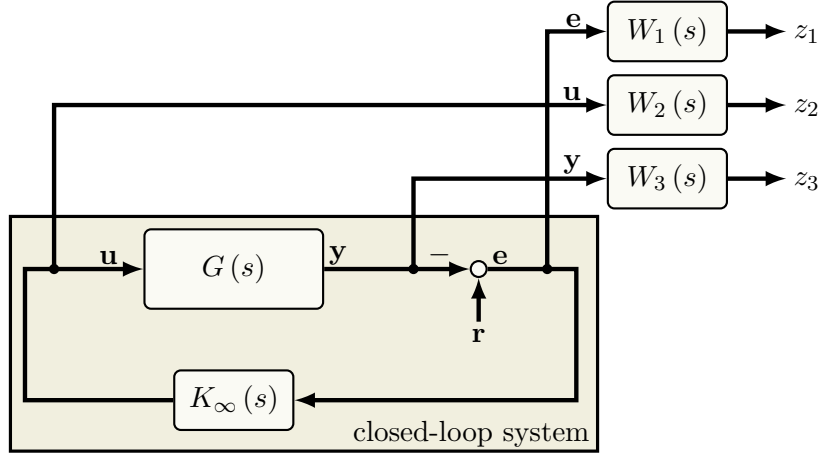
Figure 5.18.: Structure of the extended model including the weight functions $W_i(s)$. The highlighted part corresponds to the original closed-loop system.

response of the sensitivity $S(s)$, the complementary sensitivity $T(s)$, and the control effort $K_\infty(s) S(s)$ this technique determines an H_∞ controller $K_\infty(s)$ such that the predefined closed-loop objectives are fulfilled. Hence, the mixed sensitivity design is a reasonable procedure to balance the different demands for the controlled system. As a first step, the closed-loop system is virtually extended by the weight functions $W_1(s)$, $W_2(s)$, and $W_3(s)$. The Figure 5.18 presents the overall structure of the extended closed-loop system. As the introduced weights specify the control objectives, they are used to shape the transfer functions S, T, and $K_\infty S$. By solving the related optimization problem

$$\min_{K_\infty \text{ stabilize}} \underbrace{\left\| \begin{array}{c} S(s) W_1(s) \\ K_\infty(s) S(s) W_2(s) \\ T(s) W_3(s) \end{array} \right\|_\infty}_{\left\| T_{zr}(s) \right\|_\infty} \leq \gamma \;, \tag{5.28}$$

$T_{zr}(s)$ denotes the weighted sensitivity matrix, the H_∞ controller K_∞ is determined. For that purpose, the Robust Control Toolbox of MATLAB 2018b (The MathWorks, Natick, USA) was utilized. The resultant closed-loop transfer functions satisfy the inequalities

$$\begin{aligned} \overline{\sigma}(S(s)) &\leq \gamma \underline{\sigma}\left(W_1^{-1}(s) \right) \\ \overline{\sigma}(K_\infty(s) S(s)) &\leq \gamma \underline{\sigma}\left(W_2^{-1}(s) \right) . \\ \overline{\sigma}(T(s)) &\leq \gamma \underline{\sigma}\left(W_3^{-1}(s) \right) \end{aligned} \tag{5.29}$$

If the resulting γ, representing the peak singular value of the weighted sensitivity matrix T_{zr}, is below 1, the predefined design requirements for the closed-loop system are fulfilled.

In the remaining part of this section, two controllers are designed. First, focus is on

Table 5.4.: Parameter of the weights W_1, W_2, and W_3 related to H_∞ controllers $K_{\infty,\mathrm{I}}$ and $K_{\infty,\mathrm{II}}$. The weight functions $W_\mathrm{I}(s)$ and $W_\mathrm{II}(s)$ are given by Equations (5.30) and (5.31).

| | weights correlated to $K_{\infty,\mathrm{I}}$ | | | weights correlated to $K_{\infty,\mathrm{II}}$ | | | | |
	W_1	$W_{2,1}$	$W_{2,2}$	W_1	$W_{2,1}$	$W_{2,2}$	$W_{3,1}$	$W_{3,2}$
Typ	W_I	W_II	W_II	W_I	W_II	W_II	W_II	W_II
A	1.0×10^{-2}	$1.0 \times 10^{+5}$	$2.0 \times 10^{+3}$	5.0×10^{-3}	1.0×10^{-4}	$2.0 \times 10^{+3}$	4.0×10^{-1}	3.25×10^{-1}
ω_b	5.0×10^{-4}	—	—	7.5×10^{-5}	—	—	—	—
M	$1.5 \times 10^{+0}$	—	—	$1.5 \times 10^{+0}$	—	—	—	—
T	—	$1.0 \times 10^{+0}$	$1.0 \times 10^{+0}$	—	$1.0 \times 10^{+0}$	$1.0 \times 10^{+0}$	$3.5 \times 10^{+3}$	$1.25 \times 10^{+3}$
T_D	—	$1.0 \times 10^{+3}$	$2.0 \times 10^{+3}$	—	$1.0 \times 10^{+3}$	$2.0 \times 10^{+3}$	$7.5 \times 10^{+3}$	$4.0 \times 10^{+3}$
n	—	1	1	—	1	1	4	1

tracking behavior and disturbance attenuation, afterwards, the control design objective is robust stability of the closed-loop system.

5.5.1. Reference tracking & disturbance attenuation

The objectives of the first H_∞ controller $K_{\infty,\mathrm{I}}$ are an enhanced reference tracking and a improved disturbance attenuation. Assuming low-frequency changes in the references and low-frequency disturbances, $\overline{\sigma}(S)$ has to be small while $\underline{\sigma}(T)$ has to be unity for small frequencies. As the condition $S(s) + T(s) = I$ applies, both objectives can be fulfilled simultaneously by shaping the sensitivity S or the complementary sensitivity T.

For shaping the closed-loop sensitivity S by the weight W_1, the function

$$W_\mathrm{I}(s) = \frac{(T_\mathrm{p}s + 1)}{(MT_\mathrm{p}s + A)} \quad \text{with} \quad T_\mathrm{p} = {}^1\!/_{\omega_\mathrm{b}M} \tag{5.30}$$

is introduced. The correlated tuning parameters specify the closed-loop requirements: A determines the maximum stationary control error, M the desired damping, and the bandwidth ω_b the speed of the controlled system. A proper choice of the weight $W_2(s) = \mathrm{diag}(W_{2,1}, W_{2,2})$ limits the control effort. Therefore, the transfer function

$$W_\mathrm{II}(s) = \frac{A(T_\mathrm{d}s + 1)^n}{(Ts + 1)^n} \tag{5.31}$$

is utilized. As all control objectives are taken into account, the weight W_3 is not required in the present case. The utilized tuning parameter of W_1 and W_2 are presented in Table 5.4.

Based on the provided information, the controller $K_{\infty,\mathrm{I}}$ is calculated by solving the optimization problem defined by Equation (5.28). The controller is given by the state-
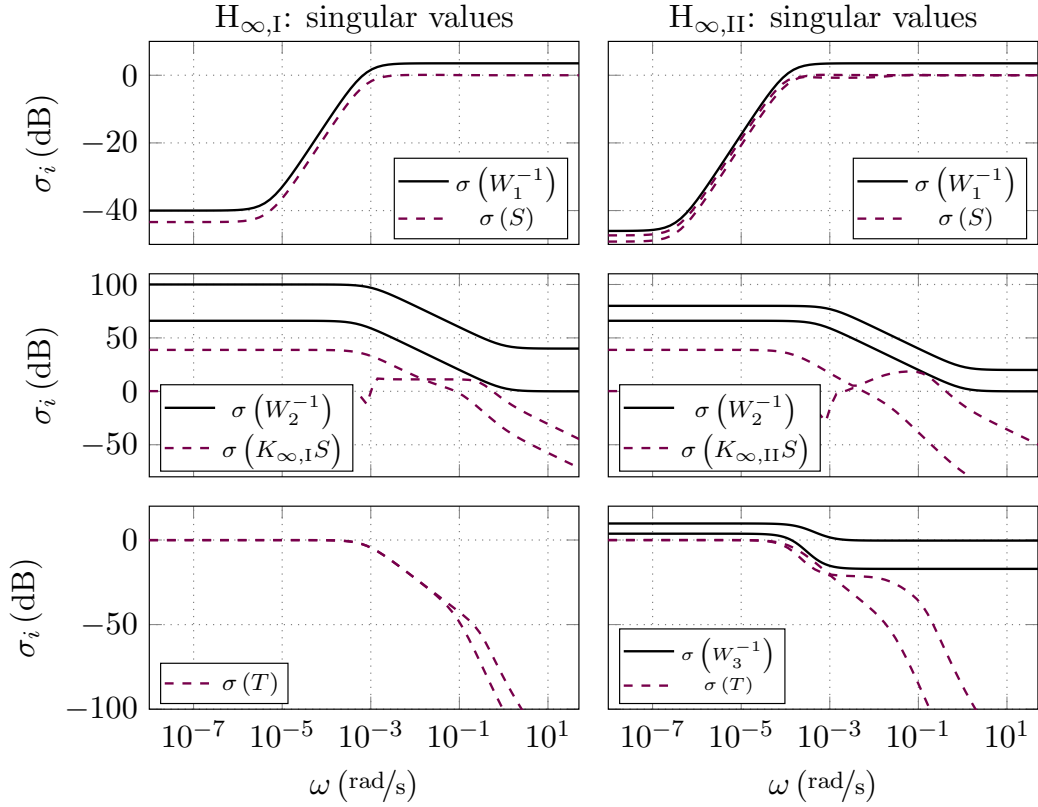
Figure 5.19.: Singular values of the closed-loop transfer functions $S(s)$, $T(s)$, and $K(s)S(s)$ compared to predefined weight functions $W_i(s)$. The **left** column is related to controller H$_{\infty,\text{I}}$, the **right** column to controller H$_{\infty,\text{II}}$.

Figure 5.20.: Closed-loop simulations of scenario *Pro 5* according to controller H$_{\infty,\text{I}}$ (—) and H$_{\infty,\text{II}}$ (- - -). At $t_{\text{sp}} = 2$ h, reference value of particle porosity $\epsilon_{\text{p,ref}}$ is increased from 0.39 to 0.425; at $t_{\text{dist}} = 15$ h, the moisture content Y_{in} is set from 6 $^{\text{g}_\text{f,wet}}/_{\text{kg}_\text{f,dry}}$ to 15 $^{\text{g}_\text{f,wet}}/_{\text{kg}_\text{f,dry}}$. The related particle size distributions are presented in Figure 5.15.

space model

$$
\begin{aligned}
s\mathbf{X}_K(s) &= A_K\mathbf{X}_K + B_K\mathbf{U}_K \\
\mathbf{Y}_K(s) &= C_K\mathbf{X}_K + D_K\mathbf{U}_K \\
\text{with} \quad \mathbf{U}_K(s) &= \begin{bmatrix} d_{32,\text{ref}} - d_{32,\text{bed}} \\ \eta_{\text{ref}} - \eta \end{bmatrix} \quad \text{and} \quad \mathbf{U}(s) = \mathbf{Y}_K
\end{aligned}
\tag{5.32}
$$

of order 12. The related system matrices are given in Appendix D. Figure 5.19 presents, together with the singular values of the predefined weights W_i, the closed-loop transfer function S, KS, and T. It becomes evident that the predefined requirements, see Equation (5.29), are fulfilled. Referring to the closed-loop simulation related to scenario *Pro 5*, the results are presented in Figures 5.15 and 5.20, the application of controller $K_{\infty,\text{I}}$ guarantees a stable process regime. Compared to the MIMO controller derived in previous Section 5.4.2 - the corresponding simulation results are given in Figure 5.14 - the H_∞ controller enhanced (i) the reference tracking after the set-point switch at $t_{\text{sp}} = 2$ h slightly and (ii) the rejection of the disturbance occurring at $t_{\text{dist}} = 15$ h significantly. However, as proven by the simulation of scenario *Pro 6*, scenario is given in Table 5.3; results are presented in Figure 5.21, the designed controller did not enhance the process robustness. After the set-point switch of ϵ_{p} from $\epsilon_{\text{p,I}}$ to $\epsilon_{\text{p,III}} = 0.37$ at t_{sp}, the reduction of the injection rate $\dot{m}_{\text{inj}}$ from 40.0 kg/h to 32.0 kg/h at t_{dist} destabilized the process. In consequence, self-sustained oscillations of the particle size distribution $n(t, L)$, represented by an oscillating Sauter mean diameter $d_{32,\text{bed}}$, arose. This issue is addressed in the subsequent section.

5.5.2. Robust stability

The aim of controller $K_{\infty,\text{II}}$ is a robust operation of the FBLG within a predefined domain, respecting process perturbations. The perturbations can, inter alia, be caused by process disturbances or by a shift of the operation point, for instance, induced by a change of the reference point. In the present case, the perturbations resulted from the following parameter variations:

- The nominal size of milled particles $L_{\text{mill},0}$ and the temperature of the fluidization medium at the inlet $\theta_{\text{f,in}}$ are utilized as actuating values. They are limited by the constraints $0.7\,\text{mm} \leq L_{\text{mill},0} \leq 0.9\,\text{mm}$ and $70.0\,°\text{C} \leq \theta_{\text{f,in}} \leq 90.0\,°\text{C}$, respectively.

- The injection rate $\dot{m}_{\text{inj}}$ and the moisture content of the fluid at inlet Y_{in} may vary over process time t. Interpreted as process disturbances, they are constrained by $32.0\,\text{kg/h} \leq \dot{m}_{\text{inj}} \leq 48.0\,\text{kg/h}$ and $0.0\,\text{g}_{\text{f,wet}}/\text{kg}_{\text{f,dry}} \leq Y_{\text{in}} \leq 15.0\,\text{g}_{\text{f,wet}}/\text{kg}_{\text{f,dry}}$.

Even though the perturbations occur in different parts of the system, they can be lumped into a single unstructured model uncertainty [43]. For that purpose, the stable open-loop transfer function $G(s)$ corresponding to the default parameter set $\Pi_{\text{pro},0}$ and a set of open-loop stable transfer functions $G(s; \Pi_{\text{pro},i})$ related to different uncertain parameter sets $\Pi_{\text{pro},i}$ are determined. The deviation between $G(s)$ and $G(s; \Pi_{\text{pro},i})$ is
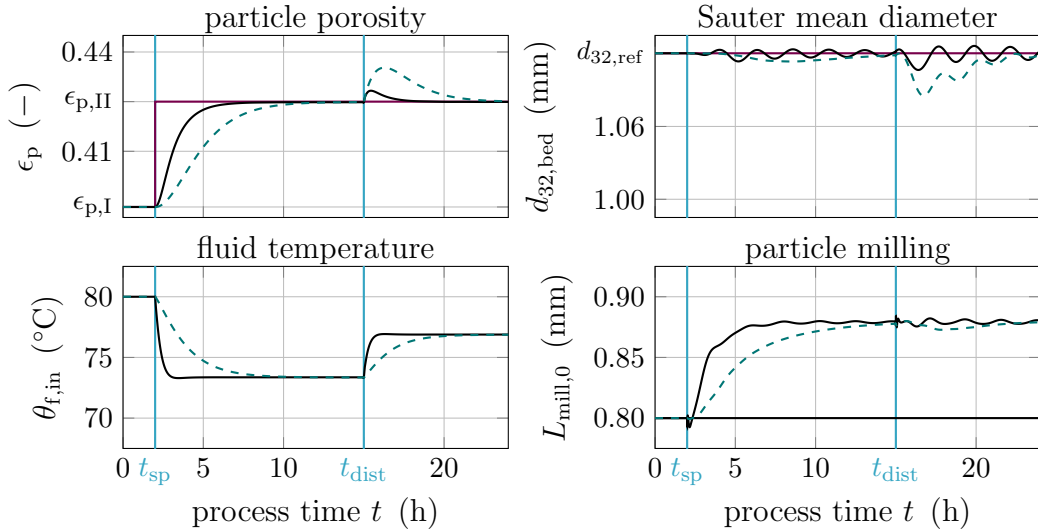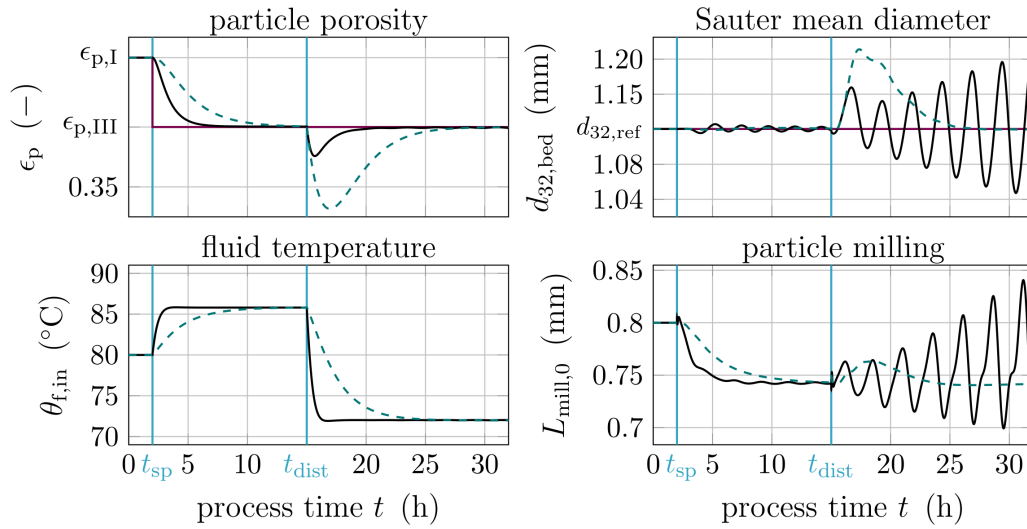
Figure 5.21.: Closed-loop simulations of scenario *Pro 6* according to controller H$_{\infty,\text{I}}$ (———) and H$_{\infty,\text{II}}$ (- - -). At $t_{\text{sp}} = 2$ h, reference value of particle porosity $\epsilon_{\text{p,ref}}$ is decreased from 0.39 to 0.37; at $t_{\text{dist}} = 15$ h, the injection rate is reduced from 40.0 kg/h to 32.0 kg/h.
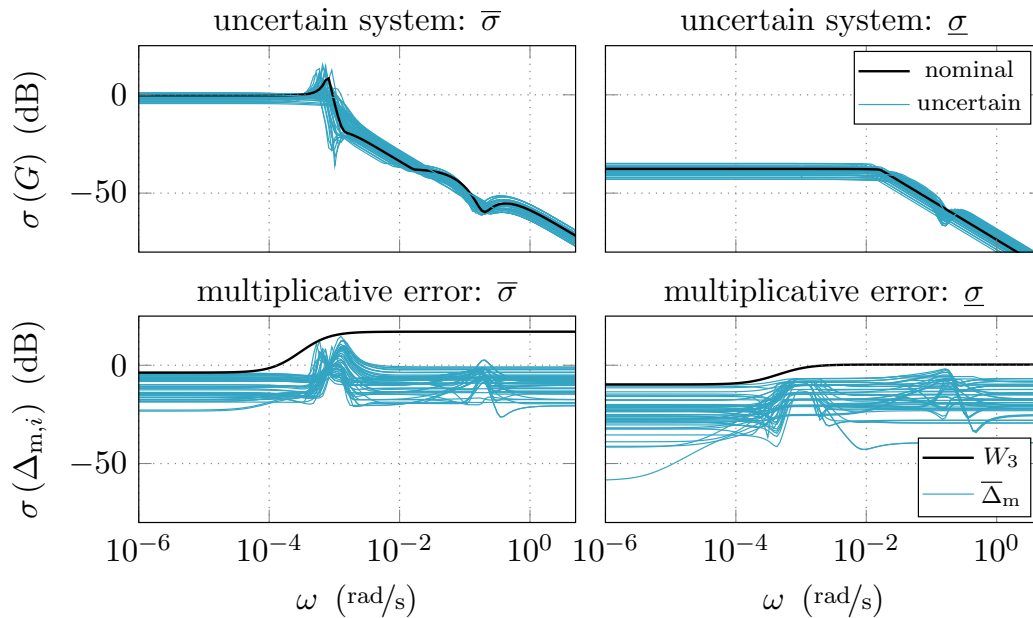
Figure 5.22.: Singular values of the open-loop frequency response of the uncertain system **(upper row)** and the corresponding multiplicative model uncertainty **(lower row)**.

quantified by the multiplicative model uncertainty

$$\Delta_{\mathrm{m},i}\left(\mathrm{s}; \Pi_{\mathrm{pro},i}\right) = \left[G\left(\mathrm{s}; \Pi_{\mathrm{pro},i}\right) - G\left(s\right)\right] G^{-1}\left(s\right). \tag{5.33}$$

Figure 5.22 presents the minimum and maximum singular values of the frequency response of the uncertain systems and the resultant multiplicative model error. The related parameter sets were determined by combining the permitted minimum, the nominal, and the permitted maximum value of the four uncertain parameters $L_{\mathrm{mill},0}$, $\theta_{\mathrm{f,in}}$, $\dot{m}_{\mathrm{inj}}$, and Y_{in}. Based on the resultant 80 combinations of the uncertain parameters, 51 open-loop stable LTI systems $G\left(\mathrm{s}; \Pi_{\mathrm{pro},i}\right)$ were determined. The remaining parameter combinations correspond, as illustrated in Figure 5.7, to open-loop unstable systems or, as the injection rate is to high with respect to the thermal conditions, to not feasible operating conditions.

The upper boundaries $\overline{\Delta}_{\mathrm{m}}\left(s\right)$ limit the singular values of the multiplicative model error. For the controller design, $\overline{\Delta}_{\mathrm{m}}\left(s\right)$ are approximated by the function $W_{\mathrm{II}}\left(s\right)$ given by Equation (5.31) with the tuning parameters presented in Table 5.4. The desired proper operation of the FBLG within the predefined parameter constraints demands robust stability. Based on the Small-Gain theorem [123], it can be shown that $\overline{\sigma}\left(T\right) < \underline{\sigma}\left(\overline{\Delta}_{\mathrm{m}}^{-1}\right)$ is a sufficient for robust stability in the presence of the given multiplicative model uncertainty [43]. Referring to Equation (5.29), the controller $K_{\infty,\mathrm{II}}$ designed by the mixed sensitivity design fulfills the inequality $\overline{\sigma}\left(T\right) \leq \gamma\underline{\sigma}\left(W_3^{-1}\right)$. Hence, setting $W_3\left(s\right) = \mathrm{diag}\left(\overline{\Delta}_{\mathrm{m}}\right)$, robust stability of the closed-loop system is guaranteed if $\gamma < 1$ is fulfilled.

In consequence of the introduced weight W_3, the weight W_1 has to be adjusted: A successful shaping of the open-loop transfer function $K_{\infty,\mathrm{II}}G$ during the controller design procedure demands that the crossover frequency ω_{c} of $\sigma\left(W_1\right)$, viz. $\sigma\left(W_1\left(\omega_{\mathrm{c}}\right)\right) = 0$ dB, is smaller than the crossover frequency of $\sigma\left(W_3\right)$ [43]. The parameter set of the used weights W_i is presented in Table 5.4. Again, the controller $K_{\infty,\mathrm{II}}$ is calculated by solving the optimization problem defined by Equation (5.28). The resulting γ equals 0.95. The corresponding state-space representation of the controller is given in Appendix D. Figure 5.19 presents the related weights $W_i\left(s\right)$ and the determined closed-loop transfer functions. Again, the inequality conditions defined by Equation (5.29) are fulfilled.

As the resulting γ is smaller than one, robust stability of the closed-loop system is achieved for the considered multiplicative model uncertainty. In consequence, the designed controller $K_{\infty,\mathrm{II}}$ is capable of suppressing the considered process uncertainties as, for instance, variations of the injection rate $\dot{m}_{\mathrm{inj}}$ as in scenario $\Pi_{\mathrm{pro},6}$. Referring to the corresponding simulation results, presented in Figure 5.21, the designed controller $K_{\infty,\mathrm{II}}$ is capable of stabilizing - in contrast to controller $K_{\infty,\mathrm{I}}$ - the FBLG after the set-point switch and process disturbance at t_{sp} and t_{dist}, respectively.

The application of $K_{\infty,\mathrm{II}}$ enhances the process stability: As proven by the stability map related to the closed-loop systems, presented in Figure 5.23, $K_{\infty,\mathrm{II}}$ shifts the stability boundary to smaller values of $L_{\mathrm{mill},0}$ and $\theta_{\mathrm{f,in}}$. Therefore, the controller $K_{\infty,\mathrm{II}}$ increases the domain where the process can be operated under steady-state conditions.
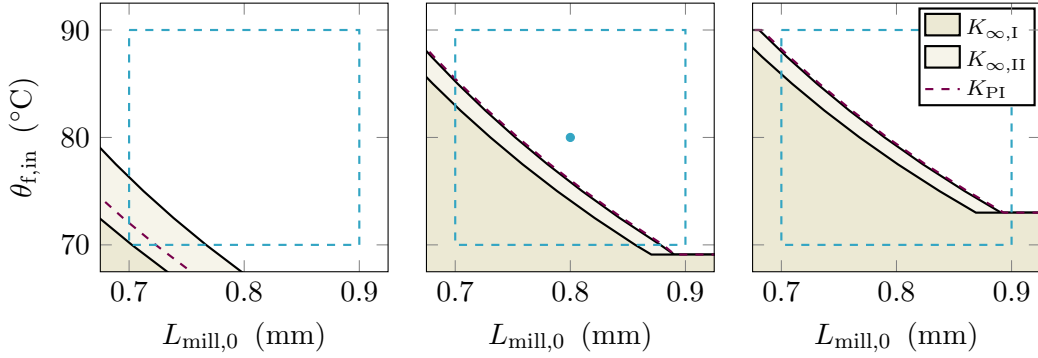
Figure 5.23.: Local stability of the uncertain closed-loop systems $K_i G\left(\mathrm{s}; \Pi_{\mathrm{pro},i}\right)\left(I + K_i G\left(\mathrm{s}; \Pi_{\mathrm{pro},i}\right)\right)^{-1}$ for the designed MIMO controllers. From the left to the right, $\dot{m}_{\mathrm{inj}}$ and Y_{in} equals 32 $^{\mathrm{kg}}/_{\mathrm{h}}$ and 6 $^{\mathrm{g}_{\mathrm{f,wet}}}/_{\mathrm{kg}_{\mathrm{f,dry}}}$, 40 $^{\mathrm{kg}}/_{\mathrm{h}}$ and 6 $^{\mathrm{g}_{\mathrm{f,wet}}}/_{\mathrm{kg}_{\mathrm{f,dry}}}$, and 40 $^{\mathrm{kg}}/_{\mathrm{h}}$ and 15 $^{\mathrm{g}_{\mathrm{f,wet}}}/_{\mathrm{kg}_{\mathrm{f,dry}}}$. The shaded domains indicate an unstable steady-state. The predefined reference point and workspace are indicated by the marker (●) and the dashed line (- - -), respectively.

On the contrary, as illustrated in Figure 5.20, the velocity of the reference tracking and disturbance attenuation decreased significantly.

By designed, the derived controller guarantees a stable closed-loop behavior only if the corresponding open-loop system is stable, too. As the underlying stability criterium - the Small-Gain theorem - is conservative, the controller might stabilize open-loop unstable systems as well. However, comparing the open and closed-loop stability-maps presented in Figures 5.7 and 5.23, the application of the robust controllers did not increase the stability domain significantly. If an operation in the open-loop unstable domain is required, other control concepts have to be utilized. For instance, as shown by Palis & Kienle [79], the briefly introduced H_∞ loop-shaping approach is capable of stabilizing an FBLG within the open-loop stable and unstable domain.

5.6. Multi-stage FBLG & future perspectives

The control strategies presented so far enable the formulation of particles with a predefined porosity under steady-state conditions. Naturally, the presented methods can be adopted such that other product properties, e.g., moisture content or temperature, can be controlled. However, if more than one product property should be controlled simultaneously, further degrees of freedom might be required. One way to provide additional degrees of freedom in FBLG is the multi-stage configuration.

As illustrated in Figure 5.24, integrated weirs divide the process chamber into separate stages in multi-stage FBLG. In consequence, different thermal conditions can be realized, allowing the operator to combine several process steps within one operation unit. For instance, as reported by Bertin et al. [6] for an industrial FBLG process, the
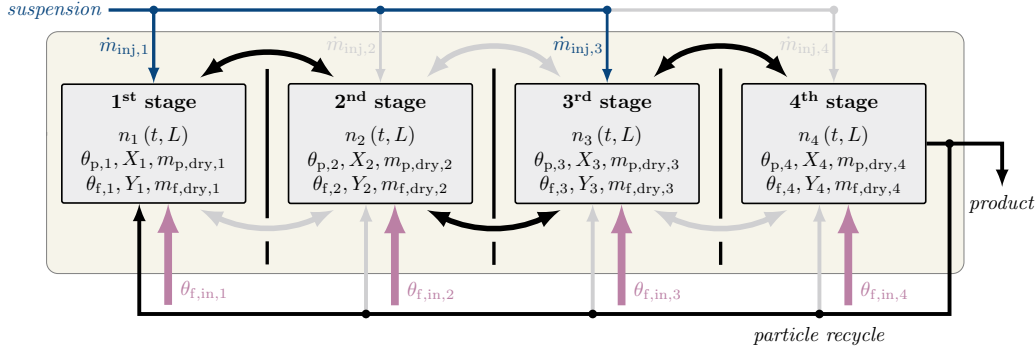
Figure 5.24.: Flow sheet of a multi-stage FBLG process.

process chamber can be subdivided into growth, drying, and cooling stages.

For taking multi-stage operation into account, the dynamic model has to be extended. As an example, the PBM of the ith stage is given by

$$\frac{\partial n_j\,(t,L)}{\partial t} = -G_j \frac{\partial n_j}{\partial L} + \dot{n}_{\text{in},j} - \dot{n}_{\text{out},j} \ , \tag{5.34}$$

where the growth rate G_j depends on the related injection rate $\dot{m}_{\text{inj},j}$ while the particle flow-rates $\dot{n}_{\text{in},j}$ and $\dot{n}_{\text{out},j}$ represent the particle exchange between the respective stage and surrounding stages as well as with the periphery. Depending on the investigated configuration, the remaining system equations (5.2) – (5.25) , e.g., to account for the particles' temperature $\theta_{\text{p},j}$ and moisture content X_j on stage j, can be adopted straightforwardly.

The dynamic model can be used to investigate the influence of different configurations and operating parameters on the process and product properties. Of particular interest is the impact of the weirs on the particle transport. As shown by experiments [62, 116] and CFD-DEM simulations with mono-disperse particle populations [22], the configuration, e.g., overflow, side-flow, and underflow, influences significantly the particle exchange rate between different stages. However, as the exchange depends on the particles' size [22], classifying particle transport is expected for continuously operated multi-stage processes with a particle populations widespread in their sizes. Compared to the representative transport across the weirs, as illustrated by the simulation results presented in Figure 5.25, the classifying particle transport leads to a change in the particle size distribution in the stages: While the first stage contains small particles, large particles are mainly in the last stage. Hence, the multi-stage operation allows for better control of the particle growth, for example, by applying different fluidization conditions and injection rates in the individual chambers. Further conceivable applications of multi-stage FBLG are the integration of nucleation processes in the early and finishing processes in the later stages. For instance, the last chamber can be used for applying a protection layer or for the cooling of the product particles.

Besides product properties, the configuration of multi-stage FBLG influences the process stability. As illustrated in Figure 5.25 and Appendix E, the introduction of drying
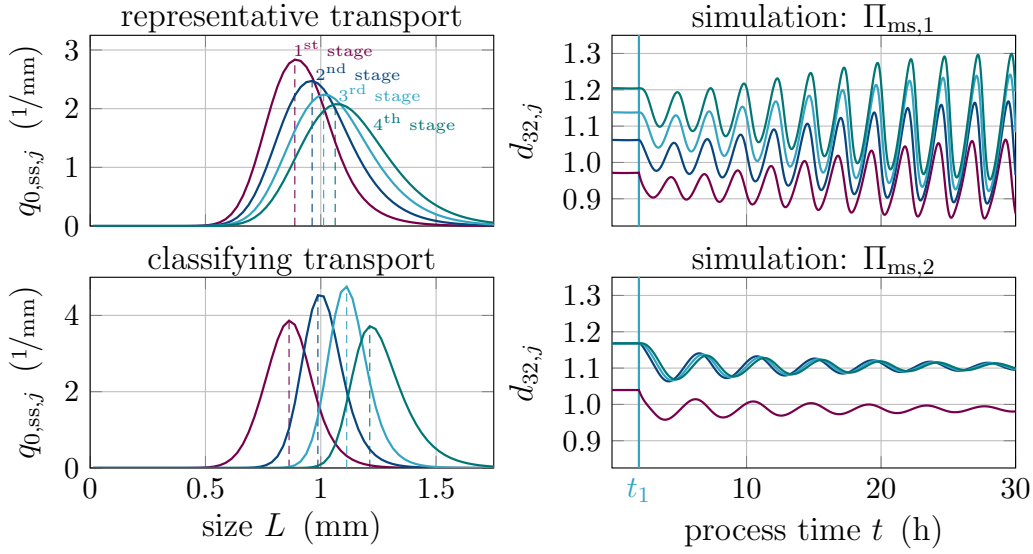
Figure 5.25.: Simulation results regarding four-stage FBLG: **Left column:** influence of the classifying particle transport over the weirs on the particle size distribution on the stages at steady-state; **Right column:** Influence of drying stages ($\Pi_{\mathrm{ms},2}$) on process dynamics. A detailed presentation of the corresponding simulation results is given in Appendix E.

stages, viz. no suspension is injected, enhances the process stability. This outcome is in line with the findings presented in Chapter 3.3: The reduction of the overall injection rate $\sum \dot{m}_{\mathrm{inj},j}$ increases the mean residence time of particles in the FBLG τ_{process}, resulting in a more stable process regime.

5.7. Concluding remarks

The objective of the present chapter was to illustrate how PBM can be used to formulate tailor-made particles in continuous FBLG under stable steady-state conditions. As a first step, the population balance model was extended by a system of ODE functions to account for thermal conditions in the FBLG. The two sub-systems - the PBM and the ODE system - were interconnected, inter alia, by introducing the drying potential η. Based on an experimentally determined correlation [91], the shell porosity $\epsilon_{\mathrm{shell}}$ and, in consequence, the apparent particle porosity ϵ_{p} are linked to the drying potential. As shown by dynamic simulations and stability analyses, presented in Section 5.3, the process stability depends on (i) the particle milling and (ii) on the thermal conditions. The theoretical findings are in qualitative agreement with the experimental observations of Schmidt et al. [92, 94].

As indicated by open-loop simulations, the formulation of tailored particles under stable steady-state conditions is challenging as uncertainties and disturbances may perturbate the FBLG process. For achieving these objectives, different feedback controllers were

designed and tested in Sections 5.4 and 5.5. As a first approach, a single input single output controller was designed to regulate the particles' porosity ϵ_p by manipulating the temperature of the fluidization medium $\theta_{\mathrm{f,in}}$. Even though the controller was capable of controlling the designated product quality, a shift of the related reference value $\epsilon_{\mathrm{p,ref}}$ resulted in the occurrence of self-sustained oscillations of the particle size distribution. For preventing this process instability, the controller was augmented by a second control loop: by adjusting the particle milling, the Sauter mean diameter $d_{32,\mathrm{bed}}$ of the particle bed was controlled. In consequence, a stationary profile of the particles size distribution established after a sufficient settling time.

In contrast to the SISO controller, the resultant decentralized multiple input multiple output controller enabled a stable FBLG and guaranteed the formation of particles with tailored porosity. Referring to the simulation results, presented in Figure 5.14, the transient response of the closed-loop system is quite slow. As a further tuning of the parameters of the decentralized MIMO controller can not enhance the process dynamics significantly, the application of an advanced control strategy was tested afterward.

In particular, two H_∞ controller were derived by mixed-sensitivity design: While the objective of the first controller was an enhancement of process performance in terms of reference tracking and disturbance attenuation, the second controller aimed at an increase of robustness against process uncertainties. By selecting appropriate weight functions during the design, the controllers $\mathrm{H}_{\infty,\mathrm{I}}$ and $\mathrm{H}_{\infty,\mathrm{II}}$ were determined. Referring to the related closed-loop simulations presented in Figure 5.20 and 5.21, the two goals were achieved.

So far, the scope of the investigations was the formulation of particles with a desired porosity under steady-state conditions. For accounting further product properties, the presented dynamic model can be extended by empirical and first-principle correlations. Another promising application of the derived model is the investigation of multi-stage FBLG. Due to the complex linkage of particles, mass, and energy flows within this configuration, the effect of parameter changes on the process dynamics and product qualities is not always evident nor transparent. It is for that reason that the presented dynamic model, along with dynamic simulations and theoretical analyses, might be a valuable tool for improving the process understanding. Then again, the multi-stage model can be utilized to determine the process configuration and the correlated set of operating parameters such that tailor-made particles are formulated. Thereby, the dynamic model can be used to optimize energy consumption [63] and minimize operating costs.

Finally, combined with parameter and state estimation methods, as recently presented by Otto et al. [72] and Dürr et al. [30], the derived model for online monitoring and model adaption.

6

Summary & future perspectives

Fluidized bed layering granulation is an essential class of particulate process widely applied in different fields of processing industries. One option to achieve high throughput of product particles with uniform properties is the continuous operation of FBLG. In this configuration, particles that fulfill product specifications are permanently withdrawn from the process, while nuclei have to be supplied. The required nuclei can be obtained by internal, e.g., thermal overspray, or external processes, e.g., milling of oversized particles. Even if this modes offer promising advantages in comparison to a batch-wise operation, a stable operation of continuous FBLG under steady-state conditions is a challenging task: Depending on the operating parameters, the process tends to instability in the form of self-sustained oscillations. As those oscillations lead to variations of mass flows and product properties over process time and may - in the worst case - induce a process breakdown, they are highly undesired.

After an introduction to fluidized bed layering granulation, the presented thesis started with a motivation of the occurrence of instabilities of continuous FBLG by means of theoretical analyses and experiments. For theoretical investigations, different population balance models were designed and utilized. Based on the finding and the established process models, a control concept to ensure a process regime under steady-state conditions was designed and successfully tested. Subsequently, the dynamic model was extended to account for particles' properties as porosity, temperature, and moisture content. The extended model was the foundation to study the influence of operating parameters on process stability and product properties. Based on the findings, different model-based controllers were designed capable of controlling particle properties and of guaranteeing an operation under stable steady-state conditions. Finally, a brief introduction to multi-stage FBLG processes was given.

Throughout this thesis, different novel contributions concerning continuous FBLG were elaborated and presented:

- In Chapter 3 the influence of the process configuration and operating parameters on the dynamic stability of continuously operated FBLG with internal and external nucleation was studied. By means of numerical stability analysis it was shown for both configurations that the interplay of nucleation and particle growth has

a significant influence on dynamic stability. Furthermore, the influence of the formation of functional zones - the process chamber divides into spraying and drying zone - on dynamics was of particular interest in this chapter. In contrast to the intuitive expectations of the process engineers, the dynamic models predicted a moderate influence of zone formation on process stability.

- The aim of Chapter 4 was a continuous operation of a pilot-scale FBLG with external nucleation by milling oversized particles under steady-state conditions. As a reminder, in the setting of continuous FBLG, a stable steady-state operation is characterized by a constant bed mass and a stationary profile of the particle size distribution over process time.

  A series of experiments confirmed the previous theoretical findings: While fine milling resulted in the occurrence of self-sustained oscillations, the observed oscillations were slightly decaying for coarser milling. However, even for coarser milling, steady-state conditions were not achieved due to the large settling times of the process. A simulation study accompanied the plant experiments. As simulation results and experimental data were in good agreement, the underlying dynamic process model was utilized for the design of a feedback control strategy. Based on the measure of a representative of the particle size distribution, the milling process was actuated. The designed control strategy was successfully applied and validated. For the first time, it was proven experimentally that the application of feedback control is capable of enhancing the process dynamics of FBLG such that the process settled at a stable steady-state within a short period.

- The formation of tailor-made particles in a stable process regime was within the scope of Chapter 5. For that purpose, a population balance model was extended to account for thermal conditions. Based on an experimentally determined correlation, the state of the fluidization medium was linked to a key product property - the porosity of the particles. By this linkage, a bidirectional coupling of particles and fluidization medium was achieved. The developed dynamic model was used to investigate the influence of the operating parameter on the process stability and product properties. By means of a stability analysis, it was shown that process stability also depends on the thermal operating parameters. The derived theoretical results are in qualitative agreement with the experimental findings of Schmidt et al. [92, 94].

  For achieving both objectives - the formation of tailored product particles and a stable steady-state operation - the application of multiple input multiple output controller is required. For that purpose, decentralized and centralized controllers were designed and validated by simulations. Comparing the two approaches, the performance and robustness of the closed-loop systems related to the centralized controllers are superior.

In summary, the present thesis showed that population balance modeling is a valuable tool in the context of continuously operated fluidized bed layering granulation. Based on the degree of detail, the dynamic models are capable of predicting the process

dynamics qualitatively and quantitatively. Therefore, they can be used to enhance the understanding of the dynamics of continuous granulation processes. Furthermore, the PBM can be used for the design of model-based controllers to enhance process dynamics and robustness. Finally, it was shown that the PBM could be extended to account for additional particle properties.

For future directions, especially the last issue is of great relevance: The dynamic model can be extended by empirical or first-principle correlations to consider further product properties. Thereby, the extended model can be used for an in-silico product and process design. If product particles are defined by a manifold of desired properties or operating constraints limit the process, e.g., a maximum temperature of the particles, a multi-stage operation might be required. Here, the separation of the process chamber into different operating stages provides new degrees of freedom to influence the particles' growth and product properties. Along with parameter and state estimation methods, the framework of PBM can be used for the design of more advanced, model-based control strategies.

Appendix

A Measuring of particle size distributions

A population of particles consists of a large number of individuals characterized by its properties. As the indented objective of granulation processes is the size enlargement, the focus of this section is on the property particle size. Assuming a population of spherical particles, the diameter L represents the size of an individual.

For describing the entirety of the particle population at time t with respect to the size, the property-space L is subdivided into classes L_j. Hereby, the class j is limited by a lower boundary $\underline{L}_j$ and an upper boundary $\overline{L}_j$. Particles that share the same class are combined into

$$n^\star (t, L_j) = \text{number of particles in class } j \tag{A.1}$$

such that the *number distribution* $n^\star$ describes the size distribution of the population.

In practice, different methods are available to determine the number distribution of a particle population. Throughout the presented experiments, two different devices were utilized for measuring: (i) a CamSizer XT (Retsch Technology, Germany) was used for sizing withdrawn samples in the post processing, (ii) a Parsum IPP 70-S probe (Parsum GmbH, Germany) was applied for real-time inline measuring. Figure A.1 compares the functionality of the two methods. Based on images of the particles, the CamSizer XT determines the equivalent particle size L by digital imaging processing. For this purpose, the particles are idealized as spheres. In contrast, the Parsum IPP 70-S probe determines the chord length L_c of the particles by spatial filter velocimetry [85]. Since the chord length of a particle is not unique, for instance, this quantity depends on the position of the measuring on the particle, the two derived number density distributions differ. For a population of spherical particles, Fischer et al. [34] showed that the chord length distribution could be converted to the number distribution.

By dividing $n^\star (t, L_j)$ by the width of the respective classes $\Delta L_j = \overline{L}_j - \underline{L}_j$, the *number density distribution*

$$n (t, L_j) = {n^\star (t, L_j)}/{\Delta L_j} \tag{A.2}$$

is determined. Assuming that ΔL_j tends to zero, the discrete formulation of the number density distribution can be converted to the continuous formulation. The resultant
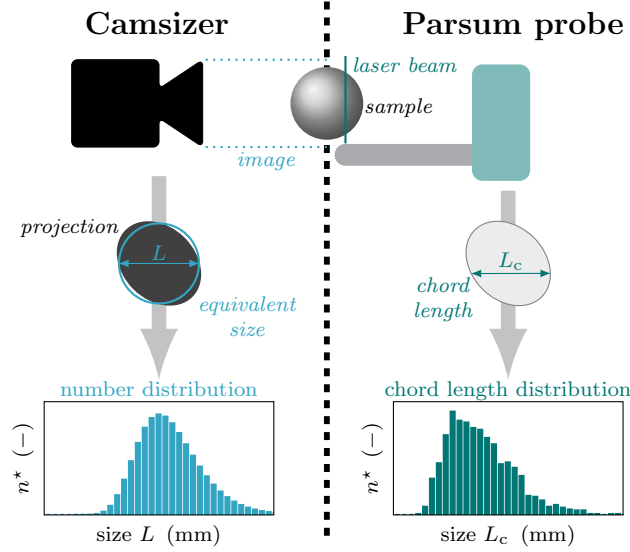
Figure A.1.: Schemes of measuring the number distributions $n^\star (t, L)$ with the CamSizer XT (**left column**) and the Parsum IPP 70-S probe (**left column**).

function $n(t, L)$ is denoted as *particle size distribution* (PSD) throughout this thesis. For comparing the particle size distributions of different samples, the *normalized particle size distribution* is introduced. For that purpose, the particle size distribution of the sample is normalized with respect to the overall number of particles within the sample. Hence,

$$q_0 (t, L) = \frac{n (t, L)}{\mu_0 (n (t, L))} \quad \text{with} \quad \mu_i = \int_0^\infty L^i n (t, L) \, \mathrm{d}L \tag{A.3}$$

determines normalized particle size distribution. The subscript i of $q_i (t, L)$ indicated the type of the measured quantity: 0 relates to the number, 1 to the length, 2 to the surface, and 3 to the volume. Assuming a population of spherical particles, the normalized particle size distribution q_i can be converted to q_j by

$$q_j (t, L) = \frac{L^{(j-i)} q_i (t, L)}{\int_0^\infty L^{(j-i)} q_i (t, L) \, \mathrm{d}L}. \tag{A.4}$$

In the present thesis, the *number-based* $q_0 (t, L)$ and the *volume-based normalized particle size distribution* $q_3 (t, L)$ are of particular interest. A further important class of size distributions are *normalized cumulative particle size distributions*:

$$Q_i (t, L_\mathrm{x}) = \int_0^{L_\mathrm{x}} q_i (t, L) \, \mathrm{d}L \ . \tag{A.5}$$

Here, the value $Q_i (t, L_\mathrm{x})$ denotes the i-based fraction of particles that are smaller than the specified size L_x. Figure A.2 illustrates the normalized (cumulative) particle size distributions for different i.

Besides the introduced distributions, a characteristic value can be used for describing the state of the particle size distribution. In the scope of particulate processes, the mean
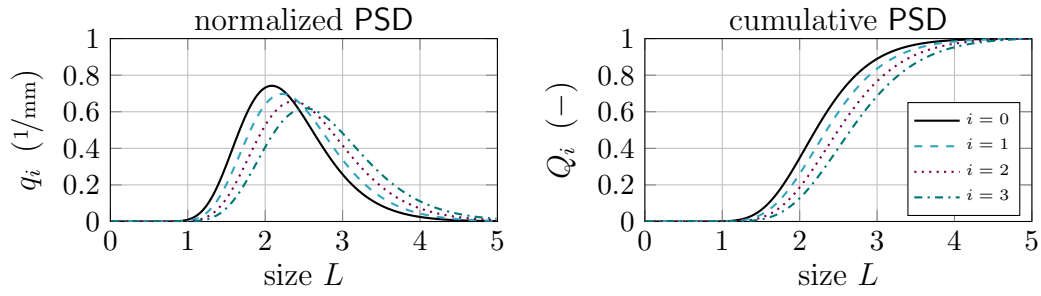
Figure A.2.: Normalized (cumulative) particle size distribution related to particles'
number ($i = 0$), size (1), surface (2), and volume (3).

value, the median, and number or mass-based quantiles are frequently used. Throughout the present thesis, the Sauter mean diameter $d_{32,\text{bed}}$, defined by

$$d_{32,\text{bed}}\left(t\right) = \frac{\mu_3\left(n\left(t, L\right)\right)}{\mu_2\left(n\left(t, L\right)\right)} \tag{A.6}$$

is used as a representative of the particle size distributions $n\left(t, L\right)$ and $q_0\left(t, L\right)$.

Supercritical Hopf bifurcation

From practical observations, it is well known that the qualitative behavior of a dynamic system depends not only on the current state but also on its system parameters. As illustrated by simulating the non-linear system

$$\dot{x}_1\left(t\right) = -x_2 + \left(\left(\mu - 1\right) - x_1^2 - x_2^2\right) x_1$$
$$\dot{x}_2\left(t\right) = +x_1 + \left(\left(\mu - 1\right) - x_1^2 - x_2^2\right) x_2 \ ,$$

the parameter μ determines the qualitative behavior. Referring to the simulation results presented in Figure B.1 the system settles at a stable steady-state for $\mu = 0.80$ while self-sustained oscillations arise for $\mu = 1.20$. To investigate the influence of the parameter μ
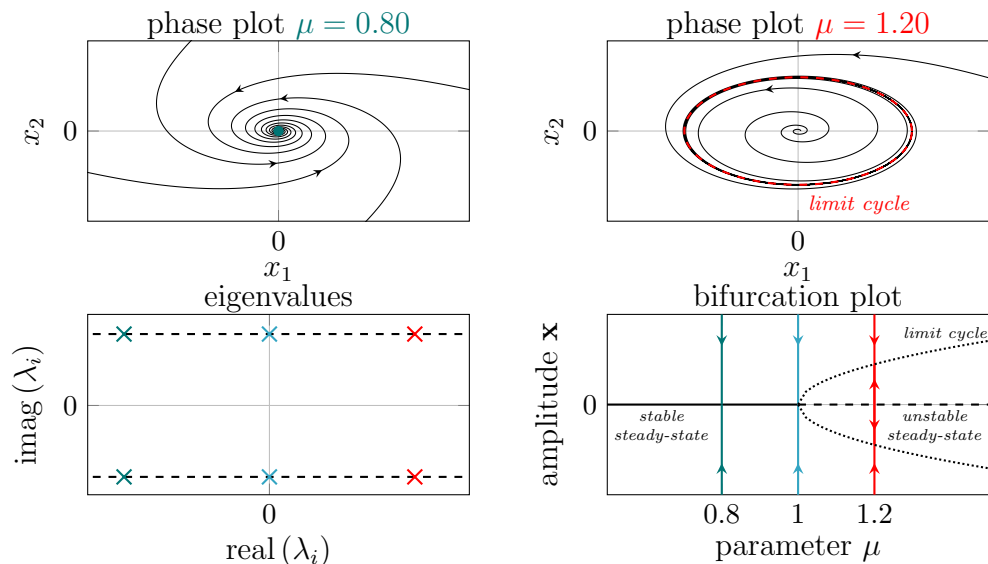
Figure B.1.: Illustration of a supercritical Hopf bifurcation: **Upper row:** phase plots of the simulations corresponding to the bifurcation parameter $\mu = 0.8$ and $\mu = 1.2$; **Lower Left:** complex plane of eigenvalues of the linearized system with respect to μ; **Lower Right:** bifurcation diagram.

on the dynamics, the local stability of the corresponding steady-state $x_{1,\mathrm{ss}} = x_{2,\mathrm{ss}} = 0$ is studied. Therefore, the system is linearized:

$$\partial \dot{x}_1/\partial x_1 = -3x_1^2 + (\mu - 1) - x_2^2 \qquad \partial \dot{x}_1/\partial x_2 = -2x_1 x_2 - 1$$
$$\partial \dot{x}_2/\partial x_1 = -2x_1 x_2 + 1 \qquad \partial \dot{x}_2/\partial x_2 = -3x_2^2 + (\mu - 1) - x_1^2 \ .$$

By determining the eigenvalues of the Jacobian matrix related to the steady-state $\mathbf{x}_{\mathrm{ss}}$

$$J|_{x_{\mathrm{ss}}} = \begin{bmatrix} \partial \dot{x}_1/\partial x_1|_{x_{\mathrm{ss}}} & \partial \dot{x}_1/\partial x_2|_{x_{\mathrm{ss}}} \\ \partial \dot{x}_2/\partial x_1|_{x_{\mathrm{ss}}} & \partial \dot{x}_2/\partial x_2|_{x_{\mathrm{ss}}} \end{bmatrix} = \begin{bmatrix} (\mu - 1) & -1 \\ +1 & (\mu - 1) \end{bmatrix} \ ,$$

the corresponding local stability can be specified. In the present case,

$$\lambda_{1/2} = (\mu - 1) \pm \sqrt{-1}$$

holds. Hence, as real $(\lambda_i) < 0 \ \forall \ i$ is a necessary and sufficient condition for local stability, the steady-state is stable for $\mu < 1$. On the contrary, the steady-state becomes unstable if $\mu > 1$.

In the present case, the loss of stability at the bifurcation point $\mu = 1$ coincides with the formation of a branch of a stable limit cycles [98]. In consequence, as corroborated by the simulation results, the process does not converge towards the steady-state but approaches the limit cycle leading to the observed self-sustained oscillations. This pattern of behavior is termed as supercritical Hopf bifurcation (Seydel [98]).

In general, an analytic determination of the Bifuractaion diagram is challenging and not always feasible. By means of the principle of continuation, the diagram can be established nevertheless [98]. In brief, a predefined bifurcation parameter is varied whereby the respective stability is determined for each parameter. Thereby, the required steady-states, Jacobian matrices, eigenvalues, and amplitudes of the limit cycles are numerically calculated. In the present work, built-in MATLAB functions were used for this purpose. For the determination of stability maps, as, for instance, Figures 3.9 and 3.16, the presented bifurcation analysis can be extended to account for a set of bifurcation parameters.

C
Controller verification

Before the designed control concept can be applied at the real plant, the controller (4.18) has to be validated. For that purpose, a series of simulations with the related non-linear process model was carried out. The corresponding simulation scenarios and results are presented in Table C.1 and Figure C.1.

Starting with a log-normal size distributed particle population,

$$q\left(t=0, L\right) = \frac{1}{(\sigma_{\text{init}} L \sqrt{2\pi})} \, \exp\left(-\frac{\ln\left(L - L_{\text{Init}}\right)}{2\sigma_{\text{init}}^2}\right)$$

with $L_{\text{init}} = 0.8275$ mm and $\sigma_{\text{init}} = 0.3625$ mm, the simulation corresponding to default parameter set $\Pi_{\text{exp},0}$ proves that the controller drives the FBLG into a stable steady-state. In the subsequent simulations, the initial profile of the size distribution is shifted by setting $L_{\text{init}} = 0.70$ mm ($\Pi_{\text{exp,init}}^-$) and $L_{\text{init}} = 0.95$ mm ($\Pi_{\text{exp,init}}^+$). In both cases, the controller is capable of stabilizing the process. Afterward, by setting $d_{32,\text{ref}} = 0.75$ mm ($\Pi_{\text{exp},d_{32}}^-$) and $d_{32,\text{ref}} = 1.05$ mm ($\Pi_{\text{exp},d_{32}}^+$), it is investigated how a change of the reference value influences the granulation process. A decrease of $d_{32,\text{ref}}$ leads, as expected, to an intensification of the particle milling represented by an increase of the consumed mill power p_{mill}. Referring to the actual $d_{32,\text{bed}}$, stationary accuracy, $d_{32,\text{ref}} - d_{32,\text{bed}} = 0$,

Table C.1.: Operating parameters and simulation scenarios related to the controller verification. The remaining parameters comply with the default parameter set presented in Table 4.1.

Parameter set $\Pi_{\text{exp},0}$			Simulation scenarios	
L_{init}	0.8275	mm	$\Pi_{\text{exp,init}}^-$	$L_{\text{init}} = 0.70$ mm
σ_{init}	0.3625	mm	$\Pi_{\text{exp,init}}^+$	$L_{\text{init}} = 0.95$ mm
$d_{32,\text{ref}}$	0.90	mm	$\Pi_{\text{exp},d_{32}}^-$	$d_{32,\text{ref}} = 0.75$ mm
L_{cs}	0.375	mm	$\Pi_{\text{exp},d_{32}}^+$	$d_{32,\text{ref}} = 1.05$ mm
			$\Pi_{\text{exp},L_{\text{cs}}}^-$	$L_{\text{cs}} = 0.325$ mm
			$\Pi_{\text{exp},L_{\text{cs}}}^+$	$L_{\text{cs}} = 0.400$ mm
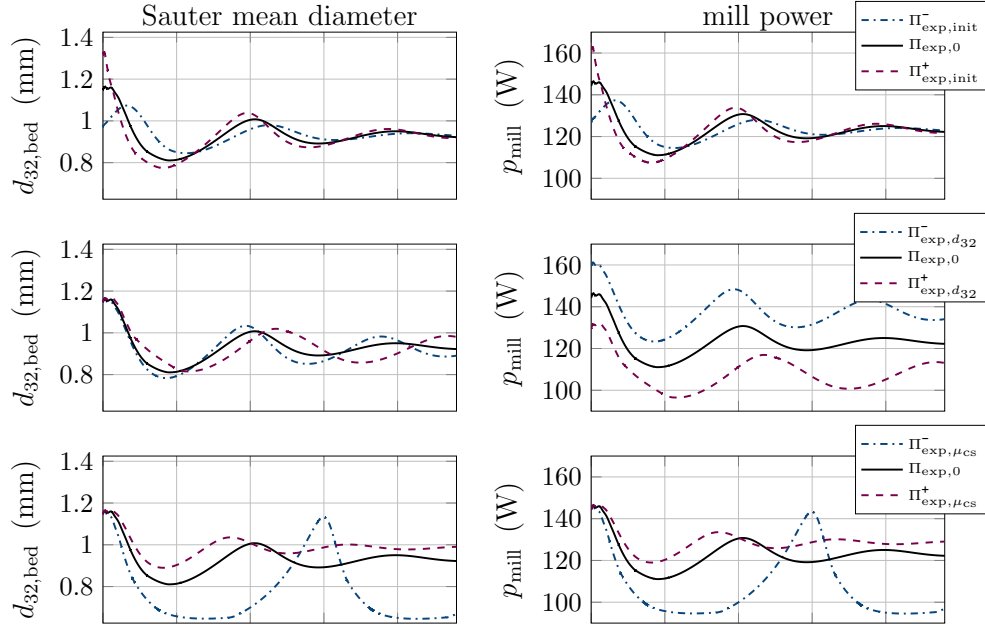
Figure C.1.: Verification of the designed control strategy by simulations: Influence of initial particle size distribution $q_0\,(t=0,L)$ (**upper row**), reference value $d_{32,\mathrm{ref}}$ (**center row**), and cut-size μ_{cs} (**lower row**) on process stability.

is not achieved. This observation is not remarkable as the tested controller does not include integral action. However, the controller dampens the induced oscillations nevertheless such that the process settles a steady-state.

Summarizing the simulation results presented so far, the application of the designed controller at the real plant is promising to enhance process dynamics and suppress the occurrence of self-sustained oscillations. Then again, one has to be aware that variations of the process configuration may lead to a failure of the control strategy. For instance, a change of the fluidization conditions, here represented by a change of the cut-size L_{cs} in scenarios $\Pi^{-}_{\mathrm{exp},L_{\mathrm{cs}}}$ and $\Pi^{+}_{\mathrm{exp},L_{\mathrm{cs}}}$, may result in the occurrence of self-sustained oscillations.

D

System matrices of H$_\infty$ controllers

The H$_\infty$ controllers $K_{\infty,\mathrm{I}}$ and $K_{\infty,\mathrm{II}}$ were determined with the Robust Control Toolbox of Matlab 2018b (The MathWorks, Natick, USA). The utilized function `mixsyn` solves the established optimization problem and returns the calculated sub-optimal γ and the corresponding controller in state-space representation:

$$s\mathbf{X}_K(s) = A_K\mathbf{X}_K + B_K\mathbf{U}_K$$
$$\mathbf{Y}_K(s) = C_K\mathbf{X}_K + D_K\mathbf{U}_K \ .$$

The input vector consists of the control errors

$$\mathbf{U}_K(s) = \begin{bmatrix} d_{32,\mathrm{ref}} - d_{32,\mathrm{bed}} & \eta_{\mathrm{ref}} - \eta \end{bmatrix}^t \ ;$$

the output vector returns the actuating values

$$\mathbf{Y}(s) = \begin{bmatrix} \Delta L_{\mathrm{mill,0}} & \Delta\theta_{\mathrm{f,in}} \end{bmatrix}^t \ .$$

For the sake of clarity, the state-space models of order N were converted to a system of transfer functions:

$$K_{\infty,k}(s) = \begin{bmatrix} \dfrac{\sum_{i=1}^{N} a_{k,(1,1),i}s^i}{\sum_{i=1}^{N} b_{k,i}s^i} & \dfrac{\sum_{i=1}^{N} a_{k,(1,2),i}s^i}{\sum_{i=1}^{N} b_{k,i}s^i} \\ \dfrac{\sum_{i=1}^{N} a_{k,(2,1),i}s^i}{\sum_{i=1}^{N} b_{k,i}s^i} & \dfrac{\sum_{i=1}^{N} a_{k,(2,2),i}s^i}{\sum_{i=1}^{N} b_{k,i}s^i} \end{bmatrix} \ .$$

The related γ and parameters are presented in Table D.1.

Table D.1.: Parameters of the transfer functions of robust controllers.

controller $K_{\infty,\text{I}}$: $\gamma = 0.68$

i	$a_{\text{I},(1,1),i}$	$a_{\text{I},(1,2),i}$	$a_{\text{I},(2,1),i}$	$a_{\text{I},(2,2),i}$	$b_{\text{I},i}$
12	0.0	0.0	0.0	0.0	1.0
11	2.9×10^{-1}	1.0×10^{-2}	-2.6×10^{-4}	1.3×10^{-2}	5.9×10^{-1}
10	3.5×10^{-1}	1.1×10^{-2}	-3.8×10^{-4}	1.9×10^{-2}	1.6×10^{-1}
9	5.5×10^{-2}	8.6×10^{-4}	-1.5×10^{-4}	7.2×10^{-3}	1.8×10^{-2}
8	2.8×10^{-3}	1.4×10^{-6}	-2.8×10^{-5}	1.3×10^{-3}	7.8×10^{-4}
7	8.2×10^{-6}	3.7×10^{-7}	-1.4×10^{-6}	4.1×10^{-5}	2.6×10^{-6}
6	1.4×10^{-8}	-4.1×10^{-10}	-3.2×10^{-9}	1.4×10^{-7}	5.2×10^{-9}
5	1.5×10^{-11}	1.3×10^{-12}	-7.6×10^{-12}	2.9×10^{-10}	6.3×10^{-12}
4	1.1×10^{-14}	-1.3×10^{-15}	-7.1×10^{-15}	3.6×10^{-13}	5.3×10^{-15}
3	5.6×10^{-18}	2.6×10^{-19}	-6.3×10^{-18}	3.0×10^{-16}	1.8×10^{-18}
2	1.4×10^{-21}	-1.1×10^{-21}	-1.9×10^{-21}	1.1×10^{-19}	1.7×10^{-23}
1	6.7×10^{-27}	-5.3×10^{-27}	-9.2×10^{-27}	5.6×10^{-25}	4.3×10^{-29}
0	3.9×10^{-38}	-3.0×10^{-38}	-5.3×10^{-38}	3.2×10^{-36}	2.5×10^{-40}

controller $K_{\infty,\text{II}}$: $\gamma = 0.95$

i	$a_{\text{II},(1,1),i}$	$a_{\text{II},(1,2),i}$	$a_{\text{II},(2,1),i}$	$a_{\text{II},(2,2),i}$	$b_{\text{II},i}$
17	0.0	0.0	0.0	0.0	1.0
16	2.0×10^{-1}	-8.3×10^{-6}	-8.2×10^{-5}	1.2×10^{-4}	2.7×10^{-1}
15	2.1×10^{-1}	-8.7×10^{-6}	-1.0×10^{-4}	1.5×10^{-4}	3.6×10^{-2}
14	1.1×10^{-2}	-4.0×10^{-7}	-2.2×10^{-5}	3.5×10^{-5}	1.9×10^{-3}
13	1.9×10^{-4}	-5.3×10^{-9}	-2.4×10^{-6}	4.0×10^{-6}	4.7×10^{-5}
12	8.1×10^{-7}	7.4×10^{-10}	-8.1×10^{-8}	1.7×10^{-7}	5.1×10^{-7}
11	1.9×10^{-9}	1.8×10^{-11}	-3.2×10^{-10}	2.6×10^{-9}	1.9×10^{-9}
10	2.9×10^{-12}	6.0×10^{-15}	-8.3×10^{-13}	1.1×10^{-11}	4.3×10^{-12}
9	3.2×10^{-15}	4.7×10^{-17}	-1.4×10^{-15}	2.7×10^{-14}	6.5×10^{-15}
8	2.7×10^{-18}	1.1×10^{-20}	-1.6×10^{-18}	4.3×10^{-17}	7.0×10^{-18}
7	1.7×10^{-21}	-4.3×10^{-23}	-1.4×10^{-21}	4.9×10^{-20}	5.0×10^{-21}
6	8.0×10^{-25}	-6.8×10^{-26}	-7.9×10^{-25}	3.8×10^{-23}	2.2×10^{-24}
5	2.5×10^{-28}	-7.1×10^{-29}	-2.9×10^{-28}	1.8×10^{-26}	5.3×10^{-28}
4	5.2×10^{-32}	-2.8×10^{-32}	-6.5×10^{-32}	4.6×10^{-30}	6.6×10^{-32}
3	6.1×10^{-36}	-4.8×10^{-36}	-8.1×10^{-36}	6.0×10^{-34}	3.4×10^{-36}
2	3.1×10^{-40}	-3.0×10^{-40}	-4.2×10^{-40}	3.2×10^{-38}	5.1×10^{-43}
1	2.3×10^{-47}	-2.3×10^{-47}	-3.2×10^{-47}	2.4×10^{-45}	1.9×10^{-50}
0	1.3×10^{-58}	-1.3×10^{-58}	-1.8×10^{-58}	1.4×10^{-56}	1.1×10^{-61}

E

Multi-stage FBLG

The multi-stage operation allows for combining different process steps in a single operation unit. By extending the introduced dynamic model accounting for single-stage FBLG (5.2) – (5.25), the influence of operating parameters and process configuration on product properties and process dynamics in multi-stage FBLG can be examined by theoretical analyses and simulation studies.

For illustration, two different process configurations of a four-stage FBLG are studied: in the first, suspension is injected on each stage; in the second, the third and fourth stages are used for drying of the particles. The used parameter sets $\Pi_{\mathrm{ms,1}}$ and $\Pi_{\mathrm{ms,2}}$ are presented in Table E.1. In the corresponding simulations, the associated results are presented in Figures E.1 – E.4, the nominal mean diameter of milled particles $L_{\mathrm{mill,0}}$ is reduced from 0.8 mm to 0.725 mm at $t_1 = 2$ h. Again, the initial states of the simulations are the steady-states related to the parameter set at $t = 0$ h.

Compared to $\Pi_{\mathrm{ms,1}}$, the configuration $\Pi_{\mathrm{ms,2}}$ leads to a reduction of the particle moisture content X_j and a raise of the temperature of the particles $\theta_{\mathrm{p},j}$ in the third and the fourth stage throughout the simulation. Meanwhile, the change of $L_{\mathrm{mill,0}}$ at $t_{\mathrm{s}} = 2$ h, leads to the occurrence of self-sustained oscillations of the particle size for $\Pi_{\mathrm{ms,1}}$ while the induced oscillation are decaying for $\Pi_{\mathrm{ms,2}}$.

Table E.1.: Simulation scenarios related to multi-stage FBLG. The remaining parameters correspond to default parameter set of single-stage operation $\Pi_{\mathrm{pro,0}}$ presented in Table 5.2.

	$\dot{m}_{\mathrm{inj,1}}$	$\dot{m}_{\mathrm{inj,2}}$	$\dot{m}_{\mathrm{inj,3}}$	$\dot{m}_{\mathrm{inj,4}}$		$L_{\mathrm{mill,0}}$	$t_1 = 2$ h
$\Pi_{\mathrm{ms,1}}$	10.0	10.0	10.0	10.0	(kg/h)	0.8 (mm)	$L_{\mathrm{mill,0}} = 0.725$ (mm)
$\Pi_{\mathrm{ms,2}}$	10.0	10.0	0.0	0.0	(kg/h)	0.8 (mm)	$L_{\mathrm{mill,0}} = 0.725$ (mm)

Figure E.1.: Simulation results related to scenario $\Pi_{\mathrm{ms},1}$: temperatures and moisture content of particles and fluidization medium on 1$^{\mathrm{st}}$ stage (——), 2$^{\mathrm{nd}}$ stage (——), 3$^{\mathrm{rd}}$ stage (——), and 4$^{\mathrm{th}}$ stage (——).

Figure E.2.: Simulation results related to scenario $\Pi_{\mathrm{ms},1}$: Normalized particle size distributions $q_{0,j}$ on stage j.
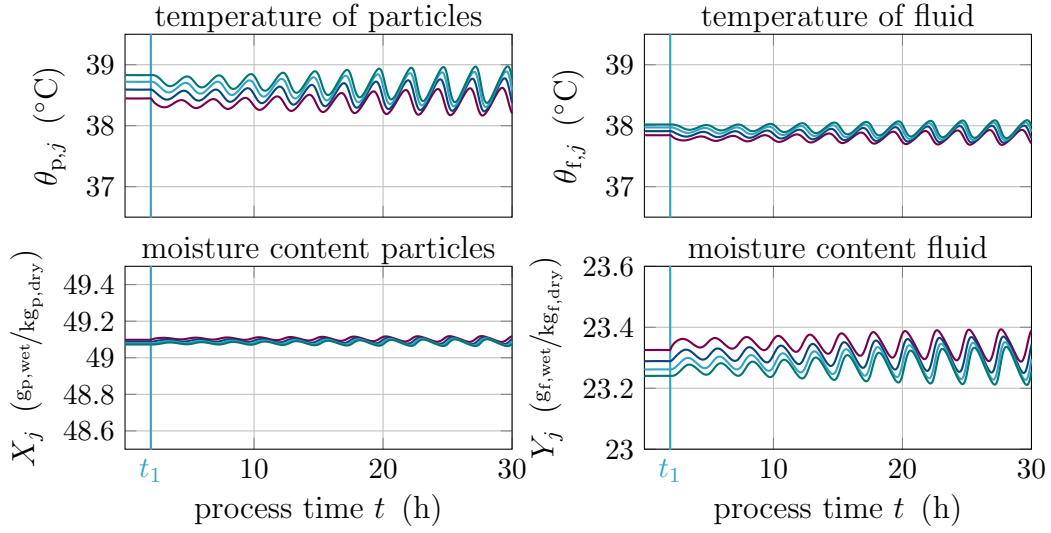
Figure E.3.: Simulation results related to scenario $\Pi_{ms,2}$: temperatures and moisture content of particles and fluidization medium on 1st stage (——), 2nd stage (- - -), 3rd stage (——), and 4th stage (——).
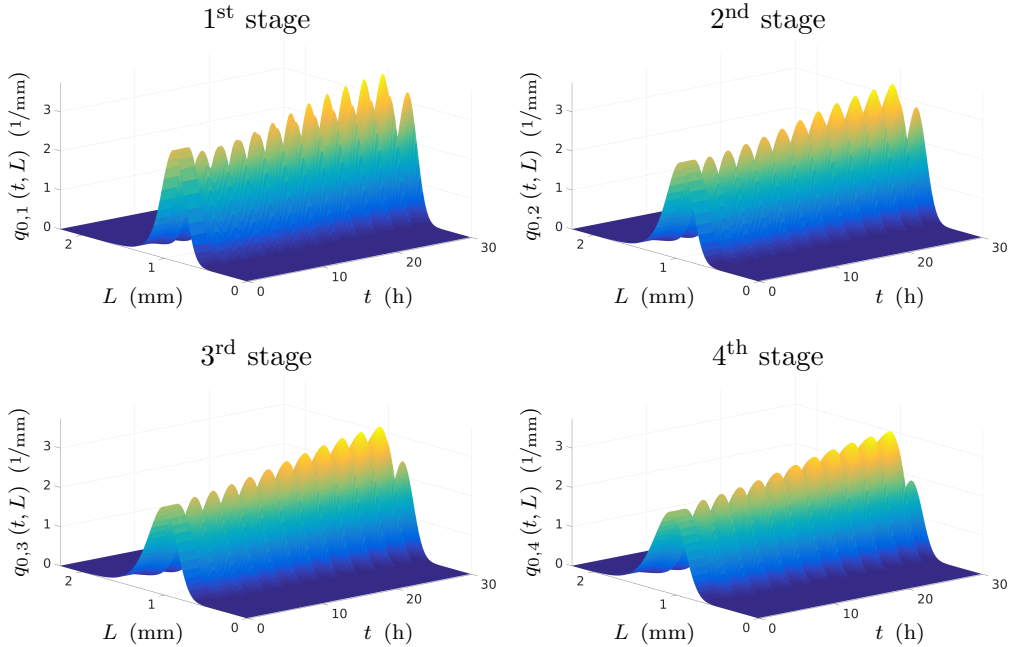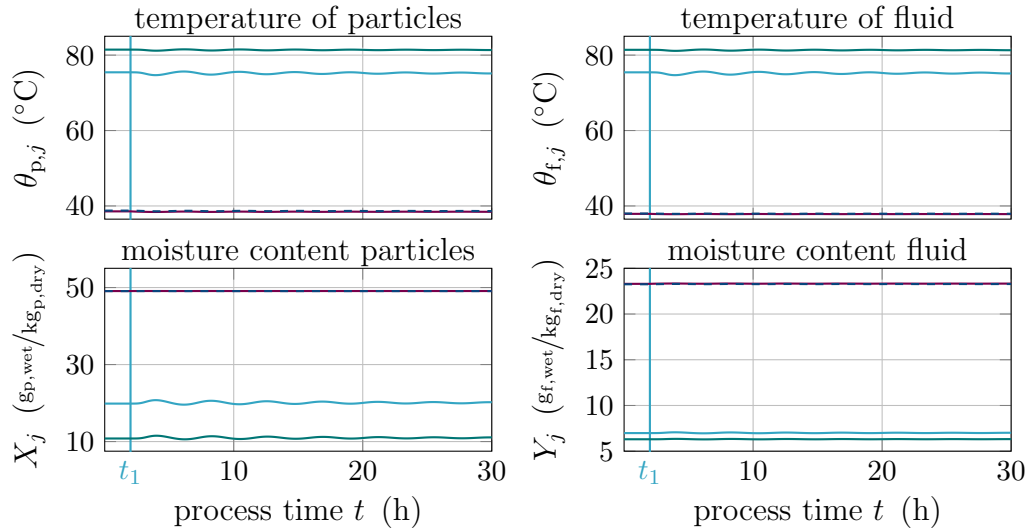

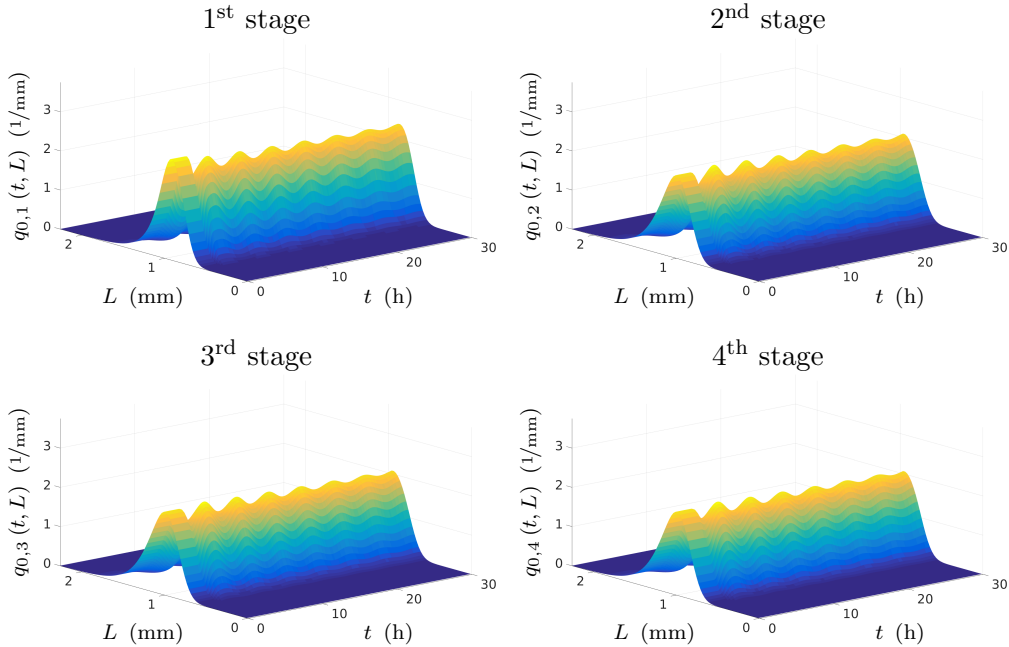Figure E.4.: Simulation results related to scenario $\Pi_{ms,2}$: Normalized particle size distributions $q_{0,j}$ on stage j.

R   Bibliography

[1] ANTONYUK, S., KHANAL, M., TOMAS, J., HEINRICH, S., AND MÖRL, L. Impact breakage of spherical granules: Experimental study and dem simulation. *Chemical Engineering and Processing: Process Intensification 45*, 10 (2006), 838 – 856. Particulate Processes A Special Issue of Chemical Engineering and Processing.

[2] ANTONYUK, S., TOMAS, J., HEINRICH, S., AND MÖRL, L. Breakage behaviour of spherical granulates by compression. *Chemical Engineering Science 60*, 14 (2005), 4031 – 4044. Granulation across the length scales - 2nd International Workshop on Granulation.

[3] BACHMANN, P., BÜCK, A., AND TSOTSAS, E. Investigation of the residence time behavior of particulate products and correlation for the bodenstein number in horizontal fluidized beds. *Powder Technology 301* (2016), 1067 – 1076.

[4] BACHMANN, P., BÜCK, A., AND TSOTSAS, E. Experimental investigation and correlation of the bodenstein number in horizontal fluidized beds with internal baffles. *Powder Technology 308* (2017), 378 – 387.

[5] BERTIN, D. E., COTABARREN, I., PINA, J., AND BUCALÁ, V. Granule size distribution for a multi-chamber fluidized-bed melt granulator: Modeling and validation using process measurement data. *Chemical Engineering Science 104* (2013), 319 – 329.

[6] BERTIN, D. E., COTABARREN, I. M., BUCALÁ, V., AND PINA, J. Analysis of the product granulometry, temperature and mass flow of an industrial multichamber fluidized bed urea granulator. *Powder Technology 206*, 1–2 (2011), 122 – 131. 9th International Symposium on Agglomeration and 4th International Granulation Workshop, 2009.

[7] BOEREFIJN, R., DONTULA, P.-R., AND KOHLUS, R. Chapter 14 detergent granulation. In *Granulation*, A. Salman, M. Hounslow, and J. Seville, Eds., vol. 11 of *Handbook of Powder Technology*. Elsevier Science B.V., 2007, pp. 673 – 703.

[8] Börner, M., Bück, A., and Tsotsas, E. DEM-CFD investigation of particle residence time distribution in top-spray fluidised bed granulation. *Chemical Engineering Science 161* (2017), 187 – 197.

[9] Börner, M., Hagemeier, T., Ganzer, G., Peglow, M., and Tsotsas, E. Experimental spray zone characterization in top-spray fluidized bed granulation. *Chemical Engineering Science 116*, 0 (2014), 317 – 330.

[10] Börner, M., Peglow, M., and Tsotsas, E. Particle residence times in fluidized bed granulation equipments. *Chemical Engineering & Technology 34*, 7 (May 2011), 1116–1122.

[11] Börner, M., Peglow, M., and Tsotsas, E. Derivation of parameters for a two compartment population balance model of wurster fluidised bed granulation. *Powder Technology 238*, 0 (2013), 122 – 131. Special Issue: 5th International Granulation Workshop Granulation across the length scale 2011.

[12] Brenan, K. E., Campbell, S. L., and Petzold, L. R. *Numerical Solution of Initial Value Problems in Differential-Algebraic Equations.* North Holland & Elsevier Science Publishing Company, 1989.

[13] Bück, A. *Model-based measurement and control of fluidised bed spray granulation processes.* PhD thesis, Otto-von-Guericke-Universität, November 2012.

[14] Bück, A., Dürr, R., Schmidt, M., and Tsotsas, E. Model predictive control of continuous layering granulation in fluidised beds with internal product classification. *Journal of Process Control 45* (2016), 65 – 75.

[15] Bück, A., Neugebauer, C., Meyer, K., Palis, S., Diez, E., Kienle, A., Heinrich, S., and Tsotsas, E. Influence of operation parameters on process stability in continuous fluidised bed layering with external product classification. *Powder Technology 300* (2016), 37 – 45.

[16] Bück, A., Palis, S., and Tsotsas, E. Model-based control of particle properties in fluidised bed spray granulation. *Powder Technology 270, Part B* (2015), 575 – 583. 6th International Workshop on Granulation: Granulation across the length scales.

[17] Bück, A., Peglow, M., Tsotsas, E., Mangold, M., and Kienle, A. Model-based measurement of particle size distributions in layering granulation processes. *AIChE Journal 57*, 4 (2011), 929–941.

[18] Bück, A., Seidel, C., Dürr, R., and Neugebauer, C. Robust feedback control of convective drying of particulate solids. *Journal of Process Control 69* (2018), 86 – 96.

[19] Cotabarren, I., Schulz, P. G., Bucalá, V., and Pina, J. Modeling of an industrial double-roll crusher of a urea granulation circuit. *Powder Technology 183*, 2 (2008), 224 – 230.

[20] Cotabarren, I. M., Bertín, D. E., Bucalá, V., and Pina, J. Feedback control strategies for a continuous industrial fluidized-bed granulation process. *Powder Technology 283* (2015), 415 – 432.

[21] Dernedde, M., Peglow, M., and Tsotsas, E. Stochastic modeling of fluidized bed granulation: Influence of droplet pre-drying. *Chemical Engineering & Technology 34*, 7 (July 2011), 1177–1184.

[22] Diez, E., Kieckhefen, P., Meyer, K., Bück, A., Tsotsas, E., and Heinrich, S. Particle dynamics in a multi-staged fluidized bed: Particle transport behavior on micro-scale by discrete particle modelling. *Advanced Powder Technology* (2019).

[23] Diez, E., Meyer, K., Bück, A., Tsotsas, E., and Heinrich, S. Influence of process conditions on the product properties in a continuous fluidized bed spray granulation process. *Chemical Engineering Research and Design 139* (2018), 104 – 115.

[24] Dorf, R. C., and Bishop, R. H. *Modern Control Systems*, 13th edition ed. Pearson, 2017.

[25] Dosta, M., Heinrich, S., and Werther, J. Fluidized bed spray granulation: Analysis of the system behaviour by means of dynamic flowsheet simulation. *Powder Technology 204*, 1 (2010), 71 – 82.

[26] Doyle, J., and Stein, G. Multivariable feedback design: Concepts for a classical/modern synthesis. *IEEE Transactions on Automatic Control 26*, 1 (February 1981), 4–16.

[27] Doyle, J. C., Glover, K., Khargonekar, P. P., and Francis, B. A. State-space solutions to standard h/sub 2/ and h/sub infinity / control problems. *IEEE Transactions on Automatic Control 34*, 8 (Aug 1989), 831–847.

[28] Drechsler, J., Peglow, M., Heinrich, S., Ihlow, M., and Mörl, L. Investigating the dynamic behaviour of fluidized bed spray granulation processes applying numerical simulation tools. *Chemical Engineering Science 60*, 14 (2005), 3817 – 3833. Granulation across the length scales - 2nd International Workshop on Granulation.

[29] Dreyschultze, C., Neugebauer, C., Palis, S., Bück, A., Tsotsas, E., Heinrich, S., and Kienle, A. Influence of zone formation on stability of continuous fluidized bed layering granulation with external product classification. *Particuology 23* (2015), 1–7.

[30] Dürr, R., Neugebauer, C., Palis, S., Bück, A., and Kienle, A. Inferential control of product properties for fluidized bed spray granulation layering. *IFAC-PapersOnLine* (2020). submitted for presentation at 21th IFAC World Congress, Berlin.

[31] ENNIS, B. J., TARDOS, G., AND PFEFFER, R. A microlevel-based characterization of granulation phenomena. *Powder Technology 65*, 1 (1991), 257 – 272. A Special Volume Devoted to the Second Symposium on Advances in Particulate Technology.

[32] ERBIL, H. Y. Evaporation of pure liquid sessile and spherical suspended drops: A review. *Advances in Colloid and Interface Science 170*, 1 (2012), 67 – 86.

[33] EVANS, W. R. Control system synthesis by root locus method. *Transactions of the American Institute of Electrical Engineers 69*, 1 (Jan 1950), 66–69.

[34] FISCHER, C., PEGLOW, M., AND TSOTSAS, E. Restoration of particle size distributions from fiber-optical in-line measurements in fluidized bed processes. *Chemical Engineering Science 66*, 12 (2011), 2842 – 2852.

[35] FRANK, U., WAWRA, S. E., PFLUG, L., AND PEUKERT, W. Multidimensional particle size distributions and their application to nonspherical particle systems in two dimensions. *Particle & Particle Systems Characterization 36*, 7 (2019), 1800554.

[36] FRIES, L., ANTONYUK, S., HEINRICH, S., DOPFER, D., AND PALZER, S. Collision dynamics in fluidised bed granulators: A dem-cfd study. *Chemical Engineering Science 86* (2013), 108 – 123. 5th International Granulation Workshop.

[37] FRIES, L., ANTONYUK, S., HEINRICH, S., AND PALZER, S. Dem–cfd modeling of a fluidized bed spray granulator. *Chemical Engineering Science 66*, 11 (2011), 2340 – 2355.

[38] GELDART, D. Types of gas fluidization. *Powder Technology 7*, 5 (1973), 285 – 292.

[39] GLOVER, K., AND DOYLE, J. C. State-space formulae for all stabilizing controllers that satisfy an H_∞-norm bound and relations to relations to risk sensitivity. *Systems & Control Letters 11*, 3 (1988), 167 – 172.

[40] GLÜCK, B. *Zustands- und Stoffwerte*, 2 ed. Verlag für Bauwesen GmbH Berlin, 1991.

[41] GNIELINSKI, V. G9 - Wärmeübertragung Partikel - Fluid in durchströmten Haufwerken. In *VDI Wärmeatlas*. VDI Verlag, 2013.

[42] GRÜNEWALD, G., WESTHOFF, B., AND KIND, M. Fluidized bed spray granulation: Nucleation studies with steady-state experiments. *Drying Technology 28*, 3 (2010), 349–360.

[43] GU, D.-W., PETKOV, P. H., AND KONSTANTINOV, M. M. *Robust Control Design with MATLAB*. Springer London, 2013.

[44] GUIGON, P., SIMON, O., SALEH, K., BINDHUMADHAVAN, G., ADAMS, M. J., AND SEVILLE, J. P. Chapter 5 roll pressing. In *Granulation*, A. Salman, M. Hounslow, and J. Seville, Eds., vol. 11 of *Handbook of Powder Technology*. Elsevier Science B.V., 2007, pp. 255 – 288.

[45] HAMPEL, N., BÜCK, A., PEGLOW, M., AND TSOTSAS, E. Continuous pellet coating in a wurster fluidized bed process. *Chemical Engineering Science 86*, 0 (2013), 87 – 98. 5th International Granulation Workshop.

[46] HAMPEL, N. A. *Diskontinuierliches und kontinuierliches Pelletcoating im Wurster-Wirbelschichtprozess.* PhD thesis, Otto-von-Guericke-Universität, May 2015.

[47] HEINRICH, S., PEGLOW, M., IHLOW, M., HENNEBERG, M., AND MÖRL, L. Analysis of the start-up process in continuous fluidized bed spray granulation by population balance modelling. *Chemical Engineering Science 57*, 20 (2002), 4369 – 4390. Particulate Processes.

[48] HOFFMANN, T. *Experimentelle Untersuchung des Einflusses von verschiedenen Prozessparametern auf das Partikel bei der Wirbelschicht-Sprühgranulation.* PhD thesis, Otto-von-Guericke-Universität, Januar 2017.

[49] HOFFMANN, T., PEGLOW, M., AND TSOTSAS, E. Prozessdynamik der Wirbelschichtgranulierung. *Chemie Ingenieur Technik 83* (2011), 658–664. Fachausschuss Agglomerations- und Schüttguttechnik, 22. Februar 2010, Fulda.

[50] HOFFMANN, T., RIECK, C., SCHMIDT, M., BÜCK, A., PEGLOW, M., AND TSOTSAS, E. Prediction of shell porosities in continuous fluidized bed spray layering. *Drying Technology 33*, 13 (2015), 1662–1670.

[51] HOUNSLOW, M. J., RYALL, R. L., AND MARSHALL, V. R. A discretized population balance for nucleation, growth, and aggregation. *AIChE Journal 34*, 11 (1988), 1821–1832.

[52] HULBURT, H., AND KATZ, S. Some problems in particle technology: A statistical mechanical formulation. *Chemical Engineering Science 19*, 8 (1964), 555 – 574.

[53] KONG, Y.-X., DI, Y.-Y., QI, Y.-D., YANG, W.-W., AND TAN, Z.-C. Low temperature heat capacities and standard molar enthalpy of formation of sodium benzoate C_6H_5COONa (s). *Thermochimica Acta 488*, 1 (2009), 27 – 32.

[54] KWAKERNAAK, H. Robustness optimization of linear feedback systems. In *The 22nd IEEE Conference on Decision and Control* (Dec 1983), pp. 618–624.

[55] LEVEQUE, R. J. *Finite Volume Methods.* Cambridge Texts in Applied Mathematics. Cambridge University Press, 2002, pp. 64 – 86.

[56] LITSTER, J., AND ENNIS, B. *The Science and Engineering of Granulation Processes*, vol. 15 of *Particle Technology Series.* Springer Netherlands, 2004.

[57] MARCHISIO, D. L., AND FOX, R. O. *Computational models for polydisperse particulate and multiphase systems.* Cambridge University Press, 2013.

[58] MARONGA, S., AND WNUKOWSKI, P. Modelling of the three-domain fluidized-bed particulate coating process. *Chemical Engineering Science 52*, 17 (1997), 2915 – 2925.

[59] McFarlane, D., and Glover, K. A loop-shaping design procedure using H$_\infty$ synthesis. *IEEE Transactions on Automatic Control 37*, 6 (June 1992), 759–769.

[60] Merkus, H. G., and Meesters, G. M. *Particulate Products - Tailoring Properties for Optimal Performance*, vol. 19 of *Particle Technology Series*. Springer International Publishing, 2014.

[61] Meyer, K., Bück, A., and Tsotsas, E. Dynamic multi-zone population balance model of particle formulation in fluidized beds. *Procedia Engineering 102* (2015), 1456 – 1465. New Paradigm of Particle Science and Technology Proceedings of The 7th World Congress on Particle Technology.

[62] Meyer, K., Bück, A., and Tsotsas, E. Determination of particle exchange rates at over-flow weirs in horizontal fluidised beds by particle tracking velocimetry. *Particuology 32* (2017), 1 – 9.

[63] Mielke, L., Hoffmann, T., Henneberg, M., Peglow, M., Bück, A., and Tsotsas, E. Reduction of energy consumption in batch fluidized bed layering granulation processes by temporal separation. *Chemical Engineering Research and Design 110*, Supplement C (2016), 2 – 11. 7th International Granulation Workshop, 2015.

[64] Molerus, O., and Hoffmann, H. Darstellung von Windsichtertrennkurven durch ein stochastisches Modell. *Chemie Ingenieur Technik 41* (1969), 792 – 796.

[65] Mörl, L., Heinrich, S., and Peglow, M. Chapter 2 fluidized bed spray granulation. In *Granulation*, M. H. A.D. Salman and J. Seville, Eds., vol. 11 of *Handbook of Powder Technology*. Elsevier Science B.V., 2007, pp. 21 – 188.

[66] Neugebauer, C., Bück, A., and Kienle, A. Control of particle size and porosity in continuous fluidized bed layering granulation processes with sieve mill cycle. *Chemical Engineering & Technology* – (2020). accepted for publication.

[67] Neugebauer, C., Bück, A., Palis, S., Mielke, L., Tsotsas, E., and Kienle, A. Influence of thermal conditions on particle properties in fluidized bed layering granulation. *Processes 6*, 12 (2018).

[68] Neugebauer, C., Diez, E., Bück, A., Palis, S., Heinrich, S., and Kienle, A. On the dynamics and control of continuous fluidized bed layering granulation with screen-mill-cycle. *Powder Technology 354* (2019), 765 – 778.

[69] Neugebauer, C., Palis, S., Bück, A., Diez, E., Heinrich, S., Tsotsas, E., and Kienle, A. Influence of mill characteristics on stability of continuous layering granulation with external product classification. In *26th European Symposium on Computer Aided Process Engineering*, Z. Kravanja and M. Bogataj, Eds., vol. 38 of *Computer Aided Chemical Engineering*. Elsevier, 2016, pp. 1275 – 1280.

[70] Neugebauer, C., Palis, S., Bück, A., Tsotsas, E., Heinrich, S., and Kienle, A. A dynamic two-zone model of continuous fluidized bed layering granulation with internal product classification. *Particuology 31* (2017), 8 – 14.

[71] NEUGEBAUER, C., SEIDEL, C., PALIS, S., AND KIENLE, A. Robust control of fluidized bed layering granulation. *IFAC-PapersOnLine* (2020). submitted for presentation at 21th IFAC World Congress, Berlin.

[72] OTTO, E., NEUGEBAUER, C., PALIS, S., AND KIENLE, A. Lyapunov-based online parameter estimation for continuous fluidized bed layering granulation. submitted for presentation at 21th IFAC World Congress, Berlin.

[73] PALIS, S. *Control of fluidized bed spray granulation processes.* PhD thesis, Otto-von-Guericke-Universität, September 2012.

[74] PALIS, S. Non-identifier-based adaptive control of continuous fluidized bed spray granulation. *Journal of Process Control 71* (2018), 46 – 51.

[75] PALIS, S., BÜCK, A., AND KIENLE, A. Entropy-based control of continuous fluidized bed spray granulation processes. *IFAC-PapersOnLine 48*, 13 (2015), 154 – 157. 5th IFAC Workshop on Lagrangian and Hamiltonian Methods for Nonlinear Control LHMNC 2015.

[76] PALIS, S., DREYSCHULTZE, C., AND KIENLE, A. A methodology for experimental determination of stability boundaries with application to fluidized bed spray granulation. In *24th European Symposium on Computer Aided Process Engineering*, P. S. V. Jiří Jaromír Klemeš and P. Y. Liew, Eds., vol. 33 of *Computer Aided Chemical Engineering.* Elsevier, 2014, pp. 625 – 630.

[77] PALIS, S., DREYSCHULTZE, C., NEUGEBAUER, C., AND KIENLE, A. Auto-tuning control systems for improved operation of continuous fluidized bed spray granulation processes with external product classification. *Procedia Engineering 102* (2015), 133 – 141.

[78] PALIS, S., AND KIENLE, A. Discrepancy based control of continuous fluidized bed spray granulation with internal product classification. *IFAC Proceedings Volumes 45*, 15 (2012), 756 – 761. 8th IFAC Symposium on Advanced Control of Chemical Processes.

[79] PALIS, S., AND KIENLE, A. Stabilization of continuous fluidized bed spray granulation with external product classification. *Chemical Engineering Science 70* (2012), 200 – 209. 4th International Conference on Population Balance Modeling.

[80] PALIS, S., AND KIENLE, A. H_∞ loop shaping control for continuous fluidized bed spray granulation with internal product classification. *Industrial & Engineering Chemistry Research 52*, 1 (2013), 408–420.

[81] PALIS, S., AND KIENLE, A. Discrepancy based control of particulate processes. *Journal of Process Control 24*, 3 (2014), 33 – 46.

[82] PALIS, S., AND KIENLE, A. Online parameter identification for continuous fluidized bed spray granulation with external sieve-mill cycle. *2017 22nd International Conference on Methods and Models in Automation and Robotics (MMAR)* (2017), 594–598.

[83] PALIS, S., NEUGEBAUER, C., BÜCK, A., HEINRICH, S., TSOTSAS, E., AND KIENLE, A. Control of multi-chamber continuous fluidized bed spray granulation. *Proceedings of PARTEC 2016* (2016), 1–4.

[84] PEGLOW, M., CUNÄUS, U., AND TSOTSAS, E. An analytical solution of population balance equations for continuous fluidized bed drying. *Chemical Engineering Science 66*, 9 (2011), 1916 – 1922.

[85] PETRAK, D. Simultaneous measurement of particle size and particle velocity by the spatial filtering technique. *Particle & Particle Systems Characterization 19*, 6 (2002), 391–400.

[86] PIETSCH, S., KIECKHEFEN, P., MÜLLER, M., SCHÖNHERR, M., JÄGER, F. K., AND HEINRICH, S. Novel production method of tracer particles for residence time measurements in gas-solid processes. *Powder Technology 338* (2018), 1 – 6.

[87] PITT, K., AND SINKA, C. Chapter 16 tabletting. In *Granulation*, A. Salman, M. Hounslow, and J. Seville, Eds., vol. 11 of *Handbook of Powder Technology*. Elsevier Science B.V., 2007, pp. 735 – 778.

[88] RADICHKOV, R., MÜLLER, T., KIENLE, A., HEINRICH, S., PEGLOW, M., AND MÖRL, L. A numerical bifurcation analysis of continuous fluidized bed spray granulation with external product classification. *Chemical Engineering and Processing: Process Intensification 45*, 10 (2006), 826 – 837.

[89] RANDOLPH, A. D. A population balance for countable entities. *The Canadian Journal of Chemical Engineering 42*, 6 (1964), 280–281.

[90] REYNOLDS, G. K., LE, P. K., AND NILPAWAR, A. M. Chapter 1 high shear granulation. In *Granulation*, A. Salman, M. Hounslow, and J. Seville, Eds., vol. 11 of *Handbook of Powder Technology*. Elsevier Science B.V., 2007, pp. 3 – 19.

[91] RIECK, C., HOFFMANN, T., BÜCK, A., PEGLOW, M., AND TSOTSAS, E. Influence of drying conditions on layer porosity in fluidized bed spray granulation. *Powder Technology 272* (2015), 120 – 131.

[92] SCHMIDT, M. *Process dynamics and structure formation in continuous spray fluidized bed processes.* PhD thesis, Otto-von-Guericke-Universität, October 2018.

[93] SCHMIDT, M., BÜCK, A., AND TSOTSAS, E. Experimental investigation of process stability of continuous spray fluidized bed layering with internal separation. *Chemical Engineering Science 126* (2015), 55 – 66.

[94] SCHMIDT, M., BÜCK, A., AND TSOTSAS, E. Experimental investigation of the influence of drying conditions on process stability of continuous spray fluidized bed layering granulation with external product separation. *Powder Technology 320*, Supplement C (2017), 474 – 482.

[95] SCHMIDT, M., RIECK, C., BÜCK, A., AND TSOTSAS, E. Experimental investigation of process stability of continuous spray fluidized bed layering with external product separation. *Chemical Engineering Science 137* (2015), 466 – 475.

[96] SCHULZ, T. Untersuchung der Sprühzone eines Granulationsprozesses in einer Wirbelschicht im Pilotmaßstab, 2016.

[97] SCHÜTTE, R., RUHS, A., PELGRIM, I., KLASEN, C.-J., AND KAISER, L. Fluidised bed spray granulation process producing two or more different size distributions, 1998.

[98] SEYDEL, R. *Practical Bifurcation and Stability Analysis.* No. 5 in Interdisciplinary Applied Mathematics. Springer, New York, NY, 2010.

[99] SHERONY, D. F. A model of surface renewal with application to fluid bed coating of particles. *Chemical Engineering Science 36*, 5 (1981), 845 – 848.

[100] SKOGESTAD, S., AND POSTLETHWAITE, I. *Multivariable Feedback Control: Analysis and Design*, second ed. John Wiley & Sons Ltd., 2007.

[101] SMITH, P., AND NIENOW, A. On atomising a liquid into a gas fluidised bed. *Chemical Engineering Science 37*, 6 (1982), 950 – 954.

[102] SONDEJ, F. *Morphologische Charakterisierung beschichteter Partikel und feststoffhaltiger Mikrotropfen.* PhD thesis, Otto-von-Guericke-Universität, August 2019.

[103] SONDEJ, F., BÜCK, A., KOSLOWSKY, K., BACHMANN, P., JACOB, M., AND TSOTSAS, E. Investigation of coating layer morphology by micro-computed x-ray tomography. *Powder Technology 273* (2015), 165 – 175.

[104] SONDEJ, F., PEGLOW, M., BÜCK, A., AND TSOTSAS, E. Experimental investigation of the morphology of salt deposits from drying sessile droplets by white-light interferometry. *AIChE Journal 64*, 6 (2018), 2002–2016.

[105] STIESS, M. *Mechanische Verfahrenstechnik - Partikeltechnologie 1.* Springer, 2009.

[106] STRENZKE, G., GOLOVIN, I., WEGNER, M., PALIS, S., BÜCK, A., KIENLE, A., AND TSOTSAS, E. Influence of drying conditions on process properties and parameter identification for continuous fluidized bed spray agglomeration. In *IDS 2018: 21st International Drying Symposium: proceedings* (Spain - València, September 2018), pp. 579 – 586.

[107] SU, Q., SCHIANO, S., WU, C.-Y., NAGY, Z. K., AND RIELLY, C. D. Dynamic impact milling model with a particle-scale breakage kernel. In *26th European Symposium on Computer Aided Process Engineering*, Z. Kravanja and M. Bogataj, Eds., vol. 38 of *Computer Aided Chemical Engineering*. Elsevier, 2016, pp. 475 – 480.

[108] TSOTSAS, E. Influence of drying kinetics on particle formation: A personal perspective. *Drying Technology 30*, 11-12 (2012), 1167–1175.

[109] TSUJI, Y., KAWAGUCHI, T., AND TANAKA, T. Discrete particle simulation of two-dimensional fluidized bed. *Powder Technology 77*, 1 (1993), 79 – 87.

[110] Turchiuli, C., Jimenèz, T., and Dumoulin, E. Identification of thermal zones and population balance modelling of fluidized bed spray granulation. *Powder Technology 208*, 2 (2011), 542 – 552. Special Issue: Papers presented to the Symposium STPMF 2009, Science and Technology of Powders and Sintered Materials.

[111] van Meel, D. Adiabatic convection batch drying with recirculation of air. *Chemical Engineering Science 9*, 1 (1958), 36 – 44.

[112] Verma, M., and Jonckheere, E. L^∞-compensation with mixed sensitivity as a broadband matching problem. *Systems & Control Letters 4*, 3 (1984), 125 – 129.

[113] Vogel, L., and Peukert, W. Breakage behaviour of different materials—construction of a mastercurve for the breakage probability. *Powder Technology 129*, 1 (2003), 101 – 110.

[114] Vogel, L., and Peukert, W. From single particle impact behaviour to modelling of impact mills. *Chemical Engineering Science 60*, 18 (2005), 5164 – 5176.

[115] Vollmari, K., Jasevičius, R., and Kruggel-Emden, H. Experimental and numerical study of fluidization and pressure drop of spherical and non-spherical particles in a model scale fluidized bed. *Powder Technology 291* (2016), 506 – 521.

[116] Vollmari, K., and Kruggel-Emden, H. Numerical and experimental analysis of particle residence times in a continuously operated dual-chamber fluidized bed. *Powder Technology 338* (2018), 625 – 637.

[117] Vreman, A., van Lare, C., and Hounslow, M. A basic population balance model for fluid bed spray granulation. *Chemical Engineering Science 64*, 21 (2009), 4389 – 4398.

[118] Vu, H. T., and Tsotsas, E. A framework and numerical solution of the drying process in porous media by using a continuous model. *International Journal of Chemical Engineering 2019* (2019), 9043670.

[119] Winkler, D. F. Verfahren zum Herstellen von Wassergas, 1922.

[120] Wnukowski, P., and Setterwall, F. The coating of particles in a fluidized bed (residence time distribution in a system of two coupled perfect mixers). *Chemical Engineering Science 44*, 3 (1989), 493 – 505.

[121] Wurster, D. E. Air-suspension technique of coating drug particles. a preliminary report. *Journal of the American Pharmaceutical Association 48*, 8 (1959), 451–454.

[122] Yates, J. G., and Lettieri, P. *Fluidized-Bed Reactors: Processes and Operating Conditions*, vol. 26 of *Particle Technology Series.* Springer International Publishing, 2016.

[123] ZAMES, G. On the input-output stability of time-varying nonlinear feedback systems part one: Conditions derived using concepts of loop gain, conicity, and positivity. *IEEE Transactions on Automatic Control 11*, 2 (April 1966), 228–238.

[124] ZAMES, G. Feedback and optimal sensitivity: Model reference transformations, multiplicative seminorms, and approximate inverses. *IEEE Transactions on Automatic Control 26*, 2 (April 1981), 301–320.

Declaration of honor

I hereby declare that I produced this thesis without prohibited external assistance and that none other than the listed references and tools have been used. I did not make use of any commercial consultant concerning graduation. A third party did not receive any nonmonetary perquisites neither directly nor indirectly for activities which are connected with the contents of the presented thesis. All sources of information are clearly marked, including my own publications. In particular I have not consciously:

- Fabricated data or rejected undesired results

- Misused statistical methods with the aim of drawing other conclusions than those warranted by the available data

- Plagiarized data or publications

- Presented the results of other researchers in a distorted way

I do know that violations of copyright may lead to injunction and damage claims of the author and also to prosecution by the law enforcement authorities. I hereby agree that the thesis may need to be reviewed with an electronic data processing for plagiarism. This work has not yet been submitted as a doctoral thesis in the same or a similar form in Germany or in any other country. It has not yet been published as a whole.

Magdeburg, February 17, 2020

Curriculum vitae

Due to the *General Data Protection Regulation* this part was removed from the thesis.

Scientific Contributions

Publications in peer-reviewed journals

- Dreyschultze, C., **Neugebauer, C.**, Palis, S., Bück, A., Tsotsas, E., Heinrich, S., Kienle, A., 2015. *Influence of zone formation on stability of continuous fluidized bed layering granulation with external product classification*, Particuology, 1 – 7.

- Bück, A., **Neugebauer, C.**, Meyer, K., Palis, S., Diez, E., Kienle, A., Heinrich, S., Tsotsas, E., 2016. *Influence of operation parameters on process stability in continuous fluidised bed layering with external product classification*, Powder Technology 300, 37 – 45.

- **Neugebauer, C.**, Palis, S., Bück, A., Tsotsas, E., Heinrich, S., Kienle, A., 2017. *A dynamic two-zone model of continuous fluidized bed layering granulation with internal product classification*, Particuology 31, 8 – 14.

- **Neugebauer, C.**, Bück, A., Palis, S., Mielke, L., Tsotsas, E., Kienle, A., 2018. *Influence of thermal conditions on particle properties in fluidized bed layering granulation*, Processes 6 (12), 235.

- Bück, A., Seidel, C., Dürr, R., **Neugebauer, C.**, 2018. *Robust feedback control of convective drying of particulate solids*, Journal of Process Control 69, 86 – 96.

- **Neugebauer, C.**, Diez, E., Bück, A., Palis, S., Heinrich, S., Kienle, A., 2019. *On the dynamics and control of continuous fluidized bed layering granulation with screen-mill-cycle*, Powder Technology 354, 765 – 778.

- Dürr, R., Seidel, C., **Neugebauer, C.**, Bück, A., 2019. *Self-tuning control of continuous fluidized bed drying of baker's yeast pellets*, Drying Technology, Article in press.

- **Neugebauer, C.**, Bück, A., Kienle, A., 2020. *Control of particle size and porosity in continuous fluidized bed layering granulation processes with sieve mill cycle*, accepted for publication in Chemical Engineering & Technology.

Conference proceedings

- Bück, A.[*], **Neugebauer, C.**, Meyer, K., Palis, S., Diez, E.; Kienle, A., Heinrich, S., Tsotsas, E., 2015. *Influence of operation parameters on process stability in continuous fluidised bed layering with external classification*[†], 7th International Granulation Workshop, Sheffield (UK).

- **Neugebauer, C.**[*], Palis, S., Bück, A., Diez, E., Heinrich, S., Tsotsas, E., Kienle, A., 2016. *Influence of mill characteristics on stability of continuous layering granulation with external product classification*[†], 26th European Symposium on Computer Aided Process Engineering, Portorož (Slovenia).

- Bück, A., Wegner, M., **Neugebauer, C.**[*], Palis, S., Tsotsas, E., 2016. *Bifurcation analysis of process stability of continuous fluidized bed agglomeration with external product classification*[†], 26th European Symposium on Computer Aided Process Engineering, Portorož (Slovenia).

- **Neugebauer, C.**[*], Bück, A., Palis, S., Mielke, L., Tsotsas, E., Kienle, A., 2018. *Influence of thermal conditions on particle properties in fluidized bed layering granulation*[‡], 6th International Conference on Population Balance Modelling: PBM 2018; Ghent (Belgium).

- Bück, A.[*], Schmidt, M., **Neugebauer, C.**, Palis, S., Kienle, A., Heinrich, S., Tsotsas, E., 2018. *Process dynamics of continuous fluidised bed layering granulation*[†], 8th International Granulation Workshop, Sheffield (UK).

- Bück, A.[*], **Neugebauer, C.**, Seidel, C., Dürr, R., Kienle, A., 2019. *Control of Shell and Particle Porosity in Fluidized Bed Layering Granulation*[†], The 12th European Congress of Chemical Engineering, Florence (Italy).

- Dürr, R.[*], Seidel, C., **Neugebauer, C.**, Bück, A., 2019. *Selftuning adaptive control for convective drying of particulate solids*[†], The 12th European Congress of Chemical Engineering, Florence (Italy).

- **Neugebauer, C.**, Seidel, C., Palis, S.[*], Kienle, A., 2020. *Robust Control of Fluidized Bed Layering Granulation*, submitted for presentation at 21th IFAC World Congress, Berlin (Germany).

- Dürr, R.[*], **Neugebauer, C.**, Palis, S., Bück, A., Kienle, A., 2020. *Inferential control of product properties for fluidized bed spray granulation layering*, submitted for presentation at 21th IFAC World Congress, Berlin (Germany).

- Otto, E.[*], **Neugebauer, C.**, Palis, S., Kienle, A., 2020. *Lyapunov-based online Parameter Estimation for Continuous Fluidized Bed Layering Granulation*, submitted for presentation at 21th IFAC World Congress, Berlin (Germany).

---

[*] *(designated)* presenter
[†] presented as poster
[‡] presented as conference talk

Further conference talks

- Bück, A., **Neugebauer, C.***, Wegner, M., Palis, S., Tsotsas, E., 2016. *Prozessdynamik der kontinuierlichen Agglomeration mit externer Klassierung*, Jahrestreffen der ProcessNet-Fachgruppen Agglomerations- und Schüttguttechnik, Mehrphasenströmungen und Computational Fluid Dynamics, Bingen (Germany).

- **Neugebauer, C.***, Diez, E., Bück, A., Palis, S., Heinrich, S., Kienle, A., 2019. *Dynamics & Control of Continuous Fluidized Bed Layering Granulation*, International Congress on Particle Technology (PARTEC), Nuremberg (Germany).

Further poster presentations on conferences

- **Neugebauer, C.**, Palis, S., Bück, A.*, Heinrich, S., Tsotsas, E., Kienle, A., 2016. *Nonlinear Dynamics of Continuous Fluidized Bed Layering Granulation with Internal Product Classification*, International Congress on Particle Technology (PARTEC), Nuremberg (Germany).

- Diez, E.*, Meyer, K., Bück, A., Tsotsas, E., **Neugebauer, C.,**, Palis, S., Kienle, A., Heinrich, S., 2017. *Spray granulation in a multi-staged continuous fluidized bed: Influencing the product properties and particle transport in a horizontal fluidized bed*, 10th World Congress of Chemical Engineering, Barcelona (Spain).

- Diez, E.*, **Neugebauer, C.**, Palis, S., Kienle, A., Mielke, L., Tsotsas, E., Bück, A., Heinrich, S., 2019. *Dynamic behavior of the spray granulation in continuously operated horizontal fluidized beds*, 9th International Granulation Workshop, Lausanne (Switzerland).

---

*presenter